博士論文

論文題目　Elucidation of Energy Conversion Mechanism for Electrons in Magnetic Reconnection with a Guide-Field

(ガイド磁場リコネクションにおける電子へのエネルギー変換機構の解明)

氏　　名　郭　学瀚

Abstract

Magnetic reconnection is a fundamental plasma process that is breaking and topological rearrangement of magnetic field lines in plasma during which the fast conversion from magnetic energy to particle energy occurs through acceleration and/or heating. In this dissertation, we examine how magnetic energy is converted into electron kinetic and thermal energy during magnetic reconnection with a guide-field using fully kinetic 2.5D particle-in-cell (PIC) simulations and laboratory experiments in UTST and MRX.

The 2D electron temperature profile obtained using Thomson scattering measurement system and triple Langmuir probes in UTST and MRX respectively shows that electrons are heated around the X-point. Measurements and analyses suggest that electrons are heated by anomalous resistivity, but the precise mechanisms that generate the anomalous resistivity remain unknown. The classical Ohmic dissipation based on the perpendicular Spitzer resistivity cannot explain the measured 2D temperature profile. The required heating power exceeds that of classical Ohmic dissipation by a factor due to the high electron temperature. To explain the high electron temperature, the Ohmic dissipation must be larger than the classical value, indicating the presence of anomalous resistivity. Magnetic and electrostatic fluctuations in the lower hybrid frequency range are observed near the X-point. These fluctuations may contribute to the observed non-classical electron heating, but additional measurements on the wave characteristics are required to draw definitive conclusions.

The 1D electron temperature profile with three different guide-field ratio in MRX suggests that the guide-field ratio plays a key role on the electron heating near the X-point. The parallel component of the magnetic energy dissipation is dominant in all three different guide-field ratio 1-3. Since this trend is also observed in 2D PASMO simulation qualitatively, the parallel acceleration is a strong candidate for the electron energization in the vicinity of the X-point.

The electron perpendicular heating mainly due to the breaking of magnetic moment conservation in the high density separatrix is observed in 2D PASMO simulation. The charge separation generates intense variation of electric field, which is sustained by the non-ideal effects within the several electron Larmor radii. Meanwhile, electron perpendicular acceleration takes place manly due to the polarization drift term as well as the curvature drift term of the magnetic energy dissipation in the downstream near the X-point. This energy conversion mechanism can explain the elongated profile of the high electron temperature measured in MRX.

Acknowledgments

There are many people I would like to acknowledge who made this thesis possible. First, thank you to my advisor, Prof. Yasushi Ono, I truly thank you for your incredible support on plasma physics, magnetic reconnection and how to be a scientist in general. I remember that you informed me a summer school and scientific meeting in Sweden and suggested me to attend it. It was a kind of turning point in my life to learn how important to communicate with people who are not familiar with your work. Furthermore, you gave me incredible opportunities for international conferences and collaboration research at NIFS and PPPL. I have the utmost respect for your insight and your ability to see the big picture not only for plasma physics but also s scientist. I deeply thank Prof. Michiaki Inomoto, thank you for your support and encouragement. You have given me good guidance whenever I was stuck on a problem. I admire your ability to command wide - ranging knowledge of plasma physics and electronics.

Second, l would also like to acknowledge: my collaborators at NIFS: Dr. Ritoku Horiuchi, Dr. Chio-Zong (Frank) Cheng and Prof. Shunsuke Usami. You taught me how to use the group's code and patiently had a long discussion with me, a little boy having no knowledge of numerical simulation, every time when I visit to NIFS. My collaborators at PPPL: Dr. Masaaki Yamada who made huge effort to make this collaboration research successful, Prof. Hantao Ji who always concerned about me even when he was so busy about FLARE project, Dr. Will Fox, who gave me experimental tips for the guide-field reconnection in MRX, Dr. Jongsoo Yoo, who dedicate so much hours for running the experiments with me in MRX and Dr. Jonathan Jara-Almonte, who gave me incisive comments on the experimental setup and results and all of the great scientists I got to work with at PPPL in Princeton.

Many thanks to the current and former UTST students and post-docs, who took time to help me grow and shaped my understanding: Dr. Tanabe, thank you for providing

the experiment results from MAST and congratulations on getting married, Dr. Kotaro Yamasaki, you taught me how to run the experiment in UTST to analyze the data, Dr. Yasuhiro Kaminou, we had a lot of conversation about the research and the other in the office, Takumichi Sugawara, I always thank you for helping me to set Thomson scattering measurement up, Kento Nishida, you have the qualities to be one of the best students and to all of the graduate students who built a welcoming community: Keita Matsuyama, Naoto Kawakami, Akinori Sato, Yusuke Fukai, Haruki Yamanaka, Ryo Tamura, Taishi Kaneda, Hironori Hatano, Yusuke Minami, Kyohei Kondo, Takumi Mihara, Yuki Inai and Yoshifumi Takahata. Of course, I can't forget my classmates, Tomohiko Ushiki, Ryoma Yanai and Hideya Koike. Tomohiko (I have never called you like this in 5 years), you are the one of the nicest people I have ever met. I am so impressed how much effort you put into the research and what you accomplished in your Ph.D. I wish you good luck at QST. Ryoma, it was such fun to climb the mountain with you. Hideya, I wish I could have spent more time with you.

Sincere thanks to Prof. Yuichi Takase and his students, who invited me to play tennis in the lunchtime everyday if weather allows. Because of that, I have to come to the campus in the morning everyday and was able to concentrate to the research after the lunch despite of the food-coma. It motivates me to come to the campus and do the research. I will never forget that we won the tennis tournament in Kashiwanoha campus with the members in 2015.

Shout out to all of my friends, colleagues and staffs in the University of Tokyo. You made my life in Kashiwanoha campus delightful and happy. To my dearest friends, thanks for Yuya Nakano and Tatsuhiko Kawamoto always helping me to remember the importance of community and love, you two really did very little to help with this dissertation, but you helped me be a better human.

Finally, I am grateful to my father, Xinyu Guo, who is my inspiration and am excellent role model, and my mother, Hongzhi Li, who has provided me cares and supports in every way he could. I also appreciate all the support from other members of my family.

Contents

List of Figures

Chapter 1

Introduction

1.1 Magnetic Reconnection

The concept of magnetic reconnection was first suggested as a mechanism for particle acceleration in solar flares [1]. Since then, magnetic reconnection has been recognized as one of the fundamental processes in magnetized plasmas, whether in the laboratory, the solar system, or distant objects in the universe. It is widely believed that reconnection plays a key role not only in dynamic phenomena in the solar system such as solar flares, coronal mass ejections and magnetospheric substorms [2; 3; 4]. It also observed as the self-organization process in fusion plasmas, typically disruptions of tokamak discharge [5; 6].

Fundamentally, magnetic reconnection is the breaking and topological rearrangement of magnetic field lines in plasma during which the fast conversion from magnetic energy to particle energy occurs through acceleration and/or heating. Figure 1.1 shows a schematic view of magnetic reconnection. When highly conductive plasmas carrying anti-parallel magnetic field lines are brought together, a sheet-like field discontinuity, which corresponds to singularities of the current density would be caused, called “current sheet”. In the framework of ideal magnetohydrodynamics (MHD), magnetic field lines are frozen-in to the plasma and remain intact. However, when a pair of field lines approach each other, non-ideal effects become locally important. Then, a dissipation of current sheet allows the plasma diffusion and magnetic reconnection to occur.

Magnetic reconnection involves both a global process and a local process at the same time. Therefore, the dynamics of reconnection depend on both the local plasma parameters and the global boundary conditions. This is the reason that significant work remains

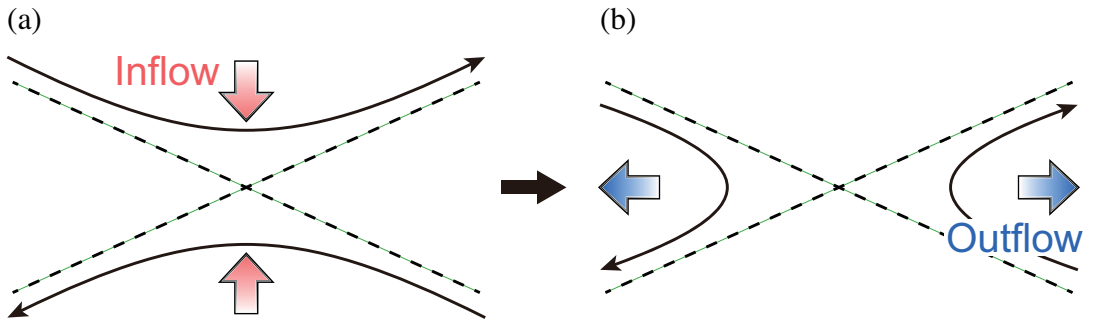

Figure 1.1: Schematic view of magnetic reconnection. (a) Before reconnection, two different field lines approach each other so that non-ideal MHD effects become important in the vicinity of the X-point. (b) After reconnection, newly reconnected field lines have high tension and therefore quickly pull away from the X-point.

in order to understand this intriguing phenomenon in spite of the progress made in the past few decades. The progress in understanding the physics of magnetic reconnection has been made from various sources: space and astrophysical observations, theory and numerical simulations, and laboratory experiments. Space and astrophysical observations have provided evidence that magnetic reconnection plays a key role in natural plasmas. Theory and numerical simulations provide breaking down the complex reconnection phenomena into a set of simpler processes and to gain improved physics understanding of each process. Laboratory experiments dedicated to the study of the fundamental reconnection physics measure the key plasma parameters at large number of points in the reconnection region.

1.1.1 Magnetic Induction and Frozen-in Fields

An important concept of magnetic reconnection is the motion of the magnetic field lines in the plasma. Now, we consider a non-ideal MHD plasma, then the generalized Ohm's law is described as:

$$\boldsymbol{E} + \boldsymbol{v} \times \boldsymbol{B} = \eta \boldsymbol{j}, \tag{1.1}$$

where η is a scalar plasma resistivity. The change of magnetic field is given by Faraday's law:

$$\frac{\partial \boldsymbol{B}}{\partial t} = -\nabla \times \boldsymbol{E}. \tag{1.2}$$

From Eq.(1.1) and Eq.(1.2), The change of magnetic field is described as:

$$\frac{\partial \boldsymbol{B}}{\partial t} = -(\nabla \times \eta \boldsymbol{j}) + \nabla \times (\boldsymbol{v} \times \boldsymbol{B}). \tag{1.3}$$

Inserting Ampère′s law, Eq.(1.3) becomes

$$\frac{\partial \boldsymbol{B}}{\partial t} = -\frac{\eta}{\mu_0}[\nabla \times (\nabla \times \boldsymbol{B})] + \nabla \times (\boldsymbol{v} \times \boldsymbol{B}) \tag{1.4}$$

$$= \nabla \times (\boldsymbol{v} \times \boldsymbol{B}) + \frac{\eta}{\mu_0}\nabla^2 \boldsymbol{B}. \tag{1.5}$$

This is known as the induction equation whose the first term on the right hand side represents the advection of field by the flow, and the second term represents a diffusion of the magnetic field due to the resistivity.

In most cases, the resistivity is very small. When we neglect the resistivity (assume $\eta \simeq 0$), Eq.(1.5) would be simplified to

$$\frac{\partial \boldsymbol{B}}{\partial t} = \nabla \times (\boldsymbol{v} \times \boldsymbol{B}), \tag{1.6}$$

which has the form of a continuity equation for the vector field $\boldsymbol{B}$.

If we now consider the magnetic flux through an arbitrary surface S bounded by a closed curve l, moving with the stream velocity $\boldsymbol{v}$, the magnetic flux Ψ is given by

$$\Psi = \int_S \boldsymbol{B} \cdot \mathrm{d}\boldsymbol{S}. \tag{1.7}$$

The convective derivative of magnetic flux Ψ is then described as:

$$\frac{\mathrm{d}\Psi}{\mathrm{d}t} = \int_S \frac{\partial \boldsymbol{B}}{\partial t} \cdot \mathrm{d}\boldsymbol{S} + \oint_l \boldsymbol{B} \cdot (\boldsymbol{v} \times \mathrm{d}\boldsymbol{l}), \tag{1.8}$$

and hence

$$\frac{\mathrm{d}\Psi}{\mathrm{d}t} = \int_S \left[\frac{\partial \boldsymbol{B}}{\partial t} - \nabla \times (\boldsymbol{v} \times \boldsymbol{B})\right] \cdot \mathrm{d}\boldsymbol{S}, \tag{1.9}$$

since

$$\oint_l \boldsymbol{B} \cdot (\boldsymbol{v} \times \mathrm{d}\boldsymbol{l}) = -\oint_l (\boldsymbol{v} \times \boldsymbol{B}) \cdot \mathrm{d}\boldsymbol{l} \tag{1.10}$$

$$= -\int_S \nabla \times (\boldsymbol{v} \times \boldsymbol{B})\, \mathrm{d}\boldsymbol{S}, \tag{1.11}$$

by Stoke's theorem. Sweeping the boundary curve l along the magnetic field lines defines a tube, called a magnetic flux tube. In the ideal MHD, the right hand side of Eq.(1.9)

is zero, called "frozen-in" condition. When this is valid then the magnetic field lines will move with the plasma as it moves. In Eq.(1.5), the magnetic field lines are not exactly tied to the plasma but can slip this distance. If this distance is small compared to the typical scale of the plasma then we can consider the magnetic field as frozen even if the resistivity is not exactly zero.

Therefore, the frozen-in law of ideal MHD states that magnetic field lines cannot be broken. However, if a finite resistivity exists, field lines can "slip" through a plasma by diffusion. This diffusion time scale $\tau_d = L^2\mu_0/\eta$ in a typical astrophysical plasma is too enormous to explain explosive phenomena such as solar flares. Here, L is a characteristic length scale of the system, μ_0 is the permeability of free space, and η is plasma resistivity. For a typical solar flare, τ_d is about 10^{14} s, while the observed duration of a solar flare is less than 10^3 s.

1.1.2 Resistive MHD Models

Sweet-Parker Model

The first model for magnetic reconnection was given independently by Sweet [7] and Parker [8], who approximated the phenomenon as a two-dimensional incompressible MHD phenomenon. Since the contributions of the two authors although independent were roughly equal in importance, their reconnection model has consistently been referred to as the Sweet-Parker model, which is based on resistive MHD and the Spitzer resistivity [9]. The Sweet-Parker model suggested that the growth of the current density during current sheet thinning saturates because finite resistivity leads to magnetic field diffusion, which balances the convective magnetic flux transport into the sheet. Therefore, the resistivity introduced magnetic reconnection; magnetic flux is transported into the sheet, reconnected and swept out of the sheet. Figure 1.2 shows the configuration of the Sweet-Parker model. Assuming incompressible motions, the stationary state is characterized by six values, three describing the dynamics.

1. the (poloidal) magnetic field B_0 immediately outside the current sheet, called the upstream field (the downstream field is negligible)
2. the upstream flow u_0 perpendicular to the field
3. the downstream flow v_0 along the field taken as the current sheet edge.

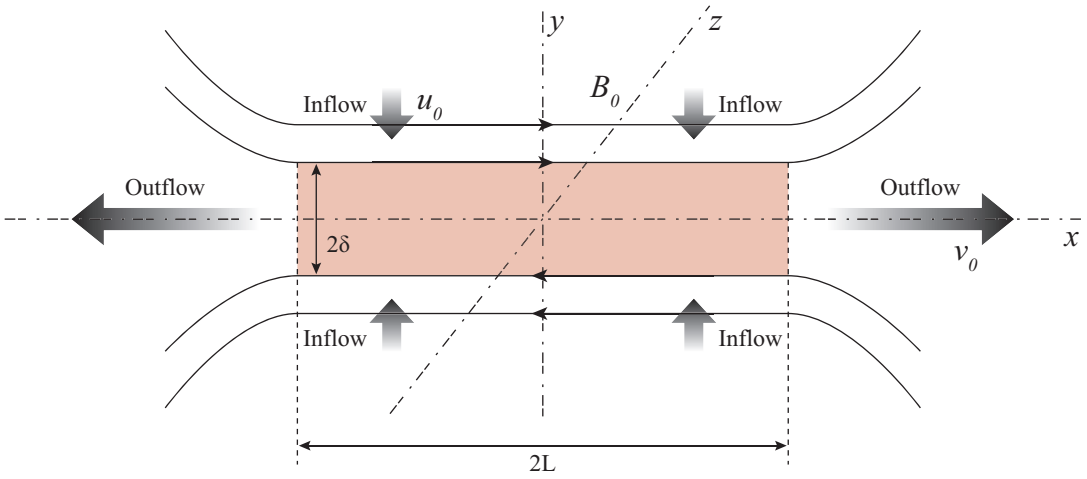

Figure 1.2: Schematic view of Sweet-Parker model. The current sheet which is red region is characterized by its thickness δ and width L.

4. the current sheet length L
5. the current sheet width δ
6. the plasma resistivity (diffusion coefficient) η

These six values are connected by three relations derived from the continuity equation, Ohm's law and the equation of motion, assuming stationary. First, integrating the continuity equation $\nabla \cdot \rho \boldsymbol{v} = 0$ over a quadrant of the current sheet and assuming constant density gives:

$$u_0 L = v_0 \delta, \tag{1.12}$$

where ρ is the mass density.

Next, we consider the generalized Ohm's law to describe the electric field:

$$\boldsymbol{E} = -(\boldsymbol{v} \times \boldsymbol{B}) + \eta \boldsymbol{j}. \tag{1.13}$$

Stationary requires E_y to be uniform in space. In the center of current sheet, the velocity vanished, as a result the resistive term dominates:

$$E_y = \eta j_y. \tag{1.14}$$

On the other hand, in the upstream region outside the current sheet, where the current density is small (ideal MHD condition is assumed), the resistive term is negligible:

$$E_y = -u_0 B_0. \tag{1.15}$$

This equation shows that the inflow plasma velocity is given by the $\boldsymbol{E}\times\boldsymbol{B}$ drift. Therefore, a relation is obtained as:

$$u_0 B_0 = \eta j_y \simeq \frac{\eta B_0}{\mu_0 \delta}. \tag{1.16}$$

Next, consider the force balance across the current sheet (the inertia term is negligible). Hence

$$\frac{\partial}{\partial z}\left(p + \frac{B^2}{2\mu_0}\right) = 0, \tag{1.17}$$

which gives:

$$\frac{B_0^2}{2\mu_0} = p_{\max} - p_0, \tag{1.18}$$

where $p_{\max}$ is the maximum pressure in the sheet center, where the (poloidal) magnetic field vanishes and p_0 is the upstream fluid pressure. Now, we consider the force balance along the mid-plane of the current sheet ($z = 0$). Since B_z is negligible, only the pressure force accelerates the fluid along the sheet due to no magnetic force:

$$v_x \frac{\partial v_x}{\partial x} = -\frac{\partial p}{\partial x}. \tag{1.19}$$

By integrating between center and edge yields, then it is obtained as:

$$\frac{\rho}{2} v_0^2 = p_{\max} - p_0. \tag{1.20}$$

Here, the current sheet edge $x = L$ is defined by the vanishing of the pressure difference across the sheet. From Eq.(1.19) and Eq.(1.20), we find the important result:

$$v_0^2 = v_A^2 = \frac{B_0^2}{\mu_0 \rho}, \tag{1.21}$$

where v_A is the Alfvén speed. The downstream outflow velocity equals the upstream Alfvén speed. This result also can be obtained from the vorticity equation without considering the pressure, which in incompressible theory is only an auxiliary quantity.

Using these relations, we can express two of the remaining values in terms of the other three:

$$M = \frac{u_0}{v_0} = \frac{u_0}{v_A} = \frac{1}{\sqrt{S}}, \tag{1.22}$$

where S is the Lundquist number:

$$S = \frac{\mu_0 L v_A}{\eta}. \tag{1.23}$$

Here we have introduced the Mach number M, which has been often used as a dimensionless measure of reconnection rate. The Sweet-Parker model narrowed the huge gap between theory and observation. The field lines need to diffuse only over δ, so that the required diffusion time scale reduces significantly. The Sweet-Parker reconnection time τ_{SP} is given by the geometric mean of the diffusion time and the Alfvén time as

$$\tau_{SP} = \sqrt{\tau_d \tau_A} = \sqrt{S}\tau_A, \tag{1.24}$$

where $\tau_d = L^2\mu_0/\eta$ and $\tau_A = L/V_A$. However, it was quickly realized that the Sweet-Parker reconnection model is still not adequate for astrophysical phenomena since S is usually large for astrophysical plasmas. For example, S is on the order of 10^5 in a typical solar flare, which gives the Sweet-Parker time of about 10^7 s, which is still far too slow.

Petschek Model

When Petschek introduced a new reconnection model [10] that allows a much faster energy release, the discrepancy between the Sweet-Parker model and the reality was seemed to be solved. The Petschek model is the introduction of a shock mediating the upstream-downstream transition which would greatly speed up the downstream outflow and reducing the size of the diffusion region, as shown in Fig.1.3. The reconnection diffusion region becomes X-shaped rather than double Y-shaped as in the Sweet-Parker model. Since the flow is sub-Alfvénic, these shocks have the characteristic properties of slow mode, then called slow shock.

Petschek showed that all the MHD relations were satisfied independent of the choice for the diffusion region length L^*, so it appears that L^* could be arbitrarily small. Petschek

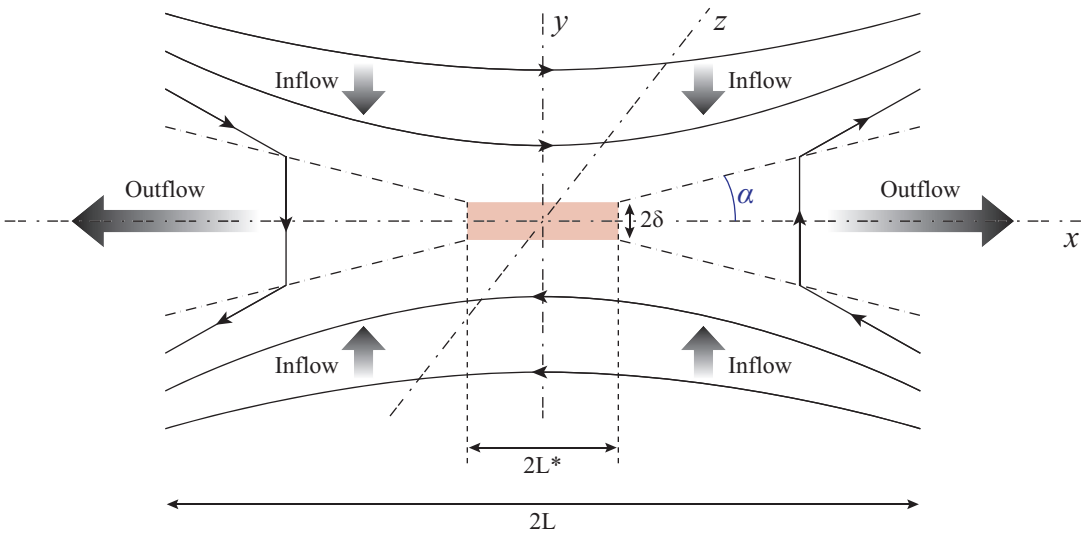

Figure 1.3: Schematic view of Petschek model. The reconnection rate is approximately three orders of magnitude faster than the Sweet-Parker model and the slow shocks provide energy conversion from magnetic energy to kinetic energy in Petschek model.

found that there is a limit on the shortness of this length:

$$L^* > L\frac{(\ln S)^2}{S}, \tag{1.25}$$

at which length the current in the shocks seriously perturbs the upstream flow. Also, Petschek derived an approximate analytical solution for the small shock angle $\alpha \ll 1$, and estimates the maximum achievable Mach number:

$$M = \frac{\pi}{8\ln S}, \tag{1.26}$$

which is approximately three orders of magnitude faster than the Sweet-Parker model. In this case, the maximum reconnection time scales as $(\ln S)\tau_A$, which can be a few percent of the Alfvén time, fast enough to account for astrophysical phenomena. The model was soon generally accepted and widely cited over the following two decades. In the 1980s, however, researchers started to realize that the Petschek model is not a self-consistent resistive MHD model. Numerical simulations with spatially uniform resistivity cannot reproduce Petschek's configuration [11]. It was also showed that the Petschek-type diffusion region can be maintained if anomalous resistivity is enforced locally at the diffusion region [12]. This means that Petschek model is just a possible resistive MHD configuration if there is an effective fast reconnection mechanism at the X-point.

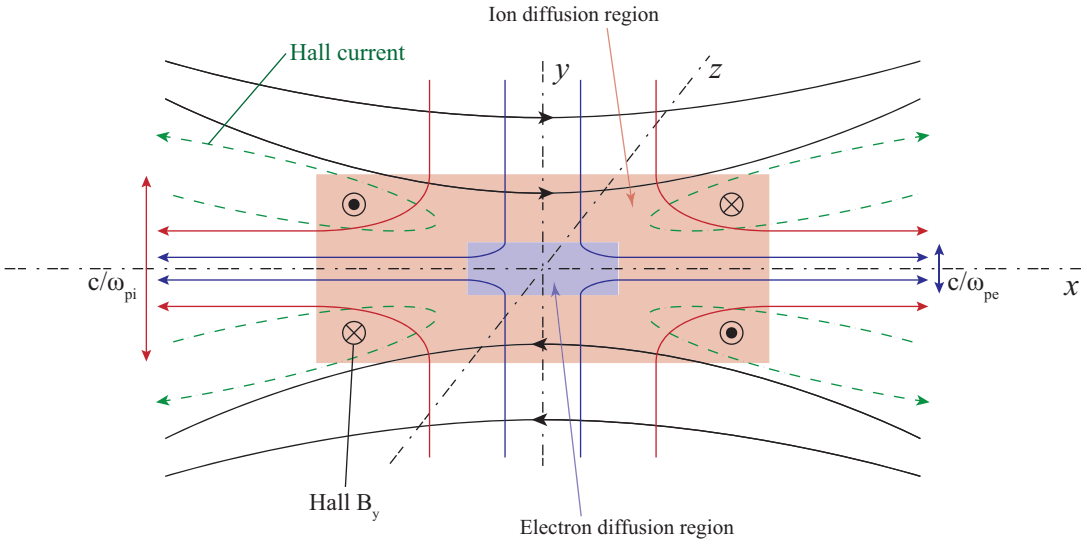

Figure 1.4: Schematic view of two-fluid dynamics in the reconnection layer. Ions decouple from electrons in the ion diffusion region whose width is on the order of the ion skin depth δ_i. Electrons are frozen in the magnetic lines until they reach to the electron diffusion region of the width on the order of the electron skin depth δ_e.

1.1.3 Two-Fluid Model

In addition to the fact that the Petschek model was not supported by MHD simulations, more observations in magnetospheric and hot fusion plasmas supported the assertion that the reconnection rate is still fast even in collision-less plasmas. These observations suggest that the physics of fast reconnection are something beyond resistive MHD.

The importance of two-fluid effects in the diffusion region was first recognized by Sonnerup [13]. Ions become unmagnetized first and form an ion diffusion region of the length scale on the ion skin depth $\delta_i \equiv c/\omega_{pi} = V_A/\omega_{ci}$ as shown in Fig.1.4. Here, ω_{pi} is the ion plasma oscillation frequency and ω_{ci} is the ion cyclotron frequency. On the other hand, electrons are tied to the magnetic field until they reach an electron diffusion region of the much smaller length scale on the electron skin depth $\delta_e \equiv c/\omega_{pe}$.

The mathematical difference between MHD and two-fluid theory appears in the different Ohm's laws. In the two-fluid regime, the MHD Ohm's law (Eq.(1.1)) can be rewritten as:

$$\boldsymbol{E} + \boldsymbol{v} \times \boldsymbol{B} - \frac{\boldsymbol{j} \times \boldsymbol{B}}{en} + \frac{1}{en} \nabla \cdot \boldsymbol{P}_e + \frac{m}{e} \frac{\mathrm{d}\boldsymbol{v}}{\mathrm{d}t} = \eta \boldsymbol{j}, \tag{1.27}$$

where $\boldsymbol{P}_e$ is the electron pressure tensor. This equation is correct even for MHD and is

reduced to the ordinary Ohm's law by setting $\boldsymbol{v}_e = \boldsymbol{v}_i = \boldsymbol{v}$ and neglecting the electron inertia and the pressure tensor terms. The generalized form of Ohm's law is identical to the equation of motion for electrons:

$$nm\frac{\mathrm{d}\boldsymbol{v}}{\mathrm{d}t} = -\nabla\cdot\boldsymbol{P}_e - en\left(\boldsymbol{E}+\boldsymbol{v}_e\times\boldsymbol{B}\right), \tag{1.28}$$

because $\boldsymbol{j} = en(\boldsymbol{v}_i - \boldsymbol{v}_e)$ and $\boldsymbol{v} = \boldsymbol{v}_i$.

Since electrons are still magnetized in the ion diffusion region, they flow in along the reconnecting field lines in the inflow region and out along the reconnected lines in the outflow regions. This difference in behavior between electrons and ions leads to a strong Hall effect from the $\boldsymbol{J}\times\boldsymbol{B}$ force inside the ion diffusion region.

The two-fluid effect is brought out by the example of a 2D reconnection problem in the x-y plane where the reconnection field is along the y direction. If the initial out-of-plane field B_z is zero (no guide field), there can be no B_z field in MHD theory because a symmetry requires the toroidal z component and the poloidal x and z components. In two-fluid theory, however, this symmetry is broken by the Hall term, which produce a quadruple out-of-plane magnetic field. It has been considered a signature of the Hall effect ever since. The existence of the Hall effect is supported by various space observations [14; 15; 16] and laboratory experiments [17; 18].

1.1.4 Kinetic Effects on Magnetic Reconnection

It is now widely accepted that two-fluid effects facilitate fast reconnection. The justification for using fluid models, however, is based on frequent collisions between particles. The fluid models cannot be used in relatively collision-less plasmas where fast reconnection is observed. There are important aspects of magnetic reconnection that cannot be properly described by fluid models.

To model the fully kinetic behavior of highly nonlinear phenomena such as magnetic reconnection, a full analytic theory becomes extremely difficult. The only practical method is based on numerical simulations using the particle-in-cell (PIC) technique. The detail of PIC technique is discussed in a following chapter. Due to the large-scale separations both in time and space, various approximations, such as the reduction of ratio between plasma frequency and electron cyclotron frequency ω_{pe}/ω_{ce} and mass ratio m_i/m_e, which are used in order for a simulation run to finish in a realistic time period even with modern

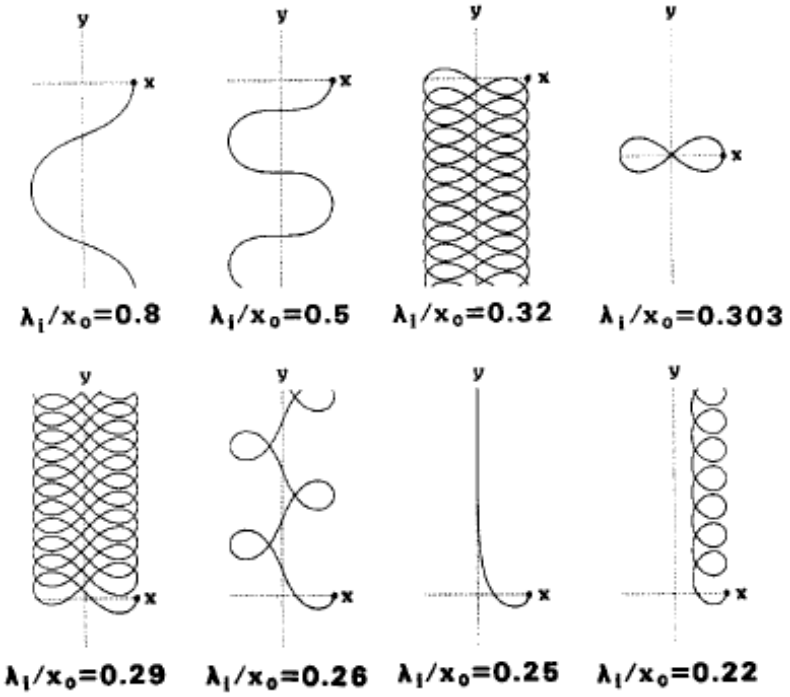

Figure 1.5: Eight types of ion meandering orbit in the one-dimensional neutral sheet model [19].

supercomputers.

In order to provide a convenient basis for theoretical analyses and numerical simulations of kinetic effects of magnetic reconnection, we should start a numerical simulation from a time-independent kinetic equilibrium solution with a neutral sheet confined between oppositely directed magnetic fields. Although it is very difficult to find an analytic solution for time-independent kinetic equilibrium due to the nonlinear Vlasov-Maxwell system, an elegant solution was found by using the constants of motion and shifted Maxwellian distribution functions [20]:

$$B_z = B_0 \tanh\left(\frac{x}{\delta}\right), \tag{1.29}$$

$$j_y = \frac{B_0}{\mu_0 \delta} \operatorname{sech}^2\left(\frac{x}{\delta}\right), \tag{1.30}$$

$$n = n_0 \operatorname{sech}^2\left(\frac{x}{\delta}\right), \tag{1.31}$$

where δ is the current sheet thickness given by

$$\delta = \left(\frac{c}{\omega_{pi}}\right) \frac{\sqrt{T/m_i}}{V}. \tag{1.32}$$

Here $V = V_i = -V_e$ is spatially constant drift velocity and $T = T_i = T_e$ is temperature.

In fully kinetic models where both ions and electrons are treated as particles, the force due to electron non-gyrotropic pressure in balancing reconnecting electric field has been reported to play an important role during magnetic reconnection. The importance of electron non-gyrotropic pressure was clearly shown in fully kinetic 2D simulations for both ions and electrons [21; 22]. It was found that the reconnection electric field is balanced by forces due to electron non-gyrotropic pressure, and electron inertial effects near the X-point. The non-gyrotropic pressure is closely related to particle meandering motion due to the finite Larmor radius effect near the center line [19; 23; 24]. When charged particles reach the neutral line, their gyroscopic motion reverses direction and they drift in the out-of-plane direction (see Fig.1.5). Fully kinetic simulations with large mass ratios have revealed that the off-diagonal ion pressure terms cancel the Hall effects outside of ion meandering orbit size, determining ion dissipation region [25].

1.1.5 Effects of the Guide-Field

The reconnecting magnetic field lines which reconnect are illustrated as opposite direction (anti-parallel) in Figs.1.1, 1.2, 1.3 and 1.4. In general, it does not need to be anti-parallel. In this case, reconnection can be thought of as occurring in the plane shown in Fig.1.4, but with a component of the magnetic field directed out of the plane (i.e., the z direction). This component of magnetic field, which is perpendicular to the reconnection plane, is called as guide-field. The dimensionless parameter can be installed for the discussion of the guide-field effects on the reconnection: the ratio of the out-of-plane component of the field to reconnecting component of the field in the inflow region, i.e., B_{guide}/B_{rec}. This guide-field ratio can play an important role in the dynamics of reconnection since the angular difference between the two field vectors on either side of the current sheet is referred to as the magnetic shear angle θ, which is related to the guide field by $B_{guide} = \tan((180 - \theta)/2)$. Even a small guide-field changes significantly dynamics of resonant electrons resulting in modification of the current sheet stability criteria [26; 27]. Particle dynamics changes from quasi-adiabatic to stochastic causing substantial asymmetry in the current structure and particle drifts [28].

To determine the dependence of the reconnection speed on merging angles of reconnecting lines, the magnitude of external guide field was varied in TS-3 and the MRX while the

reconnecting field was kept roughly constant [29; 30]. When the guide-field is zero, the reconnection speed is maximized and decreased substantially with increasing the guide-field. The guide-field distorts the quadrupole Hall magnetic field that is present in anti-parallel reconnection, resulting in an asymmetry of the Hall field across the reconnection exhaust in the particle simulations [31; 32] and the laboratory experiments [33; 34]. In general, the reconnection rates in guide-field reconnection are notably smaller than anti-parallel reconnection cases.

Since the electrons within the electron diffusion region are magnetized with the strong guide-field condition, the electron non-gyrotropic effects are expected to decrease. However, it has reported that the force terms associated with off-diagonal components of electron and ion pressure tensors due to non-gyrotropic motion of charged particles, becomes dominant at the reconnection point and sustain the reconnection electric field even when the guide-field is strong by the recent PIC simulation study [35; 36]. The large reconnection electric field along the magnetic field lines provides acceleration of electrons to super-thermal energy. This energetic electrons in the guide-field reconnection are observed in the solar flares [37; 38; 39], laboratory experiments [40; 41] and numerical simulations [42; 43; 44].

1.2 Reconnection in the Nature System

1.2.1 Solar Flares on the Sun

Solar flare is one of the most explosive phenomena among this dynamic solar activity. It is now widely believed that solar flare results from a rapid release of magnetic energy stored in the solar coronal magnetic field through magnetic reconnection. Magnetic reconnection is believed to occur slightly above the bright loop and to generate jets and energetic particles as shown Fig.1.6 [45; 46]. When the energetic particles move along the magnetic field and collide with the dense chromosphere plasma, they generate bursts of light such as hard X-rays (HXRs). Since the chromosphere plasma is heated by energy dissipation from energetic particles, it creates the SXR loop. This reconnection-based explanation of solar flares has been supported by observations of a typical soft X-ray cusp-like structure [47].

A number of satellites have been launched to study the behavior of solar flares: Yohkoh

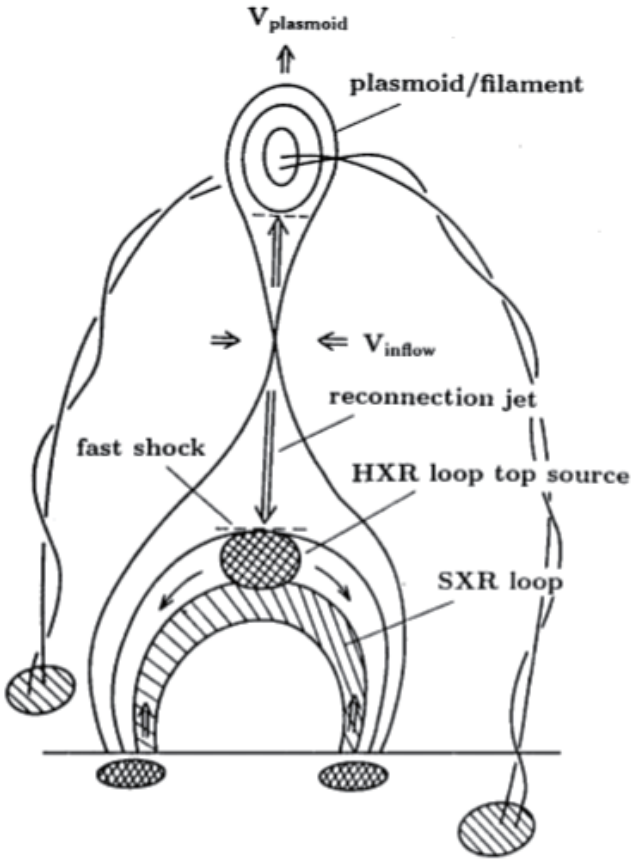

Figure 1.6: Plasmoid-induced-reconnection model, which shows magnetic reconnection site to be above the soft X-ray (SXR) loop [45].

(Sunbeam in Japanese), SOHO (Solar and Heliospheric Observatory), TRACE (Transition Region And Coronal Explorer), RHESSI (Ramaty High Energy Solar Spectroscopic Imager), Hinode (Sunrise in Japanese), and STEREO (Solar TErrestal RElations Observatory). In particular, Yohkoh, SOHO, TRACE and Hinode have shown the topological changes of solar flares as well as magnetic reconnection heating of corona plasmas in solar flares using 2D line-of-sight images [48]. Figure 1.7 shows observations of solar coronal loop-top flare measured by the Hinode satellite. The magnetic reconnection is considered to cause plasma heating and produce non-thermal particles in the solar flare. However, key questions on this explosive phenomenon remain unsolved and they will not be answered without improvements in the general understanding of magnetic reconnection.

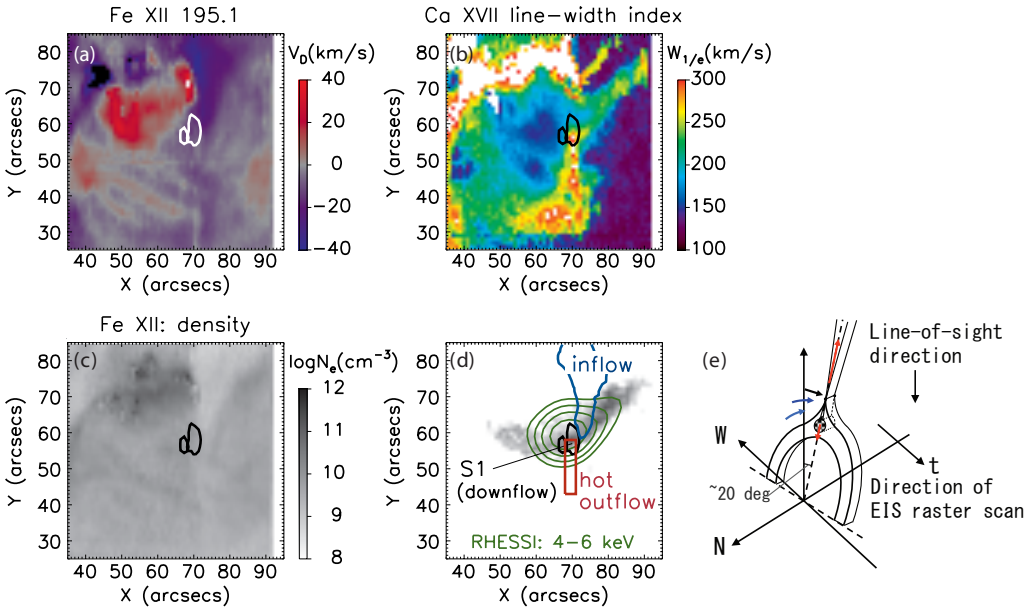

Figure 1.7: The Hinode satellite observation results of magnetic reconnection heating of corona plasmas in solar flares [48].

1.2.2 Geomagnetic Substorms in the Earth's Magnetosphere

Earth's magnetosphere is the region of influence of Earth's magnetic field. The interaction with the solar wind deforms the geomagnetic dipole field; it compresses the field lines of the day side (the magnetopause) and stretches the lines out to form a long tail (the magnetotail) on the night side as shown in Fig.1.8.

The magnetopause is one of the location of the first *in situ* space measurements of magnetic reconnection since it is accessible using satellite observations and has since repeatedly been an observational site for reconnection. One of the reason dayside reconnection is so important is because of its direct impact on Earth thought its role in space weather. Earth's magnetic field would largely protect Earth from the charged particles in space. However, reconnection changes the connectivity of magnetic fields and allows the transfer of material and energy from interplanetary space to the magnetosphere. This material could cause many problems such as power outages, satellite failure impacting GPS and cell phones. Therefore, the space weather forecast requires a thorough understanding of reconnection at the dayside magnetopause.

At the dayside magnetopause, the first direct and incontrovertible evidence of reconnec-

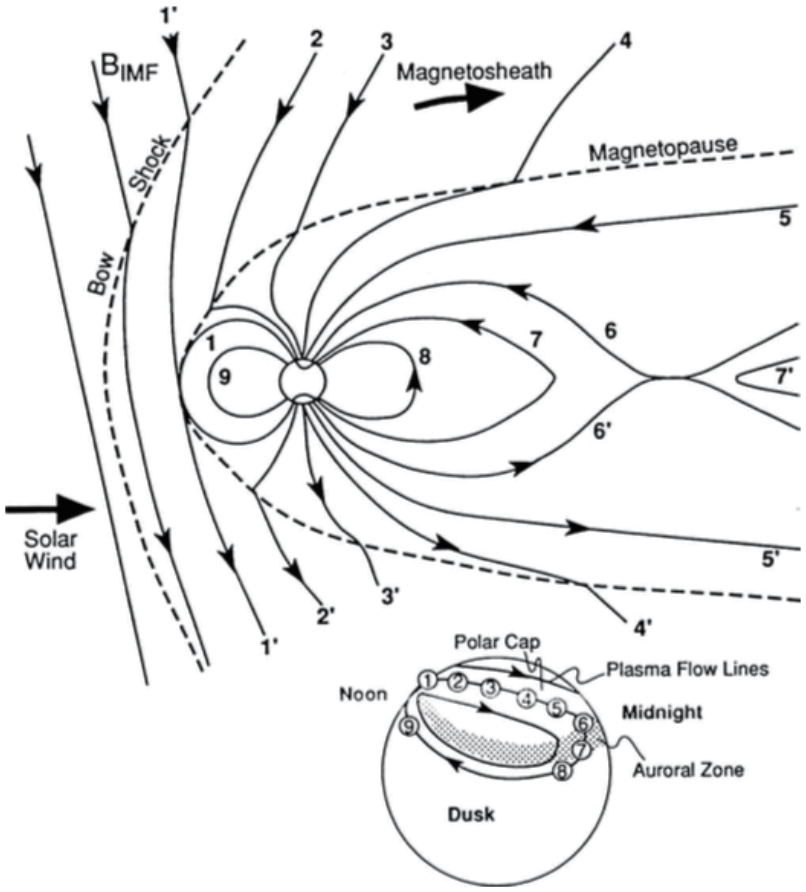

Figure 1.8: Schematics of magnetic reconnection and generated flow of plasmas in the magnetosphere [49].

tion was provided by Paschmann [50]. They observed high-speed flows associated with the reversal of the reconnecting magnetic field component, which was interpreted as the outflow resulting from reconnection. Many similar observations of plasma jets associated with magnetic reconnection have been reported [16; 51; 52; 53].

The magnetotail includes the plasma sheet, filled with the hot plasmas on the closed magnetic field lines with both their ends in the ionosphere, and tail lobes with empty open field lines, having one end in the Earth's polar cap ionosphere and another connected to interplanetary magnetic field. Evidence of magnetic reconnection has been also found in the magnetotail [15]. It is reported a rare encounter of an active diffusion region of collision-less magnetic reconnection. The X-line structure of reconnection extending more than 390 Earth radii has been observed in the magnetotail [54], which reveals that magnetotail reconnection is a large-scale process and can be in quasi-steady state. Fur-

thermore, it is argued by utilizing multiple satellites, that reconnection occurred before the associated geomagnetic substorm and thereby suggest that substorms are initiated by tail reconnection [55].

While the *in situ* measurement by using satellites has found a role of reconnection in the global dynamics, there is a lot of questions in the microphysics related to the electron diffusion region due to small number of encounters of the active diffusion region. In order to address this issue, a new NASA mission called the Magnetospheric Multi-scale (MMS) mission launched multiple satellites in 2014 to explore 3D structures of the diffusion region on scales down to the electron inertial length.

1.3 Dissertation Objectives

There is as of yet no consensus on how particles gain energy in the collision-less guide-field reconnection. To fill this gap, in this dissertation, energy conversion mechanisms for electrons during collision-less magnetic reconnection with a guide-field are discussed, based on measurements in the University of Tokyo Spherical Tokamak (UTST) and Magnetic Reconnection Experiment (MRX). Furthermore, the detail physics, which is difficult to address in the laboratory experiments due to the small scale of electron dynamics, is discussed based on 2D PIC simulation results by means of Plasma Simulation for Magnetic reconnection in an Open system (PASMO) code. The main objectives of this dissertation are:

1. To present where, when and how electrons are accelerated and heated during guide-field reconnection experiment and to assess the role of the guide-field on electron acceleration and heating.
2. To discuss possible mechanisms for observed electron heating in the vicinity of the X-point.
3. To discuss the difference of the electron dynamics between parallel and perpendicular to the magnetic field in the 2D particle simulation.

1.4 Outline of this Dissertation

This dissertation provides studies of energy conversion from magnetic energy to electron particle energy during collision-less magnetic reconnection in laboratory experiment (UTST and MRX) and numerical particle simulation (PASMO).

This dissertation is composed of six main chapters:

Chapter 1.

This chapter introduces the basic concept of magnetic reconnection and where we can find in the nature. Previous research on various energy conversion mechanisms is reviewed. Finally, the objectives and findings of this dissertation are summarized.

Chapter 2.

This chapter describes the experimental setup, the experimental regime and results of the University of Tokyo Spherical Tokamak (UTST). The details about magnetic diagnostics and Thomson scattering measurement for electron temperature and density are provided. It is shown that classical Ohmic dissipation based on the perpendicular Spitzer resistivity cannot explain the large electron heat flux along the magnetic field, which suggests the existence of an anomalous resistivity.

Chapter 3.

This chapter describes the setup and results of the Magnetic Reconnection Experiment (MRX) and the experimental regime for this study. The details about magnetic diagnostics, Langmuir probe for electron temperature and density and potential measurement are provided.

Chapter 4.

This chapter introduces the basic concept of the Particle-In-Cell (PIC) simulation and describes the setup of the 2D PASMO code for this study. The key schemes and dimensionless simulation parameters for the particle simulation are provided.

Chapter 5.

This chapter discusses the electron heating and acceleration mechanisms. It is shown that the parallel electric field and the in-plane electric field play a major role for the parallel and perpendicular component of the electron energy increment, respectively.

Chapter 6.

This chapter discusses the comparison between the laboratory experiments and the particle simulation, draws conclusions and presents ideas for future work.

Chapter 2

Laboratory Experiment in UTST

In this chapter, the University of Tokyo Spherical Tokamak (UTST) experimental apparatus and the operation of Double Null Merging (DNM) method are briefly described. Then, the diagnostics systems used for this dissertation are then discussed. Finally, the experimental results that we observed localized electron heating in high guide-field reconnection, are discussed.

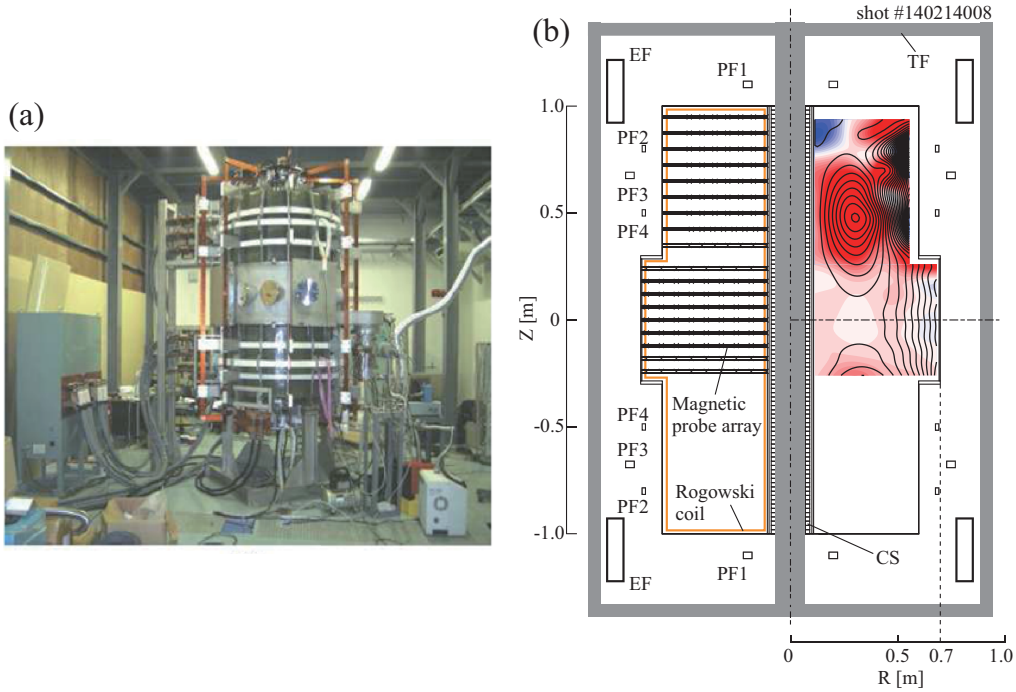

Figure 2.1: (a) The photograph of the UTST device, and (b) cross-sectional view of the UTST device are shown together with the magnetic probe array and plasma current Rogowski coil.

2.1 Overview of the University of Tokyo Spherical Tokamak (UTST)

The University of Tokyo Spherical Tokamak (UTST) [56] was constructed to show the feasibility of the DNM method for a high β ST startup [57]. The merging method has been used to increase magnetic flux of ST/CT plasmas without a CS coil in TS-3 [30], START [58], TS-4 [59] and MAST [60] devices and also to heat quickly ST plasmas in the TS-3 and UTST devices [61]. In the UTST device whose photograph is shown in Fig.2.1(a), all the coils are located outside the vacuum vessel, unlike TS-3, TS-4, MRX [62] and START/MAST devices (see Fig.2.1(b)). The DNM method is used for startup as well as a Neutral Beam Injection (NBI) heating would be used for an additional heating in UTST. The UTST device has a cylindrical vacuum vessel with $R = 0.6$ m (the maximum radius in the middle region is 0.7 m) and $Z = 2.0$ m. The upper and lower wall ($-1.0 \leq Z \leq -0.3, 0.3 \leq Z \leq 1.0$ m) is made of a thin stainless steel (SUS304 in the JIS standard) that is 1.5 mm thickness to allow the fast penetration of magnetic field into inside of the vacuum vessel. In order to sustain the mechanical strength, the thin conductive wall is covered with a 2 cm thickness of fiber-reinforced plastic (FRP) and supported by 16 conductive ribs.

2.2 Plasma Merging Operation

Figure 2.2 shows the current waveforms of the plasma current I_p, washer guns, poloidal field (PF), toroidal field (TF) and equilibrium field (EF) coils in a typical UTST shot. First, the (TF) coil and equilibrium field (EF) coils are discharged. Then, the combination of the toroidal and equilibrium field generates spiral magnetic field. After the poloidal flux generated by the EF coils penetrated the vacuum vessel, two washer guns located inside (one is in upper side and the other one is in bottom side) are discharged to perform the pre-ionization along with the spiral field. The voltage between the electrodes of the washer guns are 2.0 kV. As a result, two initial spherical torus (ST) plasmas are produced separately in both upper and lower regions of the UTST device by ramping down the currents of PF2 and PF4 coils. Meanwhile, the center solenoid (CS) coil is used to amplify the plasma currents of the initial ST plasmas to increase the upstream poloidal magnetic

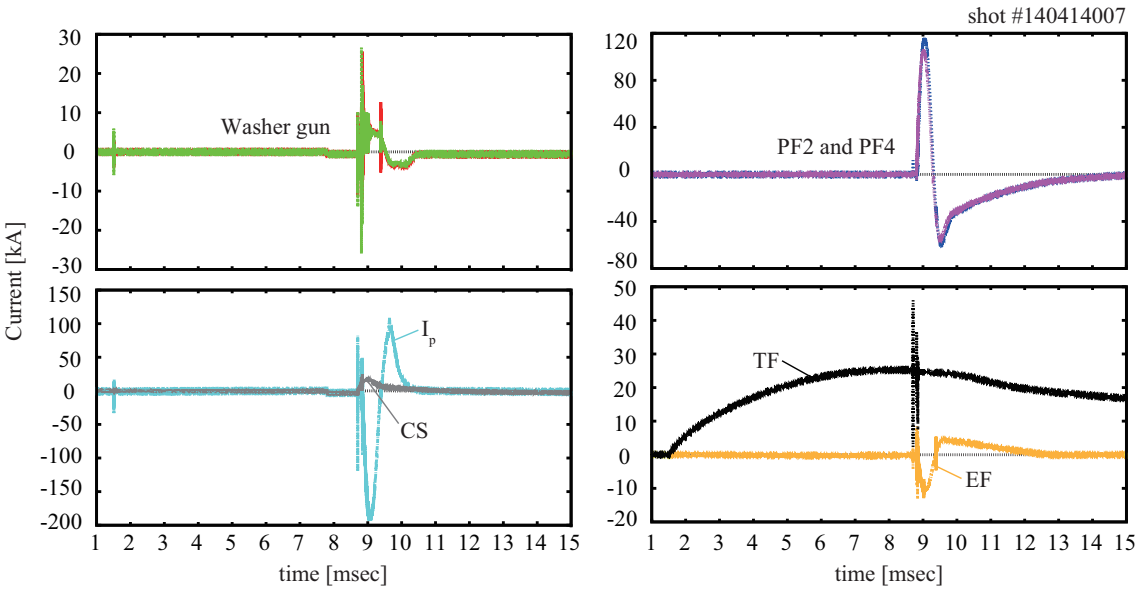

Figure 2.2: The time evolution of the current waveforms in a typical UTST shot. All plots show measured currents of the coils, washer guns and plasma during DNM startup in the UTST experiment.

field energy. The plasma current I_p measured by the internal Rogowski coil reached up 110 kA after plasma merging through magnetic reconnection, which continues for about 50 μs.

Figure 2.3 shows the time evolution of two-dimensional magnetic field structure measured by the magnetic probe array in the UTST merging experiment. The current waveforms of the washer gun, PF and CS coils and plasma current are shown in the top of Fig.2.3. And, the poloidal flux surfaces Ψ (line contour) and toroidal current density j_t (color contour) are shown in the bottom plot of Fig.2.3. The magnetic reconnection is observed during t = 750-810 μs, while we define $t = 0$ at the time of PF2 and PF4 coils discharges. The X-point structure was identified clearly around $R = 0.35$ m and $Z = 0$. The current sheet structure, which is indicated as blue region in he bottom plot of Fig.2.3, was observed by magnetic probe array during magnetic reconnection. The strength of reconnecting magnetic field (poloidal magnetic field in the upstream region) is typically 15 mT, as well as, the guide-field (toroidal magnetic field) at the X-point is typically 240 mT. Since the guide-field component is much higher than the reconnecting component, high guide-field magnetic reconnection takes place during the plasma merging period in the UTST device.

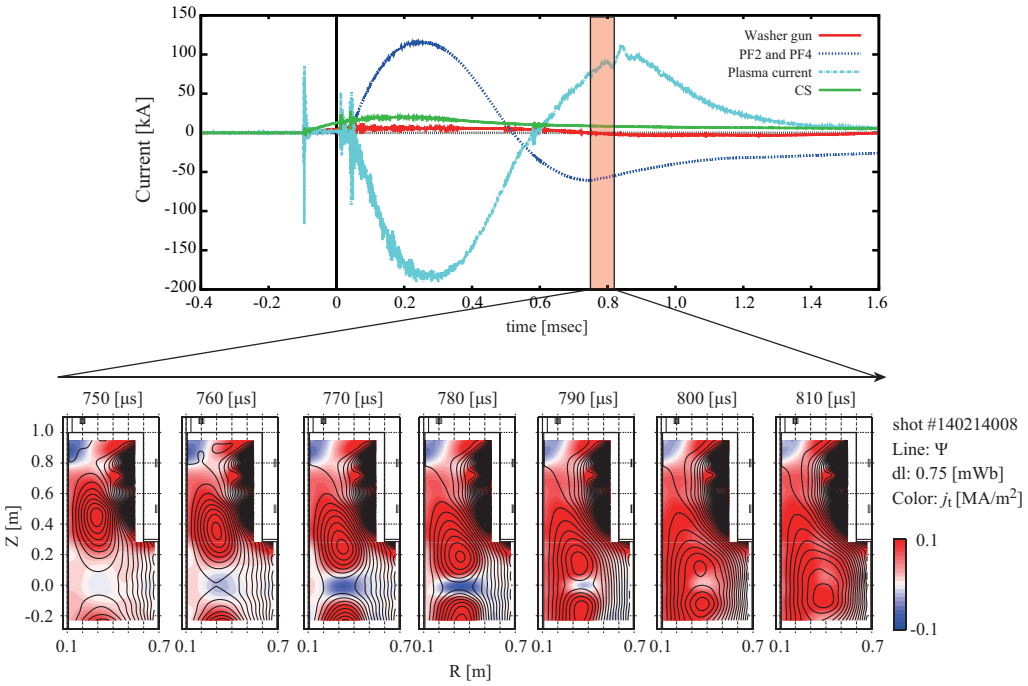

Figure 2.3: The top plot which is close-up plasma merging period shows the washer gun, coil, plasma currents. The bottom plot shows poloidal flux surfaces (lines) and toroidal current density (color) during magnetic reconnection in the UTST device. PF2 and PF4 coils are discharged at $t = 0$ ms.

2.3 Diagnostics

2.3.1 Magnetic Probe Array

In UTST, two-dimensional (R-Z plane) magnetic probe array, that is consist of multiple magnetic pickup coils is installed inside the vacuum vessel for magnetic reconnection study. The pickup coil has windings of 300 turns and whose outer and inner diameters are 5.0 mm and 3.5 mm, respectively. Since the signal output from pickup coil is proportional to $\mathrm{d}B/\mathrm{d}t$, we numerically integrated the signal to obtain the magnetic field:

$$B(t) = -\int_0^t \frac{V_{\mathrm{output}}(\tau)}{NS}\mathrm{d}\tau, \tag{2.1}$$

where NS is called as effective area of the coil: N is the number of turns and S is the area per turn of the coil.

The axial and toroidal magnetic fields (B_z and B_t) would be measured directly by using this measurement system. The locations of the magnetic probe arrays are illustrated in

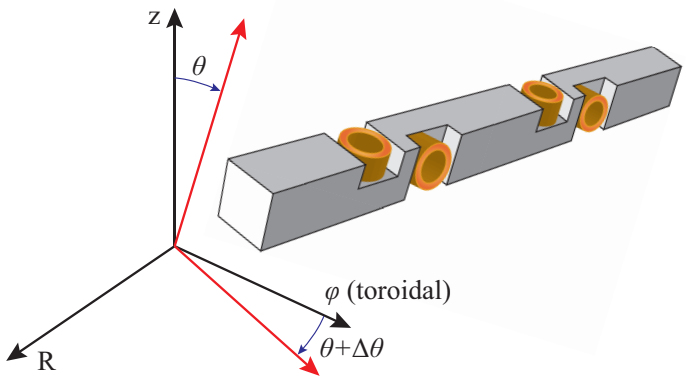

Figure 2.4: The schematic view of a rotated magnetic probe.

Fig.2.1(b). The magnetic probe array has 64 channels of coils for B_z component and 64 channels of coils for B_t component in the upper region (0.35 m $\leq Z \leq$ 0.95 m) and 81 channels of coils for B_z component and 81 channels of coils for B_t component in the middle region (-0.24 m $\leq Z \leq$ 0.24 m).

The pickup coil for B_z component is possible to measure B_t component, because the magnetic probe would be rotated when we insert the magnetic probe inside the vacuum vessel. Since it is impossible to eliminate that perfectly, a correction technique is required for the orientation of pick up coils. If the pickup coil for B_z is inclined at an angle of θ from the vertical, the measured value of magnetic field is expressed as:

$$B' = B_z \cos\theta - B_t \sin\theta. \tag{2.2}$$

Then, the true values of B_z and B_t are calculated from the values B'_z and B'_t measured by the pickup coils and angles of the coils:

$$\begin{pmatrix} B_z \\ B_t \end{pmatrix} = \frac{1}{\cos\Delta\theta} \begin{pmatrix} -\sin(\theta+\Delta\theta) & \sin\theta \\ \cos(\theta+\Delta\theta) & \cos\theta \end{pmatrix} \begin{pmatrix} B'_z \\ B'_t \end{pmatrix}, \tag{2.3}$$

where θ and $\Delta\theta$ are the angles as illustrated in Fig.2.4. The angles θ and $\Delta\theta$ are calculated by the following expressions. When only the TF coil is discharged, there is only toroidal magnetic field B_t component inside the vacuum vessel. The measured signal by

the magnetic probe can be describes as

$$\begin{pmatrix} B'_z \\ B'_t \end{pmatrix} = B_t \begin{pmatrix} \sin\theta \\ \cos(\theta + \Delta\theta) \end{pmatrix}. \tag{2.4}$$

When only EF1 and EF2 coils are discharged, no toroidal magnetic field B_t exists and the measured value is expressed as

$$\begin{pmatrix} B'_z \\ B'_t \end{pmatrix} = B_z \begin{pmatrix} \sin(\theta + \Delta\theta)\theta \\ -\cos\theta \end{pmatrix}. \tag{2.5}$$

Now, we define γ and ζ as

$$\gamma \equiv \frac{B'_t}{B'_z} = \frac{\cos\Delta\theta}{\tan\theta} - \sin\Delta\theta, \tag{2.6}$$

$$\zeta \equiv \frac{B'_z}{B'_t} = -\tan\theta\cos\Delta\theta - \sin\Delta\theta. \tag{2.7}$$

Then, θ and $\Delta\theta$ can be described as

$$\theta = \pm \arcsin\left(\sqrt{\frac{1-\zeta^2}{\gamma^2-\zeta^2}}\right), \tag{2.8}$$

$$\Delta\theta = \arctan\left(-\frac{\gamma\tan\theta - \frac{\zeta}{\tan\theta}}{\gamma - \zeta}\right), \tag{2.9}$$

where the top sign represents $\gamma > 0$ and the bottom sign represents $\gamma < 0$. If $\Delta\theta$ is already known, the orientation of the pickup coils would be achieve by only TF coil discharge and θ is obtained by:

$$\theta = \arctan\left(\frac{\cos\Delta\theta}{\gamma + \sin\Delta\theta}\right). \tag{2.10}$$

When the both B_z and B_t are obtained, poloidal flux Ψ, radial magnetic field B_r, toroidal electric field E_t and toroidal current density j_t would be calculated by assuming the toroidal symmetry:

$$\Psi = 2\pi \int_{R_0}^{R} B_z \rho \mathrm{d}\rho, \tag{2.11}$$

$$B_r = -\frac{1}{2\pi}\frac{\partial\Psi}{\partial z}, \tag{2.12}$$

$$E_t = -\frac{1}{2\pi R}\frac{\partial\Psi}{\partial t}, \tag{2.13}$$

$$j_t = -\frac{1}{\mu_0}\left(\frac{\partial B_z}{\partial R} - \frac{\partial B_r}{\partial z}\right), \tag{2.14}$$

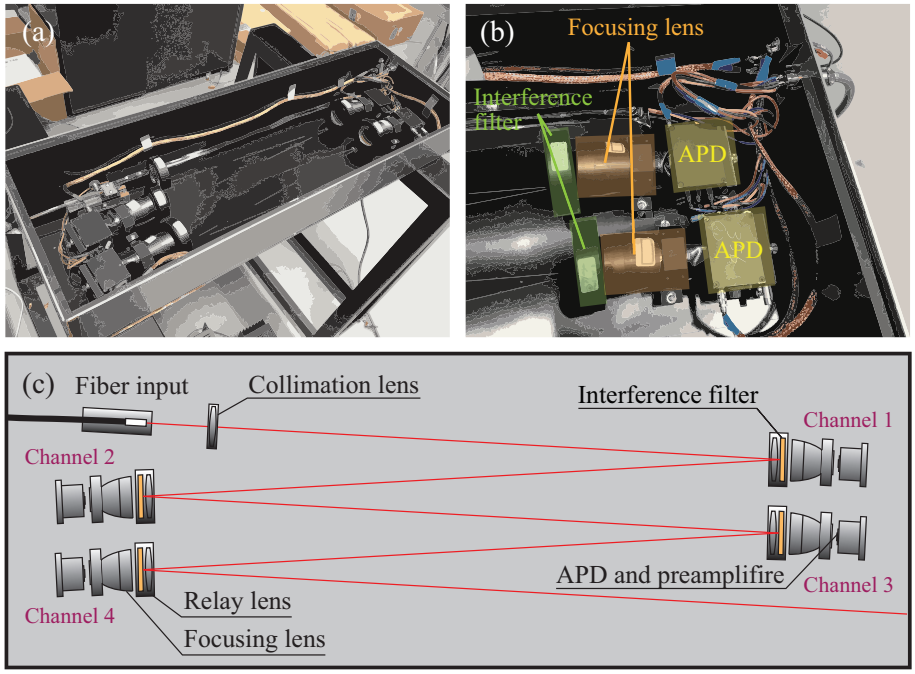

Figure 2.5: Schematic view of the polychromator. This contains a collimation lens and four interference filters, lens elements and electric circuits including an avalanche photo diode.

where R_0 is the radius of the center post. The sampling rate of the magnetic probe measurement is up to 2 MS/s using 14 bit analogue to digital converters (ADCs).

2.3.2 Slide-type Thomson Scattering Measurement System

To investigate the energy conversion mechanism for electrons during magnetic reconnection, we developed a slide-type two-dimensional Thomson scattering measurement system to evaluate electron heating in high guide-field magnetic reconnection in the UTST [63]. Thomson scattering diagnostics have been used widely as a most reliable diagnostics for electron temperature and density profile measurements. However, two-dimensional diagnostics of Thomson scattering have not been used widely in the experiment devices, because of requirement of many laser channels and spectrometers, which inevitably results in large-scale experimental facilities and high costs.

To solve this problem, we adopted a new method to slide radially the whole one-dimensional Thomson scattering system that measure axial profiles of electron temperature and density in a single discharge [64]. Laser light from a horizontally-polarized Nd:YAG laser oscillator with a wavelength of 1064 nm is amplified to approximately 3 J,

and then injected into plasma axially from a lower Brewster window of the UTST device. The laser beam is focused near spot in the mid-plane ($Z = 0$) of the UTST by a focusing lens. The scattered light from charged particles is focused into axial close-set optical fibers by condensing lens, and transferred to polychromators. The axial resolution is determined according to the fiber positions and the highest axial resolution is 5 mm. At the laser beam path, the images of the optical fibers are about 2.2 mm, which is smaller than the axial resolution. The measured signals along the horizontally-polarized Nd:YAG laser are perpendicular to the toroidal magnetic field: the scattering angle ($\sim \pi/2$).

The laser beam passed from an upper Brewster window of the UTST device is focused to a beam dump by an upper lens. The absorptive neutral density glass beam dump consists of narrow blades creating a surface at a steep angle to the direction of the laser beam propagation. The upper lens and beam dump are located outside the vacuum vessel of the UTST and can be adjusted to the sliding laser path of helium neon alignment laser beam through the vacuum vessel.

Multiple polychromators were assembled for the slide-type 2D Thomson scattering system. Each polychromator contains a collimation lens, four interference filters, lens elements (relay lenses and focusing lenses) and avalanche photo diodes (APDs) with preamplifier circuit. Figure 2.5 shows the schematic view of the polychromator. Each polychromator measures four different wavelength bands: 1059-1051 (channel 1), 1055-1045 (channel 2), 1053-1037 (channel 3), 1051-1009 nm (channel 4). Each interference filter has high blocking power ($> 10^5$) at 1064 nm, the wavelength of Nd:YAG laser, to reduce the stray light.

The position of the condensing lens and optical fibers are adjusted by measurement of Raman scattered light from nitrogen gas. The polarization of Raman scattered light is considered in absolute calibration that allows us to calculate the electron density from the intensity of Thomson scattering signals.

For 2D measurements of electron temperature and density, we slide radially the whole one-dimensional Thomson scattering system that measures their axial profiles in a single discharge. Using this slide system, we can measure radial profiles in 0.32 m $\leq R \leq$ 0.58 m region by changing the radial position of whole 1D Thomson system every discharge.

In order to maximize the signal-noise ratio, the signals from APDs are integrated with time (called integrals in this paper), because the electric noise is non-stationary in time.

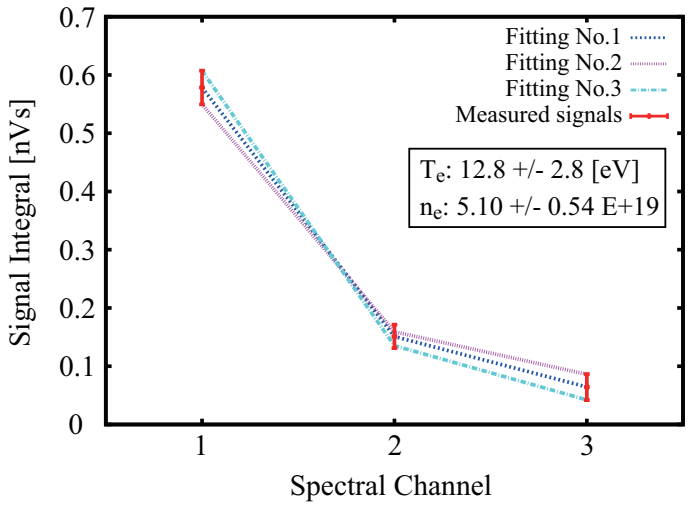

Figure 2.6: The spectral fit performed to the signal integrals to obtain the electron temperature and density. The horizontal axis is the channel number of the APDs in a polychromator.

The calculation of electron temperature and density from integrals of Thomson scattering signals is performed by the least-squares method. Figure 2.6 shows a sample of the fittings to obtain the electron temperature and density from integrals of Thomson scattering signals. The fitting of number 1 was calculated with the condition that minimizes the sum of squared residuals. The fitting number 2 and 3 are the minimum/maximum electron density (maximum/maximum electron temperature) calculated with the condition that maximizes the sum of squared residuals within the measurement errors, respectively. The noise integral is about 0.02-0.03 nVs, which is about 5% of signal in channel 1, 15% of signal in channel 2 and 40% of signal in channel 3, respectively.

To estimate the converted energy by magnetic reconnection quantitatively, the measurement of the electron temperature and density with a high confidence and accuracy is required. In other words, estimating an error of the measurement system is important. The fitting error of this measurement system, which is about $\pm$ 2 eV and $\pm$ 0.5×10^{19} in the electron temperature and density, respectively, allows us to estimate the gain energy of electrons by magnetic reconnection.

2.4 Experimental results in UTST

Figure 2.7 (a) shows the time evolution of the 2D magnetic field structure measured by the 2D magnetic probe array in central region on UTST, where the toroidal current density

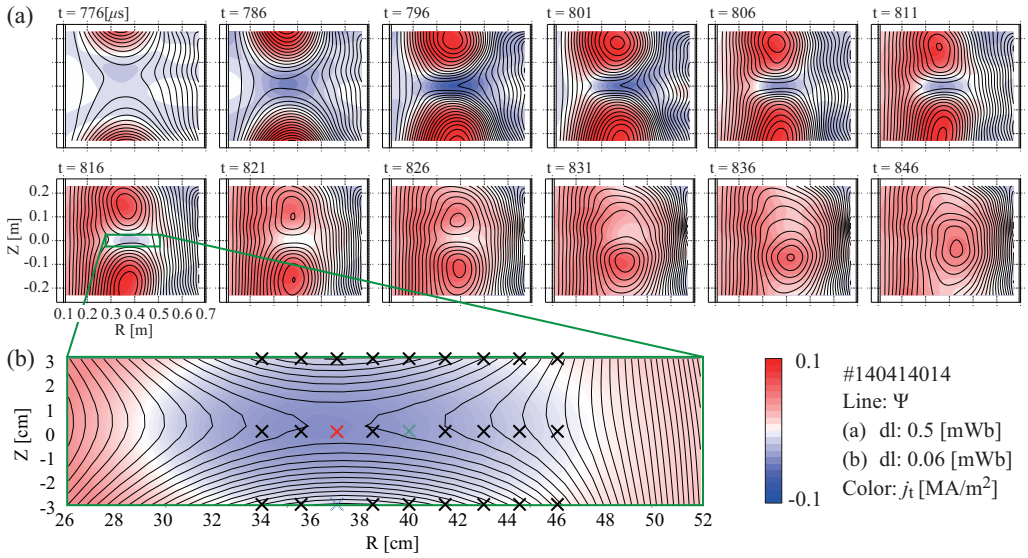

Figure 2.7: (a) Time evolutions of poloidal magnetic flux (line contour) and toroidal current density (color contour) during the tokamak plasma merging experiment (strong guide-field magnetic reconnection). (b) The cross markers indicate measurement positions for Thomson scattering measurement system.

is shown by red/blue color. Also, Figure 2.7 (b) shows detailed structure of Fig.2.7 (a) during magnetic reconnection (t=816 μs) and the measurement positions of 2D Thomson scattering system. During magnetic reconnection, the observed radially elongated current sheet region is similar to that predicted in classical Sweet-Parker model.

In Figs.2.8 (a)-(d), those values are calculated from the measured B_z and B_t by the magnetic probe array. Figure 2.8 (a) shows the time evolution of reconnected magnetic flux: poloidal flux function Ψ at the X-point.

The reconnected flux increases during magnetic reconnection and decreases after reconnection. Figure 2.8 (b) shows the time evolution of toroidal electric field E_t at the X-point which is defined as $(-\partial\Psi/2\pi R\partial t)$ at the X-point. The electric field at the X-point has a negative value during magnetic reconnection and peaks around t=800 μs while the magnetic flux increases fast at the X-point in fast reconnection phase.

Figs.2.8 (e) and (f) show the time evolution of electron temperature and density measured at the X-point (Z = 0, R = 37 cm), upstream region (Z = -3 cm, R = 37 cm) and downstream region (Z = 0, R = 40 cm). The temporal evolution is obtained from multiple discharge and staggering the trigger time of Nd:YAG laser and the error bar includes their discharge-to-discharge dispersion and the fitting errors from multiple discharges in a time.

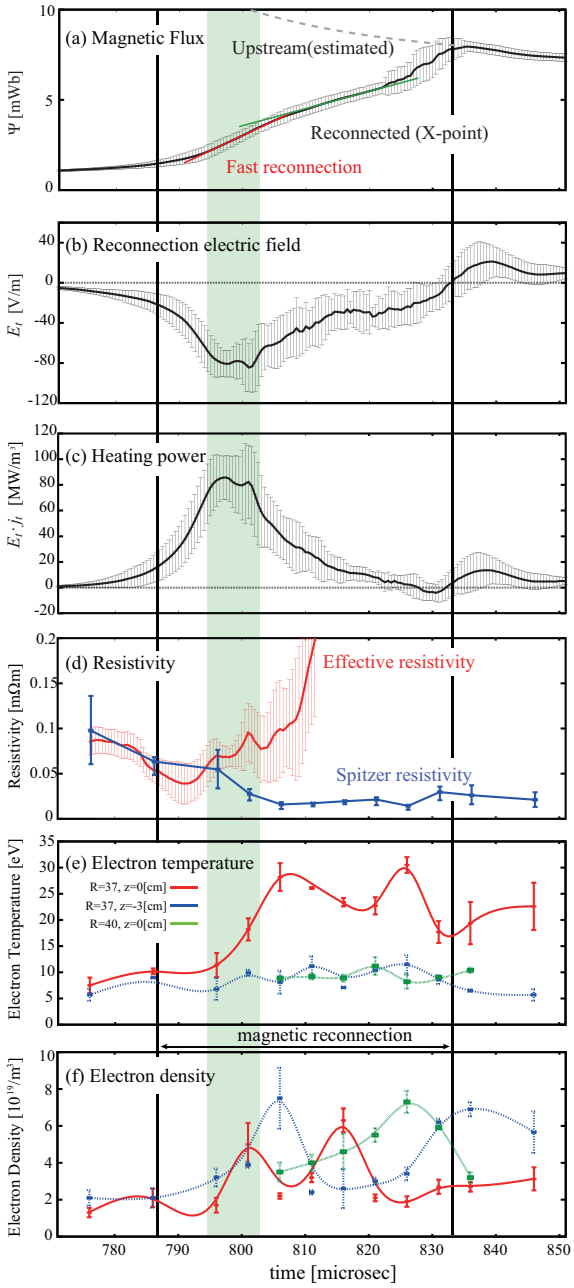

Figure 2.8: Time evolutions of (a) reconnected magnetic fluxes, (b) reconnection electric field E_t, (c) toroidal component of magnetic dissiaption energy $E_t \cdot j_t$, (d) effective and Spitzer resistivity at the X-point, (e) the electron temperature and (f) density at the X-point (red), upstream (blue) and downstream region (green) (see Fig.2.7 (b)).

We found that electron heating (from 8 eV to 27 eV) at the X-point took place during high guide-field magnetic reconnection whereas the electron temperature outside current sheet (Z = -3 cm) reveals clearly lower temperature than that at the X-point. Meanwhile, the electron heating was not observed in the downstream region.

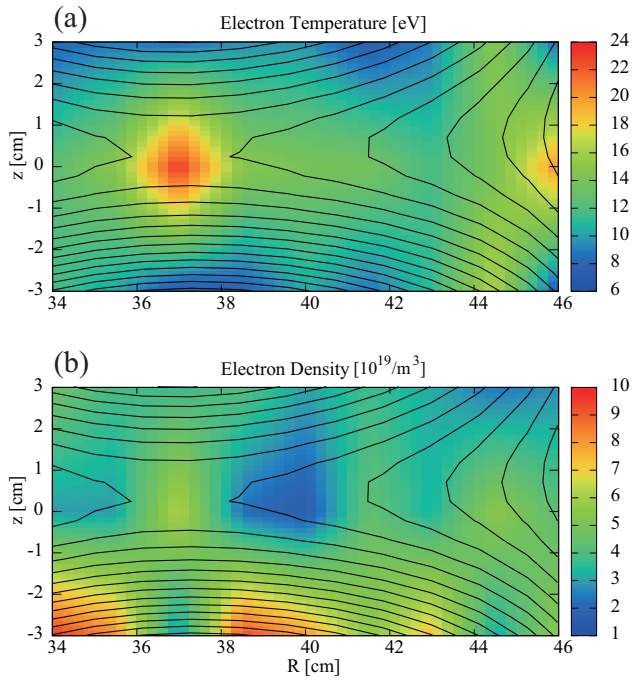

Figure 2.9: R-Z contours of poloidal flux (line), (a) electron temperature and (b) density at t=816 μs during the fast reconnection phase in the UTST merging experiment.

Figures 2.9 show the 2D counters of the electron (a) temperature and (b) density with the poloidal magnetic flux contours. Using slide-type 2D Thomson scattering measurement system, we observed that localized electron heating at the X-point forms a round-shaped high electron temperature area in sharp contrast with highly-elongated current sheet shown as Fig.2.7 (b). The radial width of the heated electron region was less than 3 cm, whereas the current sheet had radially elongated shape whose radial length is about 25 cm.

Using the measured 2D magnetic data and electron temperature and density profiles, we calculated how much energy is converted into the electron thermal energy during high guide-field magnetic reconnection in UTST. By assuming the toroidal symmetry and integrating a volume in the plasma near the X-point, the increment in electron thermal energy is obtained for 2.2 J, which is about 15% of the dissipated magnetic energy of 14 J. This conversion ratio in high guide-field ($B_t \sim 15B_p$) reconnection is higher than that in other guide-field (typically $B_t \sim 5B_p$) reconnection experiment in the TS-3 device [65]. This can be explained by that the electron heating is caused by the parallel electron acceleration by reconnection electric field E_t along the magnetic field line (mainly in toroidal direction) and thermalized during the guide-field reconnection.

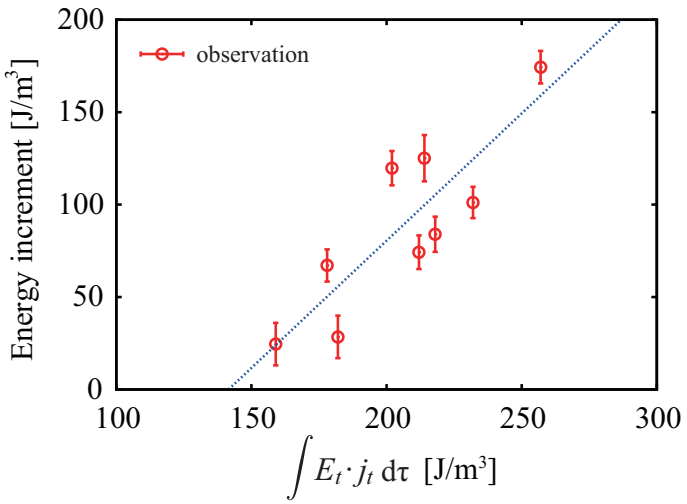

Figure 2.10: Correlation between the electron energy gain and $\int E_t \cdot j_t d\tau$ (reconnection electric field times toroidal current density) at the X-point.

2.4.1 Energy Source of Electron Heating

Figure 2.8 (c) shows the time evolution of the toroidal (parallel to the magnetic line) component of magnetic energy dissipation $E_t \cdot j_t$ at the X-point. It indicates that the electron temperature increased after $E_t \cdot j_t$ peaked during the fast reconnection phase. Also, Figure 2.10 shows the relation between the electron energy increment and $\int E_t \cdot j_t d\tau$ at the X-point. These data are obtained from different shots while $\int E_t \cdot j_t d\tau$ is time-integrated $E_t \cdot j_t$ during magnetic reconnection at the X-point. The electron energy increment grows clearly proportionally to $\int E_t \cdot j_t d\tau$ at the X-point. Therefore, the electric field at the X-point causes significant energy transfer from the magnetic field energy to the kinetic/thermal energy of electrons through the energy dissipation term, $E_t \cdot j_t$, where j_t is toroidal current density. However, $\int E_t \cdot j_t d\tau$ (see Fig.2.12 (a)) can not explain the localization of high electron temperature area near the X-point during high guide-field reconnection. The parallel electron acceleration and the ohmic heating are the possible candidates for the measured energy transfer from the magnetic field energy to the kinetic/thermal energy of electrons.

2.4.2 Electron Acceleration at the X-point

In high guide-field reconnection, electrons are accelerated parallel to the magnetic field (electrons are strongly magnetized) which is mainly consisted of the guide toroidal field in the UTST experiment. This parallel acceleration mechanism is predicted by several PIC simulations [42; 43]. Also, the accelerated electron was observed directly inside the diffusion region in Earth's magnetotail by the satellite observation [66].

As we discussed previously, the guide (toroidal) field is typically 15 times higher than the reconnecting magnetic (poloidal) field in the UTST plasma merging experiment. The reconnection electric field would accelerate the electrons toroidally, that is parallel to the magnetic field, converting the magnetic energy to the kinetic energy of electrons. In fact, a burst of bremsstrahlung soft X-ray emission was observed only during fast reconnection phase in the UTST experiment, suggesting the presence of high energetic electrons by high guide-field reconnection [67].

Since the reconnection electric field is almost uniform inside the reconnection layer (if the reconnection is quasi-steady state), the acceleration length for electrons will play an important role for increasing electron kinetic energy. The radial or axial component of magnetic field around the X-point decreases the electrons acceleration length, causing decrease in electron kinetic energy increment. In other words, electrons near the X-point are accelerated much longer than the other electrons far from the X-point, because the increase in electron kinetic energy depends on the length of magnetic field line inside the current sheet.

Now we consider the electron motion inside the reconnection layer. Figure 2.11 shows the Cartesian coordinate system in which B_y is the guide-field. The particle velocities of electrons (guiding center motion) on the X-Z plane can be described as:

$$|v_x| = \left| \frac{B_x}{\sqrt{B_x^2 + B_y^2 + B_z^2}} v_{\parallel} + v_{out} \right|, \tag{2.15}$$

$$|v_z| = \left| \frac{B_z}{\sqrt{B_x^2 + B_y^2 + B_z^2}} v_{\parallel} + v_{in} \right|, \tag{2.16}$$

where v_{in} and v_{out} are the velocities of inflow and outflow that are the velocities of drift motion, respectively. This drift motion is mainly mainly $\boldsymbol{E} \times \boldsymbol{B}$ drift in the UTST plasma

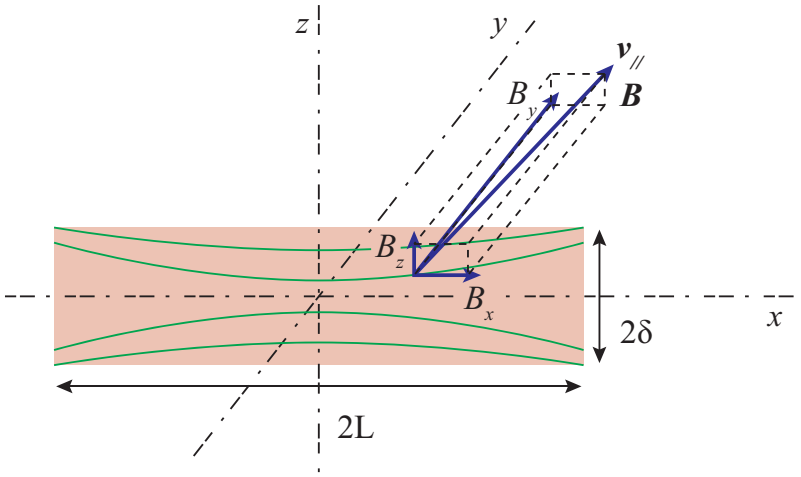

Figure 2.11: The coordinate system in which B_y is the guide-field. The width and length of the reconnection layer are 2δ and $2L$, respectively. The reconnection electric field is uniform inside the reconnection layer.

merging experiment. Since the reconnection layer is much larger than the electron gyro-radius ρ_e in the strong guide-field magnetic reconnection in UTST ($L \sim 10\delta \sim 10^3\rho_e$), we don't include the gyro motion.

Then, the poloidal velocity $|v_p|$ can be described as

$$\begin{aligned} |v_p|^2 =& |v_x|^2 + |v_z|^2, \\ =& \frac{B_p^2 v_\parallel^2}{B_p^2 + B_t^2} + \frac{2\left(B_x v_{out} + B_z v_{in}\right)}{B_p^2 + B_t^2} + v_{out}^2 + v_{in}^2, \end{aligned} \tag{2.17}$$

where $B_p^2 = B_x^2 + B_z^2$ and $B_t^2 = B_y^2$ are poloidal and toroidal magnetic field in the UTST plasma merging experiment, respectively. Assuming $B_p \ll B_t$ due to high guide-field condition, the poloidal velocity $|v_p|$ can be approximated as

$$|v_p| \simeq \left(\frac{B_p}{B_t} + \alpha\right)\left|v_\parallel\right|, \tag{2.18}$$

where $\alpha = \sqrt{(v_{in}^2 + v_{out}^2)/v_\parallel^2}$. Since electrons would be accelerated by the reconnection electric field parallel to the magnetic field inside the reconnection layer, we can obtain $\alpha \ll 1$ in the strong guide-field magnetic reconnection. When we assume the reconnection electric field is uniform inside the reconnection layer and the width and length reconnection layer are 2δ as well as $2L$, respectively. The maximum acceleration length for electrons

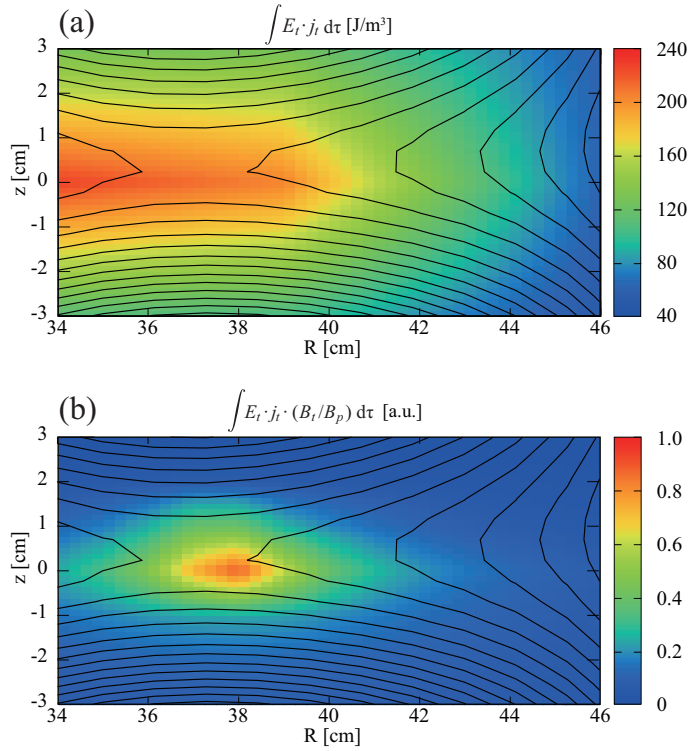

Figure 2.12: R-Z contours of poloidal flux (line) at t =816 μs, (a) $\int E_t \cdot j_t \mathrm{d}\tau$ and (b) the normailzed $\int E_t \cdot j_t \cdot (B_t/B_p)\mathrm{d}\tau$.

l_{acc} can be evaluated as

$$\begin{aligned} l_{acc} =& |v_{\parallel}|\tau_{acc}, \\ =& |v_{\parallel}||\frac{1}{v_p}|\sqrt{\delta^2 + L^2}, \\ =& \sqrt{\delta^2 + L^2}\frac{B_t}{B_p + \alpha B_t}, \end{aligned} \tag{2.19}$$

where $\tau_{acc} = \sqrt{\delta^2 + L^2}/|v_p|$ is the electron acceleration time which would be shorter than the electron-ion collision time τ_{ei}. Therefore, these results suggest that the electron kinetic energy increment $\Delta P_{e,k}$ in high guide-field reconnection would be described as

$$\Delta P_{e,k} = \int_0^{l_{acc}} \vec{E_t} \cdot \vec{dl} \propto \frac{E_t \cdot B_t}{B_p + \alpha B_t}. \tag{2.20}$$

2.4.3 Thermalization of the Accelerated Electrons

This parallel acceleration mechanism plays an important role for the electron kinetic energy increment, however, needs an additional explanation of the electron heating measured

by Thomson scattering, because the measured electron temperature is perpendicular to the magnetic field in the UTST merging experiment. Additionally, we need to discuss the thermalization process in order to explain the electron heating because it is the increase in the electron thermal energy.

The classical Spitzer resistivity which is a electrical resistivity based on collisions can be obtained from electron temperature and density, described as:

$$\eta_{\mathrm{Sp}} = \frac{\pi^{3/2} m_e^{1/2} Z e^2 c^2 \ln\Lambda}{2(2k_B T_e)^{3/2}},$$

where Z is the ionic charge and $\ln\Lambda$ is the Coulomb logarithm. Fig.2.8 (d) shows that the effective resistivity $\eta_{\mathrm{eff}} = E_t/j_t$ was comparable to the Spitzer resistivity before the fast reconnection phase (795-803 μs), however, increased quickly and became much larger than the Spitzer resistivity at the X-point when the fast reconnection phase started. Since the effective resistivity consists of collision effect (Spitzer resistivity) as well as collision-less effect, the anomalous resistivity $\eta_{\mathrm{Ano}} = \eta_{\mathrm{eff}} - \eta_{\mathrm{Sp}}$ due to collision-less effect will become dominant during fast reconnection phase. These results suggest that accelerated electrons are thermalized by the collision-less effect around the X-point in the high guide-field reconnection. One of the possibility is that the fluctuations (waves) is excited and couple with the accelerated electrons near the X-point. Unfortunately, the strength of magnetic field in the UTST device is too strong to address this issue.

In order to explain the localized electron heating at the X-point, we install guide-field effect term $B_t/(B_p + \alpha B_t)$ to the energy source term $E_t \cdot j_t$ and calculate integrate with time during magnetic reconnection. Figure 2.12 (b) shows the R-Z contour of $\lim_{\alpha\to 0} \int E_t \cdot j_t (B_t/B_p + \alpha B_t) \mathrm{d}\tau$. Since this time-integrated value can explain the localized electron heating at the X-point, the increment of electron thermal energy $\Delta P_{e,t}$ in the strong guide-field magnetic reconnection will be described as

$$\Delta P_{e,t} \propto \int \left(\frac{B_t}{B_p + \alpha B_t} \right) E_t \cdot j_t \mathrm{d}\tau. \tag{2.21}$$

Chapter 3

Laboratory Experiment in MRX

In this chapter, the experimental apparatus of Magnetic Reconnection Experiment (MRX) device at the Princeton Plasma Physics Laboratory (PPPL) is briefly described. Then, diagnostics used for this dissertation are discussed. Finally, the details of the experimental regime and key experimental result are presented and discussed.

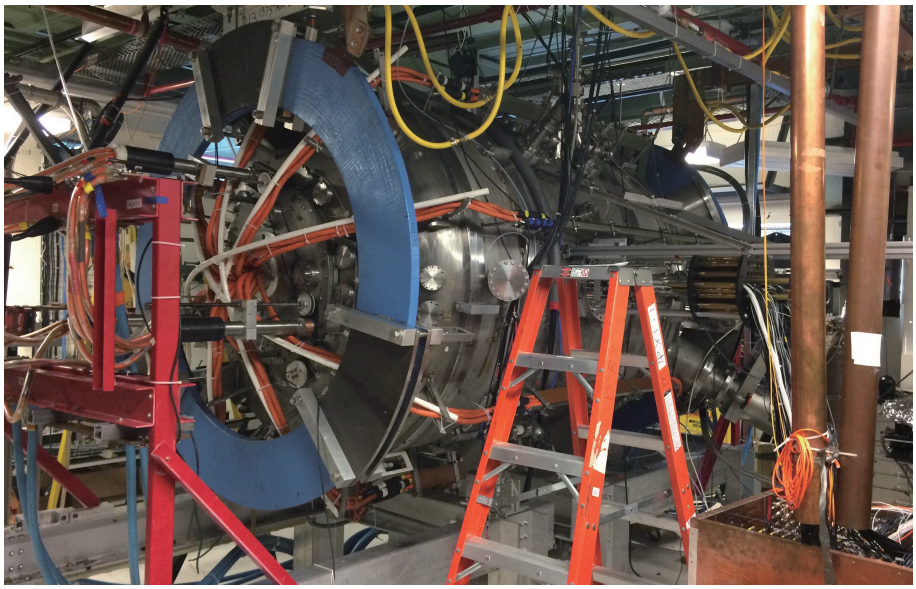

Figure 3.1: A Photograph of the Magnetic Reconnection Experiment. MRX has a cylindrical vacuum vessel. Various diagnostics are inserted into the machine through the large mid-plane port to measure important physical quantities.

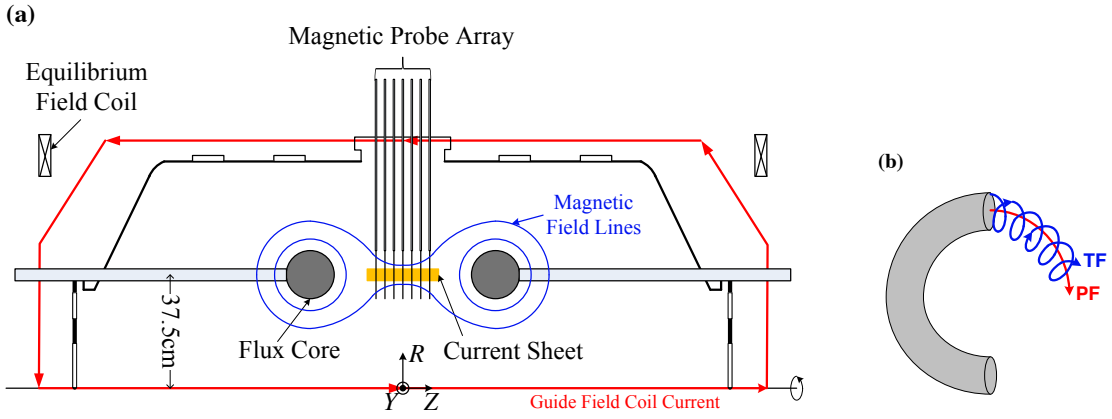

Figure 3.2: (a) The picture shown is a cross-section of the cylindrically symmetric vacuum vessel with magnetic field lines drawn. The gray circles indicate the location of the two flux cores. The orange color denotes the shape of the current sheet formed during pull reconnection. (b) Each flux core contains a PF winding to produce the magnetic X-point geometry and a TF helically wound coil, which produces an electric field used to break down the plasma.

.

3.1 Overview of Magnetic Reconnection Experiment (MRX)

MRX device is a mid-size laboratory device specifically designed for detailed studies of magnetic reconnection. Figure 3.1 shows a photograph of the MRX. The vacuum vessel is cylindrical and the inner radius is 76.2 cm. The wall is made of quater-inch-thick 304 stainless steel. The axial length of the vacuum vessel is about 1.7 m. There are two blue circular coils for the equilibrium field (EF), which is relatively uniform axial magnetic field. The EF coils are used to control the radial position of the current sheet by balancing the radial hoop force.

Figure 3.2 (a) shows a cross-sectional view of the MRX vacuum vessel. The local coordinate system used in MRX is also shown: R is radially outward, Y is the out-of-plane direction and Z is the axial direction. The distance between the two flux cores can be varied externally into 42 cm. Various probes such as a two-dimensional magnetic probe array are inserted radially to measure important local physics quantities.

Figure 3.2 (b) shows a schematic view of flux core inside of which there are two sets of

coils: poloidal field (PF) coils and toroidal field (TF) coils [62]. The PF colis are wound toroidally to generate the X-line geometry at the middle of the vacuum vessel and to drive magnetic reconnection. The TF coils are wound poloidally to inductively create the plasma around the flux cores.

When plasma is ignited, there is global pressure imbalance because both the magnetic and plasma pressures are high near the flux cores. This pressure imbalance drives plasma inflow from the flux cores to the middle: "pushing" the magnetic flux toward the middle. This push reconnection phase begins right after the plasma formation. After the global pressure imbalance is relieved, the magnetic flux is pulled toward the flux cores from the middle and a current sheet becomes an elongated shape along Z direction. In this phase, the initial out-of-plane magnetic field that is produced during the plasma formation phase becomes negligible compared to the reconnecting magnetic field such that anti-parallel reconnection is achieved. In this work, we add a guide-field externally using guide-field coil. This stage of the MRX discharge is called the pull reconnection phase. In the pull reconnection, the reconnection rate is relatively constant, that is called the quasi-steady state.

3.2 Diagnostics

To study energy conversion mechanism during magnetic reconnection in MRX, several diagnostics are required. Due to the relatively low electron temperature and short discharge time, *in-situ* measurement of plasma quantities are possible in MRX as other laboratory reconnection experiments (TS-3/4 and UTST).

3.2.1 Magnetic Probes

In MRX, two-dimensional magnetic probe array is installed with a maximum radial resolution of 6 mm while covering 16 cm radially. Figure 3.3 (a) shows a photograph of 2-D magnetic probe array. It consists of 7 probes with separation of 3 cm along Z. A lot of magnetic pick up coils are aligned inside of the magnetic probe. The diameter and height of the coils are 1.75 mm. Figure 3.3 (b) shows the alignment of the pickup coils.

With the 2-D magnetic probe array, the time evolution of all three components of the magnetic field are measured in MRX. The magnitude of the magnetic field is calibrated

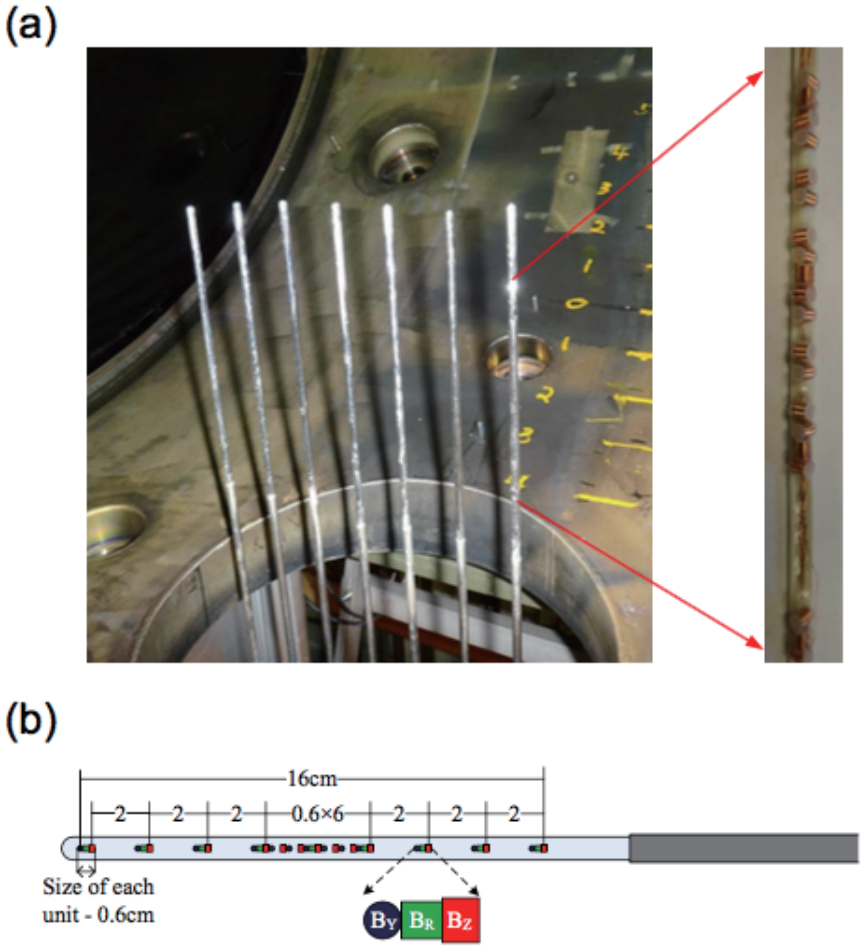

Figure 3.3: 2-D magnetic probe array [68]. (a) Photo of 2-D magnetic probes inside of the MRX chamber. There are a series of miniature pickup coils inside each probe. (b) Alignment of the pickup coils. Each probe has 35 total pickup coils: 9 for B_R and 13 for both B_Y and B_Z.

using a 7 turn Helmholtz coil with approximately 2 cm diameter and coil separation. A typical value of the effective area of the coil in MRX is 2.4 cm^2. Passive electronic integrators are used to integrate a voltage across the leads of the coil before the signals are digitized in order to reduce the noise and impact from the digitizer offset voltage and bandwidth limitations.

2-D magnetic field profiles can be used to compute the current density with the use of Ampere's law. Assuming toroidal symmetry, which is same method as UTST's, each component of the current density is given by

$$J_R = \frac{1}{\mu_0}\frac{\partial B_Y}{\partial Z}, \tag{3.1}$$

$$J_Y = \frac{1}{\mu_0}\left(\frac{\partial B_R}{\partial Z} - \frac{\partial B_Z}{\partial R}\right), \tag{3.2}$$

$$J_Z = \frac{1}{\mu_0 R}\frac{\partial (RB_Y)}{\partial R}. \tag{3.3}$$

Finally, the inductive out-plane reconnection electric field E_Y is calculated as

$$E_Y = \frac{1}{2\pi R}\frac{\partial \psi}{\partial t}, \tag{3.4}$$

where the poloidal flux function ψ can be determined as

$$\psi = \int_0^R 2\pi r' B_Z dr' \tag{3.5}$$

$$= \int_0^R 2\pi r' B_Z dr' - \int_{Z_0}^Z 2\pi r' B_R dz'. \tag{3.6}$$

The poloidal flux ψ is set to be zero at the machine axis ($R = 0$).

3.2.2 Langmuir Probes

Since the quasi-steady period of the discharge is short and the plasma potential changes quickly from about -150 to 150 V, a single-tip Langmuir probe that requires a sweep of the bias voltage is not suitable for MRX. Thus, we decided to use triple Langmuir probes for the electron temperature and density measurements. Figure 3.4 (a) shows a photograph of a triple Langmuir probe. The tip diameter is 0.8 mm and its length is 1.2 mm. The four tips made of tungsten form a square and the distance between adjacent tips is 2.3 mm. We clean the Langmuir probes by sand-blasting almost every time before we install it inside the vacuum vessel to avoid an artificially high electron temperature and low density.

Figure 3.4 (b) shows a schematic of the MRX triple Langmuir probe diagnostic. The two electrodes labeled Φ_+ and Φ_- are biased in a double probe configuration. Two additional unbiased tips provide floating potential measurements. Assuming the Maxwellian distribution function, the current-voltage characteristic of the Langmuir probe can be described as

$$I_p(\Phi) = -I_{sat} + en_e A\sqrt{\frac{T_e}{2\pi n_e}}\exp\left[-\frac{e(\Phi_p - \Phi)}{T_e}\right], \tag{3.7}$$

where $I_p(\Phi)$ is the current flowing from the probe to the plasma, A is the probe area, and Φ_p is the plasma potential. The bias voltage Φ_B is chosen to be large enough for Φ_- tip to collect the ion saturation current I_{sat}. Then, the electron temperature can be deduced by measuring Φ_+ and Φ_-. Since the double probe is floating, the Φ_+ tip draws the same amount of the electron current. Using $I_p(\Phi_+) = I_p(\Phi_-)$ and $I_p(\Phi_f) = 0$, the relation between Φ_+ and Φ_f can be computed as [69]

$$\frac{I_p(\Phi_+) - I_p(\Phi_f)}{I_p(\Phi_+) - (\Phi_-)} = \frac{1}{2} = \frac{1 - \exp[-(\Phi_+ - \Phi_f)/T_e]}{1 - \exp[-\Phi_B/T_e]}. \tag{3.8}$$

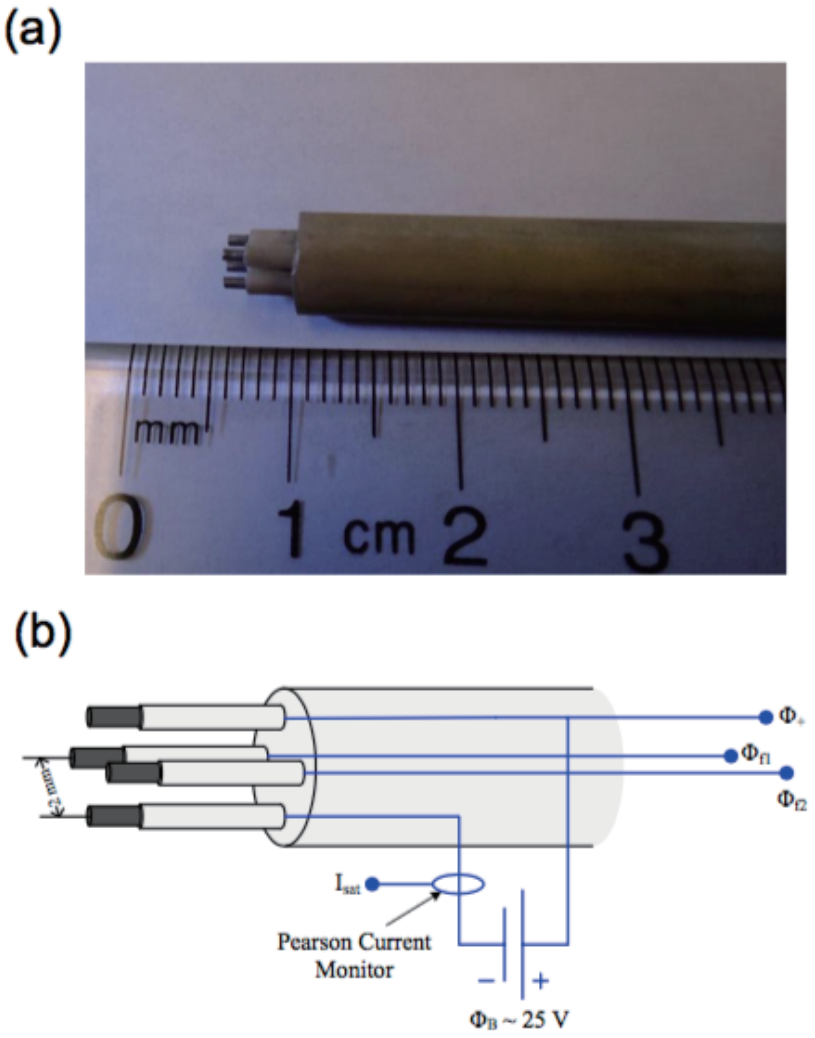

Figure 3.4: MRX triple Langmuir probe [68]. (a) Photo of a MRX triple Langmuir probe. It consists of two tips in a double probe configuration and two additional floating potential tips. (b) Schematic of the Langmuir probe measurement. Two floating potential tips are needed to minimize effects from local electric fields.

When $\Phi_B \gg T_e$, the above equation simplifies to $\Phi_+ - \Phi_f = \ln_2 T_e$, from which the electron temperature can be determined. The major reason for the additional floating potential tip is to minimize the effect from local electric fields. Because the in-plane electric field can be as high as several thousands V/m in MRX discharges, the 2 mm separation between tips can cause an error of about 3 eV in Te measurement. By averaging over the two Φ_f tips and placing Φ_+ in the middle of them, this effect can be significantly reduced.

The plasma density can be computed by measuring the ion saturation current as [69]

$$I_{sat} = \exp[-0.5] A e n_i C_s, \tag{3.9}$$

where $C_s = \sqrt{T_e/m_i}$ is the ion sound velocity when $T_e \gg T_i$. Since T_i is comparable to or slightly larger than T_e in MRX discharges, we can't use this simple expression. However, It is suggested that the ion saturation current does not strongly depend on T_i as long as $T_i < 2T_e$ [70]. Therefore, $C_s \simeq \sqrt{T_e/m_i}$ is a valid approximation for MRX discharges. The probe area A is cross-calibrated with a reference Langmuir probe by comparing their signals in a quiet, toroidally symmetric plasma. The probe area of the reference Langmuir probe is calculated by using the actual dimensions of the probe.

3.2.3 Floating Potential Probe

The radial floating potential profile is measured by a 22-tip floating potential probe. Figure 3.5 shows the alignment of the probe. It has 17 radial measurement points with the maximum resolution of 0.7 cm. There are five radial locations where two tips exist with a small separation ($\sim$ 4 mm) along the direction perpendicular to the probe shaft. The purpose of the additional five tips is to provide an approximate value of the local

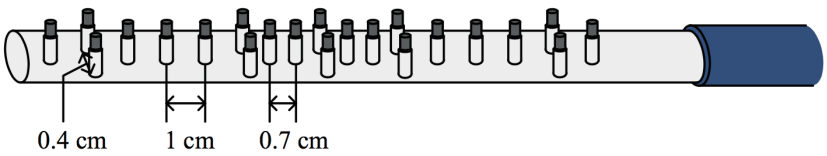

Figure 3.5: Schematic view of the 22-tip floating potential probe [68]. It consists of 22 floating potential tips with 17 measurement points. At 5 radial locations, additional information on the local electric field can be gained from examining differences between the two closely located tips.

electric field by assuming that the difference of electron temperature in those two location is negligible.

3.3 Experimental results in MRX

3.3.1 Plasma Parameters and Experimental Regime

Using two-dimensional (R-Z) scans of the previously described probes, 2D profiles of various plasma parameters such as n_e, T_e and Φ_f are obtained. The number of measurement points along the Z direction is 6-7 and the distance between the measurement points is typically 3 cm. Along the radial direction, electrostatic probes have 11 measurement points with the 1 cm separation except the edge points (2 cm). More than 1000 discharges are analyzed based on the reproducibility of the data from the 2-D magnetic probe array and a reference Langmuir probe in order to select the final data set. The main criteria are the location of the X-point and the electron density and temperature measured by the reference Langmuir probes at the upstream. The plasma parameters are controlled such that the plasma is in the collision-less regime, which provides the opportunity to identify the energy conversion mechanism in a laboratory plasma.

Figure 3.6 (a) shows a typical shot of the MRX discharge the quasi-steady period in the pull reconnection phase. The current sheet is elongated along the high-density separatrix due to the Hall effects. The strength of the guide-field B_Y is three times larger than the reconnecting field B_X shown as Fig.3.6 (b). The guide-field is about 280 G around the

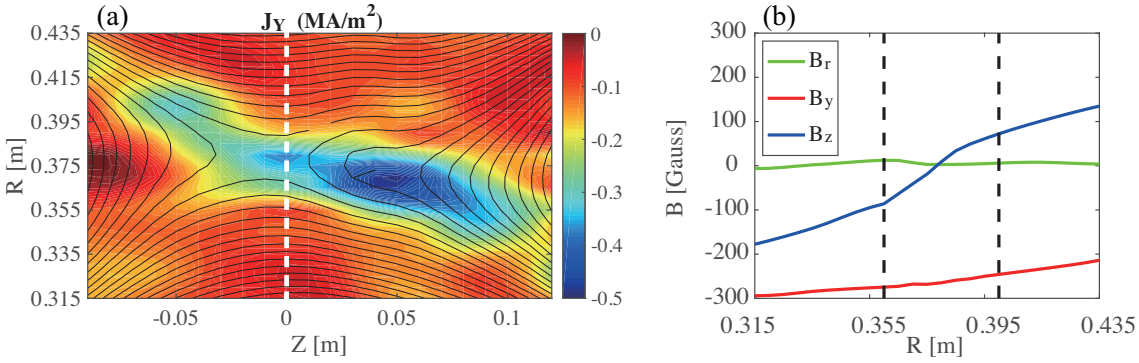

Figure 3.6: (a) The magnetic flux (line contour) and out-plane current density (color contour) in the quasi-steady state of guide-field reconnection. (b) Radial profiles of the three components of magnetic field along Z=0.

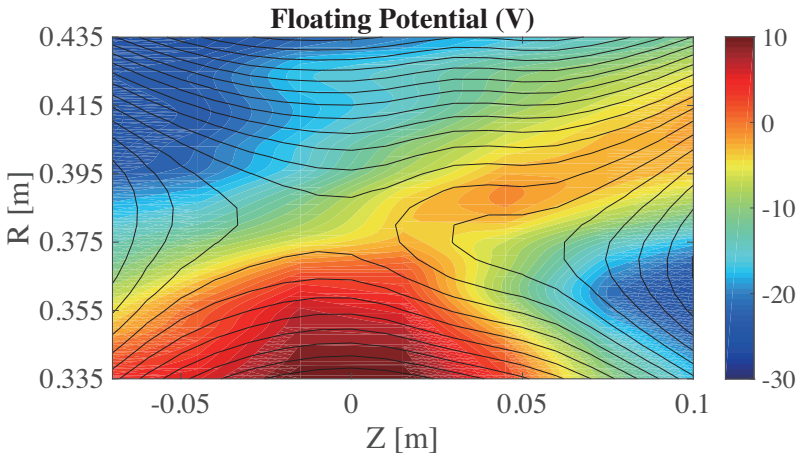

Figure 3.7: 2D floating potential profile at $t = 340\ \mu$ s along with contours of the poloidal flux Ψ. It is measured by the 22-tip floating potential probe at 6 different Z locations.

X-point and the shoulder value of the reconnecting magnetic field is about 90 G.

3.3.2 Quadruple Structure of Plasma Potential

Figure 3.7 shows the 2D profile of floating potential Φ_f measured by the 22-tip floating potential probe at 6 different Z directions. This floating potential profile reflects the key aspects of the in-plane electrostatic potential profile. However, in order to carry out quantitative analysis, Φ_f must be converted to the plasma potential Φ_p using

$$\Phi_p \simeq \Phi_f + (3.3 + 0.5 \ln \mu)\, T_e, \tag{3.10}$$

where $\mu = m_i/m_p$ and T_e is in units of eV [69]. Since Φ_p is depends on the electron temperature, whose spatial structure is depends on the location of the X-point as suggested from the UTST and MAST data, we scrutinize the magnetic data to define the location of the X-point and calculate Φ_p using reconstructed Φ_f.

Figure 3.8 shows the measured 2-D profile of the plasma potential Φ_p in the middle of the quasi-steady reconnection period along with contours of the poloidal flux Ψ. The plasma potential is observed to have a quadrupole structure, as has been measured in previous guide-field reconnection experiments at the VTF [71] and UTST [72]. Such a structure is required to obtain $E_\parallel = 0$ on MHD scales and is also consistent with $\boldsymbol{E} \times \boldsymbol{B}$ plasma flows through the current sheet.

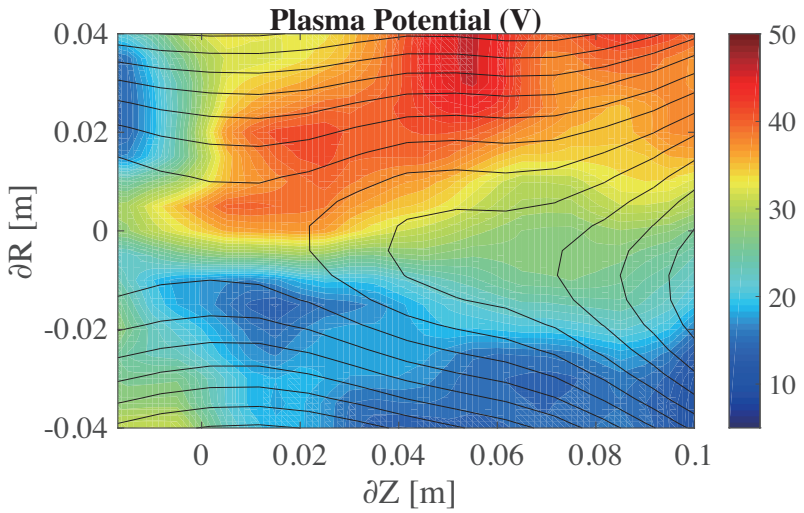

Figure 3.8: 2D plasma potential profile Φ_p with contours of the poloidal flux Ψ.

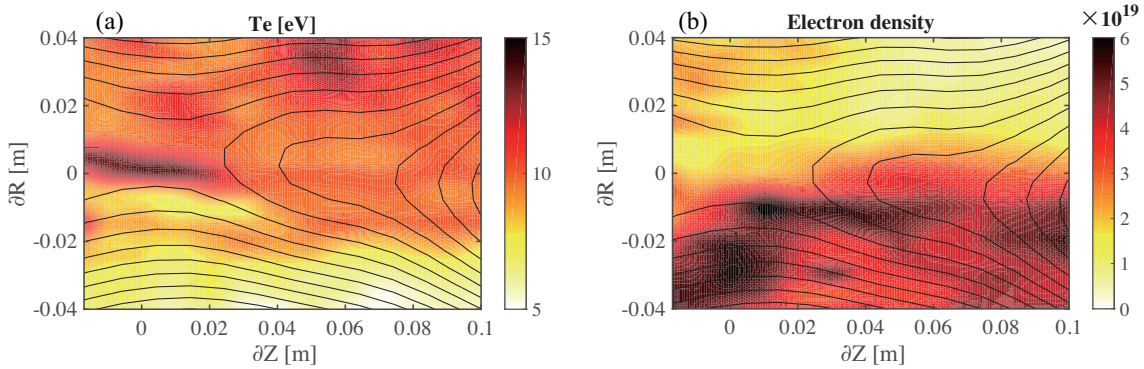

Figure 3.9: 2D (a) electron temperature and (b) density profile measured by the triple Langmuir probe along with the contours of the poloidal flux Ψ.

3.3.3 Electron Heating in Guide-Field Reconnection

Electrons are significantly heated during collision-less reconnection in MRX guide-field reconnection. Figure 3.9 (a) shows the 2D profile of electron temperature measured by a triple Langmuir probe. The electron temperatures of upstreams are 10-11 eV ($\delta R > 0$) and 5-6 eV ($\delta R < 0$). Meanwhile the electron density profile shows the opposite pattern of the electron temperature profile shown as Fig.3.9 (b). The breakdown and plasma formation in MRX caused this temperature and density asymmetry. Since the plasma pressure in two upstreams is comparable, we negligible the asymmetric effects.

The electron temperature is highest ($\sim$ 15 eV) near the X-point. This feature is consistent with other experiment results in TS-3, UTST and MAST. However, there is a

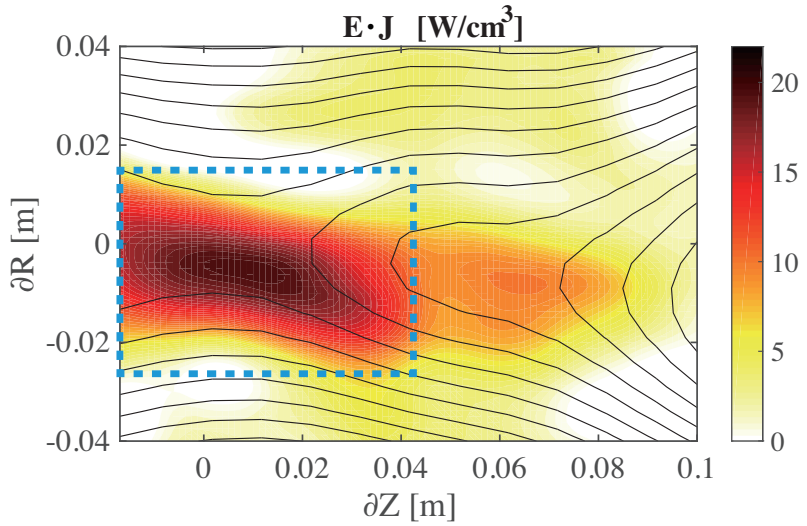

Figure 3.10: Work done by the electric field on both elections and ions per unit time and unit volume ($\boldsymbol{E} \cdot \boldsymbol{J}$). The magnetic energy dissipation is elongated in high-current separateix, however, mostly localized near the X-point.

difference between this profile and that of the other devices, that the shape of high electron temperature is elongated along with high-current separatrix.

Since we have 2D plasma potential profile, all three components of magnetic energy dissipation can be estimated in MRX. Figure 3.10 shows the 2D profile of the work done by the electric field on both the electrons and ions per unit time and unit volume $\boldsymbol{E} \cdot \boldsymbol{J}$ at $t = 340\mu$s. Assuming ions is too heavy (the mass ratio is over 7000) to carry the current, we can discuss about electron energy gain by the $\boldsymbol{E} \cdot \boldsymbol{J}$ profile. The electrons obtain energy mostly from the reconnection electric field in a region that is localized near the X-point.

By assuming toroidal symmetry, the electron energy gain from the electric field W_{gain} per unit time inside the volume of plasma marked the small blue box in Fig.3.10 can be calculated as

$$W_{gain} = \int (\boldsymbol{E} \cdot \boldsymbol{J}) dx^3 = \int \int 2\pi R dR dZ (\boldsymbol{E} \cdot \boldsymbol{J}) \simeq 2.1 \times 10^5 [W]. \tag{3.11}$$

The Ohmic dissipation based on the Spitzer resistivity cannot be the main reason for the electron energy gain. The current around the X-point is mostly parallel to the magnetic field for guide-field reconnection in MRX, we can negligible the contribution from perpendicular Spitzer resistivity. The total energy of Ohmic dissipation based on the parallel

Spitzer resistivity inside the volume is

$$W_{Spitzer} = \int \eta_{S,\parallel} J^2 dx^3 \simeq 1.4 \times 10^4 [W]. \tag{3.12}$$

This estimation shows that the collisional drag term cannot balance the total energy gain unless the so-called anomalous resistivity exists around the X-point due to high-frequency fluctuations, that is consistent with the UTST results discussed in the previous chapter.

3.3.4 Guide-Field Effects on Electron Heating

In order to study the effects of the guide-field on the energy conversion mechanism, we run the experiment in MRX with varifying the strength of the guide-field while keeping the strength of the reconnecting field around 90 G. Also, the electron density would play a important role in the energy conversion process, we maintained it with $B_Y/B_{rec} \sim 3$ case. Figure 3.11 shows the 1D radial profiles of the electron temperature with three different guide-field ratio in the middle of the quasi-steady state. It is obvious that the electron temperature profile is depend on the guide-field ratio. It is important to note that when the magnetic energy dissipation rate $\boldsymbol{E} \cdot \boldsymbol{J}$, is decomposed into $E_\parallel \cdot J_\parallel$ and $E_\perp \cdot J_\perp$, i.e., separating the inner product into that of the perpendicular and parallel components with respect to the local magnetic field lines, the parallel component, $E_\parallel \cdot J_\parallel$, is measured to be significantly larger than the perpendicular component, $E_\perp \cdot J_\perp$ unlike the anti-parallel

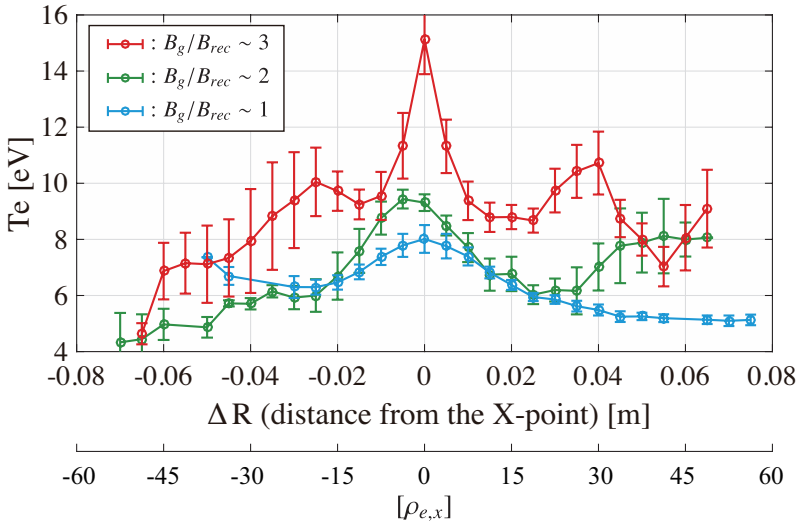

Figure 3.11: Radial profiles of T_e with three different guide-field ratio in the middle of the quasi-steady state period.

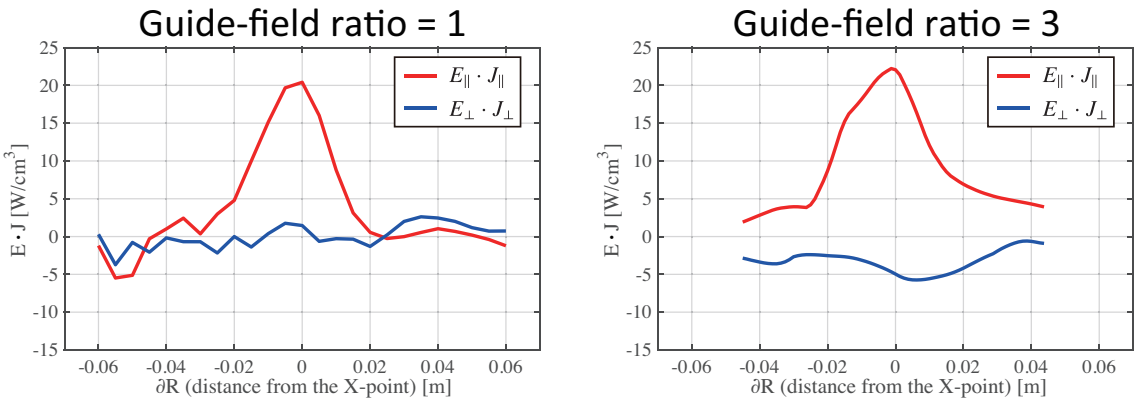

Figure 3.12: Comparison of two compositions of energy deposition rate measured in MRX with different guide-field ratio

reconnection experiment. Figure 3.12 shows the guide-field effect on $E_\parallel \cdot J_\parallel$ and $E_\perp \cdot J_\perp$. These results indicate the parallel acceleration is most likely the key physics for the energy conversion mechanism in the guide-field reconnection.

Chapter 4

Simulation Setup

In this chapter, a brief overview of the particle-in-cell (PIC) simulation method is described. Then, the open boundary technique, that is design to study for magnetic reconnection in PASMO code, is described. Then, the Harris-type initial condition for PIC simulation of magnetic reconnection is described. Finally, it is presented a coordinate transformation from the Cartesian coordinate system to the magnetic coordinate system.

4.1 Basic Equations

When we assume continuity in the phase space such that particles are neither created or destroyed then the considering the flow of particles into and out of a volume of the phase space, the most complete physical model for studying plasma physics is the Vlasov equation Eq.4.1, providing a 6-dimensional phase space kinetic description of the plasma, coupled with the Lorentz force Eqs.4.2-4.5, the relativistic equations of motion and Maxwell equations for electrodynamics:

$$\frac{\partial f(\boldsymbol{x},\boldsymbol{v},t)}{\partial t} + \nabla\cdot(\boldsymbol{v}f(\boldsymbol{x},\boldsymbol{v},t)) + \nabla_{\boldsymbol{v}}\cdot\left[\frac{q}{m}\left(\boldsymbol{E}+\boldsymbol{v}\times\boldsymbol{B}\right)f(\boldsymbol{x},\boldsymbol{v},t)\right] = 0 \tag{4.1}$$

$$\frac{1}{c}\frac{\partial \boldsymbol{B}}{\partial t} = -\nabla\times\boldsymbol{E} \tag{4.2}$$

$$\frac{1}{c}\frac{\partial \boldsymbol{E}}{\partial t} = \nabla\times\boldsymbol{B} - \frac{4\pi}{c}\boldsymbol{j} \tag{4.3}$$

$$\nabla\cdot\boldsymbol{B} = 0 \tag{4.4}$$

$$\nabla\cdot\boldsymbol{E} = 4\pi\rho. \tag{4.5}$$

Here, the charge density ρ and the current density $\boldsymbol{j}$ become:

$$\rho = \sum_{s}^{i,e} q_s \int f_s(\boldsymbol{x}, \boldsymbol{v}, t) d^3\boldsymbol{v} \tag{4.6}$$

$$\boldsymbol{j} = \sum_{s}^{i,e} q_s \int \boldsymbol{v}_s f_s(\boldsymbol{x}, \boldsymbol{v}, t) d^3\boldsymbol{v}. \tag{4.7}$$

In a full three-dimensional model, the plasma phase space is six-dimensional. If the number of grid points, that is the memory required for the simulation, scales as n^6, the memory requirements are far beyond the actual technology limits. It is therefore necessary to use a "compressed" representation of the discretized the distribution function $f_s(\boldsymbol{x}, \boldsymbol{v}, t)$. Since the distribution function is formed by a lot of particles, one of the method that use a very sparse phase space representation is the particle-in-cell method. It decomposes the distribution function into the sum of contributions coming from a finite set of computational particles. Therefore, we just need to solve the Maxwell's equations Eqs.4.2-4.5 and a lot of the equations of motion for the particles at the same time in the super-computer:

$$\frac{d\left(\gamma_0 \boldsymbol{u}_s\right)}{dt} = \frac{q_s}{m_s}\left(\boldsymbol{E} + \frac{\boldsymbol{u}_s}{c} \times \boldsymbol{B}\right) \tag{4.8}$$

$$\frac{d\boldsymbol{x}_s}{dt} = \boldsymbol{u}_s, \tag{4.9}$$

where $\gamma_0 = 1/\sqrt{1 - \boldsymbol{u}^2/c^2}$.

In this work, we use a computational super-particle, which represents many real particles, to make simulations efficient. It is allowed to rescale the number of particles, because the Lorentz force depends only on the charge-to-mass ratio, so a super-particle will follow the same trajectory as a real particle would. Furthermore, the ratio between plasma frequency, ion gyro-frequency and electron gyro-frequency is same as the real plasma. In order to avoid the noisy solution and huge potential at a single point due to reduced number of the particles, we installed the finite size particle method in the simulation (discussed in later section).

4.2 Particle-In-Cell method

Particle-In-Cell (PIC) method is a very intuitive method of plasma simulation where the basic scheme is to move the electrons and ions within a discrete spatial grid upon which are calculated electromagnetic fields that are self-consistent with the particle motion. Dealing

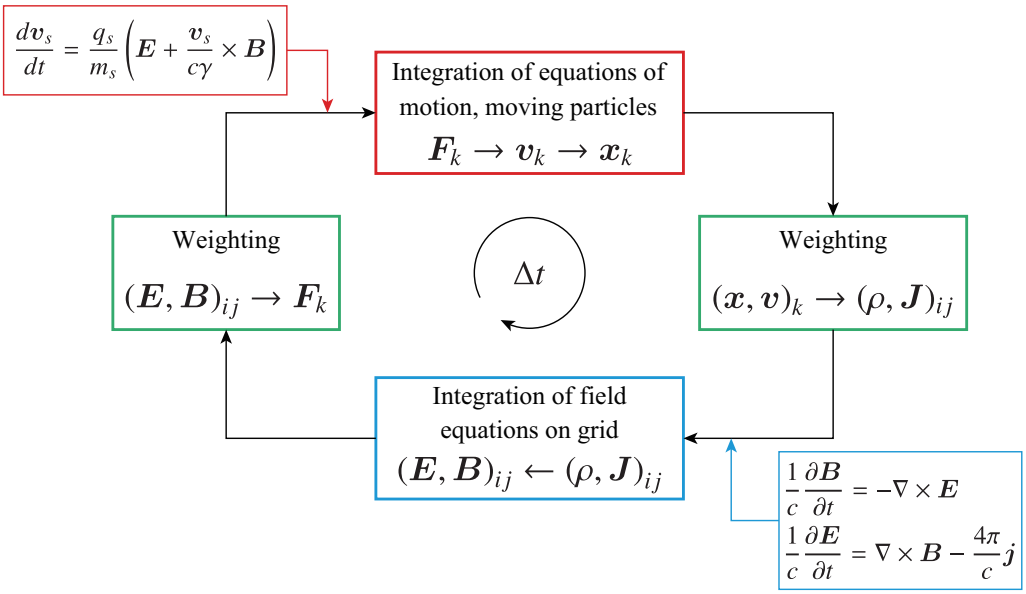

Figure 4.1: Generalized PIC code time-step cycle, particle indices k and grid indices i, j.

with charged particles, the physical description of the problem is closed by the Maxwell equations for the electromagnetic fields, which are coupled with the particle motion in a bidirectional way (by the Lorentz force and by the evaluation of charge and current densities). This forms a simple cycle which is at the core of PIC codes; particle motion determines field which determines subsequent particle motion. Over a single time step this cycle can be summarized in Fig.4.1. It is important to note that whilst the fields are only known at points upon the grid, the particles move continuously throughout the domain. The processes of an integration cycle of an electromagnetic PIC code are the following:

1. Time advancement of computational particles velocity and position using the equations of motion and the Lorentz force.
2. Deposition of the quantities needed in Maxwell equations, charge density and current density.
3. Time advancement of electromagnetic fields, discretized on spatial grids, (see section 3.4), using Maxwell equations and the quantities computed in step 2.
4. Interpolation of the electric and magnetic fields into the position of particles from the grid points.

The PIC method has the requirements for the choice of grid size and the time step. The time step needs to resolve both light-wave propagation, the gyro-motion of electrons and

the oscillation of electrons. The grid size needs to resolve the electron Debye length to avoid the so-called finite grid instability due to the aliasing of different Fourier modes.

4.3 Leap-Frog Method

Leap-frog method [73] is an elegant method for integrating Newton's laws of motion, that comes from one of the ways to write this algorithm, where positions and velocities "leap over" each other. Positions are defined at times $t_i, t_{i+1}, t_{i+2}, \ldots$, spaced at constant intervals dt, while the velocities are defined at times halfway in between, indicated by $t_{i-1/2}, t_{i+1/2}, t_{i+3/2}, \ldots$, where $t_{i+1} - t_{i+1/2} = t_{i+1/2} - t_i = dt/2$. Then, the leap-frog integration scheme is described as:

$$\boldsymbol{x}_i = \boldsymbol{x}_{i-1} + \boldsymbol{v}_{i-1/2} dt, \tag{4.10}$$

$$\boldsymbol{v}_{i+1/2} = \boldsymbol{v}_{i-1/2} + \boldsymbol{a}_i dt, \tag{4.11}$$

where $\boldsymbol{a}$ is the acceleration, which is defined only on integer times, just like the positions, while the velocities are defined only on half-integer times. The accuracy of this method can be estimated a second order method as:

1. $x_1 - x_0$ is of order h, where h is the interval between time steps,
2. the expected leading error $\sim h^2$ vanishes for the midpoint approximation, and so the error for one interval is $\sim h^3$,
3. To integrate over a finite time T the number of intervals is T/h and so the overall error is of proportional to $h^3 \times (1/h) = h^2$.

Therefore, the leap-frog method is a second order method, like 2nd order Runge-Kutta, and better than Euler, which is only first order.

4.4 Particle Solver

In particle simulations of magnetized plasmas, the Buneman-Boris algorithm is the standard method for advancing a charged particle in an electromagnetic field in accordance

with the relativistic equation of motion associated with the Lorentz force:

$$\frac{d\left(\gamma_0 \boldsymbol{u}_s\right)}{dt} = \frac{q_s}{m_s}\left(\boldsymbol{E} + \frac{\boldsymbol{u}_s}{c} \times \boldsymbol{B}\right) \tag{4.12}$$

$$\frac{d\boldsymbol{x}_s}{dt} = \boldsymbol{u}_s, \tag{4.13}$$

where $\gamma_0 = 1/\sqrt{1 - \boldsymbol{u}^2/c^2}$. The relativistic parameter γ_0 takes a huge number when the velocities become close to the speed of light. As a result, the small difference in the velocities leads the large difference in the particle energy. To prevent such an error, we instead define $\boldsymbol{v} = \gamma \boldsymbol{u}$ and $\gamma = \sqrt{1 + \boldsymbol{v}^2/c^2}$ to rewrite Eqs.4.12-4.13 as

$$\frac{d\boldsymbol{v}_s}{dt} = \frac{q_s}{m_s}\left(\boldsymbol{E} + \frac{\boldsymbol{v}_s}{c\gamma} \times \boldsymbol{B}\right) \tag{4.14}$$

$$\frac{d\boldsymbol{x}_s}{dt} = \frac{\boldsymbol{v}_s}{\gamma}. \tag{4.15}$$

This equation of motion is calculated via a finite differencing scheme in which both position and velocity are calculated every Δt but out of step by $\Delta t/2$. The equations to solve become:

$$\frac{\boldsymbol{v}_p^{t+\Delta t/2} - \boldsymbol{v}_p^{t-\Delta t/2}}{\Delta t} = \frac{q_p}{m_p}\left(\boldsymbol{E}^t + \frac{\boldsymbol{v}_p^t}{c\gamma_p^t} \times \boldsymbol{B}^t\right) \tag{4.16}$$

$$\frac{\boldsymbol{x}_p^{t+\Delta t} - \boldsymbol{x}_p^t}{\Delta t} = \frac{\boldsymbol{v}_p^{t+\Delta t/2}}{\gamma_p^{t+\Delta t/2}}, \tag{4.17}$$

where $\boldsymbol{x}_p$ and $\boldsymbol{v}_p$ are the position and velocity of a particle p, respectively. And the superscript values of the variables t and Δt are the time and the time step in the numerical simulation.

In order to calculate Eq.4.16 directly, it is easier to decompose it into three steps, that represents the particle acceleration by electric field and the rotation motion by magnetic field. First, Eq.4.16 can be derived

$$\frac{\boldsymbol{v}_p^+ - \boldsymbol{v}_p^-}{\Delta t} = \frac{q_p}{2\gamma_p^t m_p c}\left(\boldsymbol{v}_p^+ + \boldsymbol{v}_p^-\right) \times \boldsymbol{B}^t, \tag{4.18}$$

where

$$\boldsymbol{v}_p^- = \boldsymbol{v}_p^{t-\Delta t/2} + \frac{q_p}{m_p}\frac{\Delta t}{2}\boldsymbol{E}^t \tag{4.19}$$

$$\boldsymbol{v}_p^+ = \boldsymbol{v}_p^{t+\Delta t/2} - \frac{q_p}{m_p}\frac{\Delta t}{2}\boldsymbol{E}^t. \tag{4.20}$$

When we dot product Eq.4.18 with $(\boldsymbol{v}_p^+ + \boldsymbol{v}_p^-)$, we find $|\boldsymbol{v}_p^+| = |\boldsymbol{v}_p^-|$ and that we can get $\boldsymbol{v}_p^+$ by rotating $\boldsymbol{v}_p^-$ angle θ around $\boldsymbol{B}$ as shown in Fig.4.2:

$$\tan\frac{\theta}{2} = \frac{|\boldsymbol{v}_p^+ - \boldsymbol{v}_p^-|}{|\boldsymbol{v}_p^+ + \boldsymbol{v}_p^-|} = \frac{q_p B_p^t \Delta t}{2\gamma_p^t m_p c} = \frac{\omega_p \Delta t}{2} \tag{4.21}$$

$$\theta = 2\arctan\frac{\omega_p \Delta t}{2} \simeq \omega_p \Delta t \left(1 - \frac{(\omega_p \Delta t)^2}{12}\right), \tag{4.22}$$

where $\omega_p = q_p B_p^t / \gamma_p^t m_p c$ is gyro-frequency of the particle p. In order to decrease the calculation cost, we decompose it into two steps:

$$\boldsymbol{v}_p' = \boldsymbol{v}_p^- + \boldsymbol{v}_p^- \times \boldsymbol{T} \tag{4.23}$$

$$\boldsymbol{v}_p^+ = \boldsymbol{v}_p^- + \boldsymbol{v}_p' \times \boldsymbol{S}, \tag{4.24}$$

where

$$\boldsymbol{T} = -\frac{\boldsymbol{B}^t}{|\boldsymbol{B}^t|}\tan\frac{\theta}{2} = \frac{q_p \boldsymbol{B}_p}{m_p \gamma_p c}\frac{\Delta t}{2} \tag{4.25}$$

$$\boldsymbol{S} = -\frac{2\boldsymbol{T}}{1 + |T|^2}. \tag{4.26}$$

From this, we can now summarize the three step Buneman-Boris algorithm for getting from $\boldsymbol{v}_p^{t-\Delta t/2}$ to $\boldsymbol{v}_p^{t-\Delta t/2}$ as

1. Half-step acceleration by electric field as Eq.4.19
2. Rotation motion by magnetic field as Eqs.4.23-4.24
3. Half-step acceleration by electric field as Eq.4.20

For position update, we simply solve Eq.4.17.

4.5 Field Solver

In PIC simulation scheme, electric and magnetic field are defined on the grid point, that means the Maxwell's equations (Eqs.4.2-4.5) are solved on the grid point. When we use leap-frog method, which is a second-order finite differencing scheme, the equations to solve are derived as:

$$\frac{\boldsymbol{B}^{t+\Delta t/2} - \boldsymbol{B}^{t-\Delta t/2}}{\Delta t} = -c\nabla \times \boldsymbol{E}^t \tag{4.27}$$

$$\frac{\boldsymbol{E}^{t+\Delta t} - \boldsymbol{E}^t}{\Delta t} = c\nabla \times \boldsymbol{B}^{t+\Delta t/2} - 4\pi \boldsymbol{j}^{t+\Delta t/2}, \tag{4.28}$$

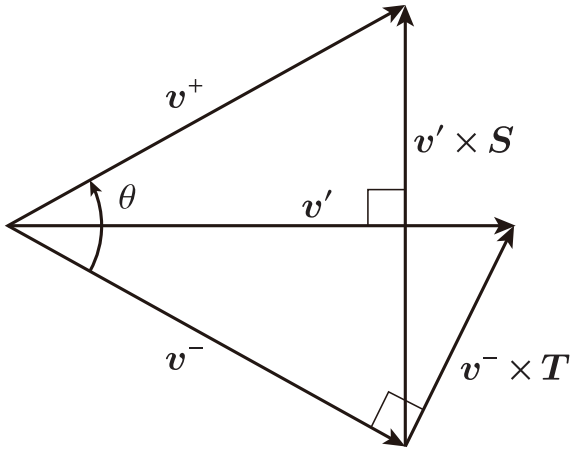

Figure 4.2: Schematic view of Buneman-Boris algorithm.

where, N is the total number of particles in the simulation. This scheme poses some problems, which we have to know how to calculate the current density $\boldsymbol{j}^{t+\Delta t/2}$.

The current density is calculated by using the position and velocities of the particles moving continuously within the domain. This is the key of a PIC code, which connects the particle motion component to the fields and allows us to calculate the fields on the grid self-consistently. For the current density, we take a summation of the particle velocities and charges weighted on the distance from the grid point as

$$\boldsymbol{j}_i^{t+\Delta t/2} = \sum_{p=1}^{N} q_p \frac{\boldsymbol{v}_p^{t+\Delta t/2}}{\gamma_p^{t+\Delta t/2}} S(\boldsymbol{x}_p^{t+\Delta t/2}), \tag{4.29}$$

where $\boldsymbol{j}_i^{t+\Delta t/2}$ is the current density at grid point i. The function S is a shape function which in this case decides what fraction of current density a particle contributes based on its position. This shape function is described in following section.

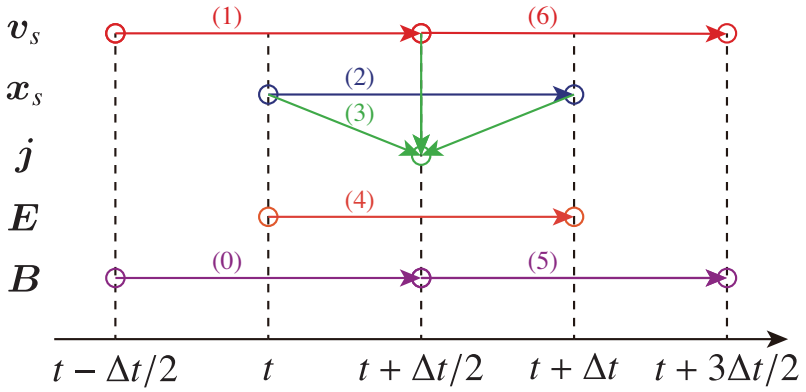

Figure 4.3: A schematic view of the time integration in PIC simulation code.

Fig.4.3 shows the summary for time integration of particles (session 4.4) and fields (session 4.5). It is important to note that we calculate $\boldsymbol{B}^t$ by averaging $\boldsymbol{B}^{t-\Delta t/2}$ and $\boldsymbol{B}^{t+\Delta t/2}$ to solve the equation of motion, Eq.4.16.

4.6 Finite Size Particle Method

As previously mentioned the fields are localized to discrete grid points whereas particles travel continuously in the simulation box. When we calculate the charge for a field, it is possible to simply assign particle charge to the nearest grid point. However, when a particle moves through the domain the point at which the charge is assigned changes and this will result in a discrete jump in charge density across grid points. This will make for a noisy solution due to small number of the super-particles but this can be reduced by weighting the particle charge between more neighbouring grid points; finite size particle method. In the PASMO code, we use a triangle shape for the shape function (called as Cloud-in-Cell (CIC) method). Figure 4.4 shows a concept of the shape function on one-dimensional grid. The width of the triangle shape function is $2\Delta x$, that has contribution to three grid points near the particle. Then, the shape function S is described as

$$S(x_s - X) = \begin{cases} 1 - \dfrac{|x_s - X|}{\Delta x} & (|x_s - X| \leq \Delta x) \\ 0 & (|x_s - X| > \Delta x) \end{cases} \tag{4.30}$$

where x_s is the position of the particle and X is a grid point.

When the particle is located between grid point X_i and X_{i+1} as shown in Fig.4.4, the contribution of the charge and velocity from the particle is calculated as the fraction of that

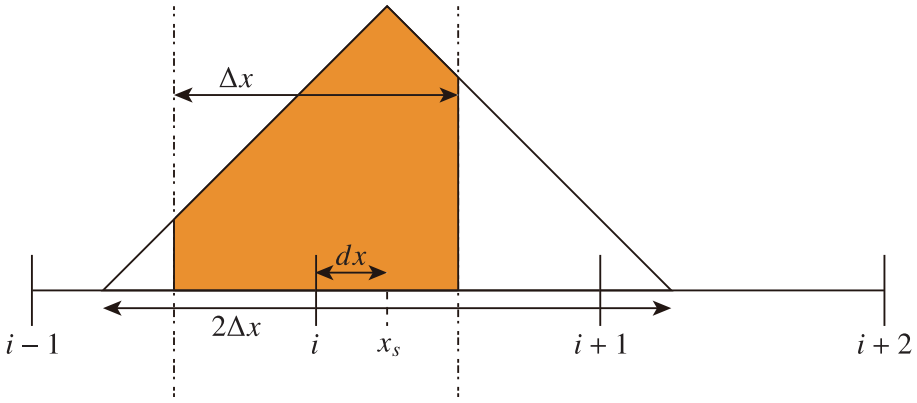

Figure 4.4: The shape function on the one-dimensional grid.

between $X_{i-\Delta/2}$ and $X_{i+\Delta/2}$, where is painted in the orange region in Fig.4.4. Therefore, the weight from the particle at the grid point X_i can be described as

$$S_i = \int_{X_{i-\Delta/2}}^{X_{i+\Delta/2}} S(x_s - X)dX. \tag{4.31}$$

In the PASMO code, we use $dx = x_s - X_i$ to calculate the weight S_i at the grid point instead of integrating over the space. The contribution to the three grid points X_{i-1}, X_i and X_{i+1} become

$$S_{i-1} = \frac{\Delta x}{2}\left(\frac{1}{2} - dx\right)^2, \tag{4.32}$$

$$S_i = \Delta x\left(\frac{3}{4} - dx^2\right), \tag{4.33}$$

$$S_{i+1} = \frac{\Delta x}{2}\left(\frac{1}{2} + dx\right)^2. \tag{4.34}$$

This weight can be applied into multi-dimensional by multiplication in the number of dimensions. For example, the simulation for this work is done by two-dimensional, the weight at a grid point $X_{i,j}$ can be described as

$$S_{i,j}(\boldsymbol{x}_s) = S_i(x_s)S_j(x_s). \tag{4.35}$$

On the other hand, the fields acting on the particle are interpolated back in exactly the same way. For instance to calculate the electric field acting on particle x_s is describes as

$$\boldsymbol{E}(\boldsymbol{x}_s) = \sum_{i,j} \boldsymbol{E}_{i,j} S(i,j). \tag{4.36}$$

4.7 Boundary Condition

All of the reconnection simulations in this work are performed in 2.5D. Vector quantities in the third dimension are allowed to exist. However, there is no variation along the third (z) dimension. The simulation domain is a rectangular box of size $L_x \times L_y$, with $L_x = 1536\lambda_D$ and $L_x = 384\lambda_D$. Figure 4.5 shows the simulation box in 2D PASMO code. In order to understand the energy conversion mechanism of magnetic reconnection and mimic the laboratory reconnection experiment, we used a free condition is used at the downstream boundary and an input driven condition is used at the upstream boundary. In the upstream region, the ideal magnetohydrodynamics (MHD) condition for the plasma,

that hat the frozen-in condition is satisfied for both ions and electrons, can be assumed:

$$\boldsymbol{E} + \boldsymbol{u} \times \boldsymbol{B} = 0. \tag{4.37}$$

Then the plasma is smoothly supplied with the $\boldsymbol{E} \times \boldsymbol{B}$ drift velocity into the simulation domain:

$$\boldsymbol{u}_{in} = \frac{\boldsymbol{E}_{in} \times \boldsymbol{B}_{in}}{B_{in}^2}. \tag{4.38}$$

The plasma inflows are symmetrically driven from two upstream boundaries by the external electric field imposed in perpendicular to the magnetic field. The amplitude of driving field $E_{d,z}(x,t)$ is initialized to zero at $t = 0$, and increases with time while keeping a bell-shaped profile near the center and a flat profile in the periphery for an initial short time. This driving field $E_{d,z}(x,t)$ is controlled by two parameters: maximum flux input rate E_0 and the spatial size of initial bell-shaped profile x_d (input window size). The distribution function of incoming particles at the input boundary is assumed to be a shifted Maxwellian with a constant temperature and the average velocity equal to the $\boldsymbol{E} \times \boldsymbol{B}$ drift velocity.

We adopt an open boundary condition in the PASMO code, where electric and magnetic fields freely expand from the downstream region and plasmas never re-enter the diffusion region after they pass through the reconnection region. Plasmas encounter energy conversion events only once in contrast to the periodic system, in which the plasma gains energy through reconnection many times (periodically). Furthermore, under the open boundary condition, we can obtain quasi-steady state, where initial Harris-type sheet is exhausted and the reconnection electric field is spatially uniform and temporally constant.

Field quantities E_x, E_y and $\partial E_z/\partial x$ are assumed to be continuous at the downstream

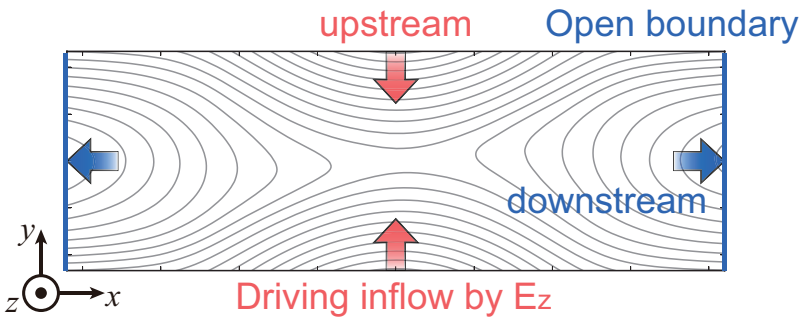

Figure 4.5: Simulation box in 2D PASMO code. The free condition is used at the downstream boundary and an input driven condition is used at the upstream boundary.

boundary. Magnetic field at the boundaries is directly given by solving Maxwell equations there.

In PASMO code, the model for the open boundary condition for particles is different from most codes [74]. When the positions of particles are updated by the particle solver, the particles in the X-boundary (downstream) cell and outside the simulation box are removed. To realize the assumption that the physical quantity outside is the same as that in the boundary region, we make the same particle distribution function in the X boundary cell as in the n-th region, which is the $(n-1)$-th neighbor of the X-boundary cell. The positions and velocities of particles in the X-boundary cell are defined using the information for particles in the n-th region. In other words, all of the particles in the X-boundary cell are replaced by those in the n-th region. When the number of electrons and ions are different in the X-boundary cell, those are loaded in the X boundary cell is adjusted to satisfy charge neutrality in the entire system. In this model, the variation of particle quantities along the x direction nearly vanishes at the boundary. Accordingly, the zero normal condition is realized there.

4.8 Initial Conditions and Normalization

As an initial condition, we adopt a one-dimensional equilibrium with the Harris-type antiparallel magnetic configuration [20] as

$$B_x(y) = B_0 \tanh(y/L), \tag{4.39}$$

$$B_z(y) = B_{z,0}, \tag{4.40}$$

$$P(y) = \frac{B_0^2}{8\pi} \operatorname{sech}^2(y/L) + P_0, \tag{4.41}$$

where reconnecting magnetic field B_0, initial guide-field $B_{z,0}$, plasma pressure of background particles $P_0 = 0.35(B_0^2/8\pi)$ are constants and L is a scale height along the y-axis. There is a magnetically neutral sheet along the mid-horizontal line ($y = 0$) in the initial equilibrium. The initial particle velocity distribution is assumed to be a shifted Maxwellian with spatially constant temperature and average particle velocity equal to the diamagnetic drift velocity. Thus, the particle distribution function can be described as

$$f_s(y) = n_0 \operatorname{sech}^2(y/L) \left(\frac{m_s}{2\pi T_s}\right)^{3/2} \exp\left[-\frac{m_s(v_{s,x}^2 + v_{s,y}^2 + (v_{s,z} - u_s)^2)}{2T_s}\right]. \tag{4.42}$$

The initial condition satisfies the kinetic equilibrium under the following condition:

$$-\frac{u_i}{u_e} = \frac{T_i}{T_e}, \qquad L = \frac{2(T_i + T_e}{B_0|u_i - u_e|}. \tag{4.43}$$

As a result, it is satisfied the pressure balance and Ampere's law:

$$n_0(T_i + T_e) = \frac{B_0^2}{8\pi}, \tag{4.44}$$

$$en_0(u_i - u_e) = \frac{B_0}{4\pi L}. \tag{4.45}$$

Because both the ions and the electrons are loaded at the same spatial position, there is no electric field in the initial profile.

The normalization for the variable physical values in the simulation is following:

$$m = \hat{m} m_e, \tag{4.46}$$

$$q = \hat{q} e, \tag{4.47}$$

$$t = \hat{t}/\omega_{ce}, \tag{4.48}$$

$$v = \hat{v}/c, \tag{4.49}$$

$$x = \hat{x}\,(c/\omega_{ce,x})\,, \tag{4.50}$$

$$E = \hat{E}\left(\frac{m_e c \omega_{ce,x}}{e}\right), \tag{4.51}$$

$$B = \hat{B}\left(\frac{m_e c \omega_{ce,x}}{e}\right), \tag{4.52}$$

where q is the charge, e is the elementary charge, m_e is the electron's rest mass, ω_{ce} is the electron cyclotron frequency, c is the light speed and $\omega_{ce,x} = eB_0/m_e$ is the electron cyclotron frequency defined by only reconnecting component of magnetic field at the upstream.

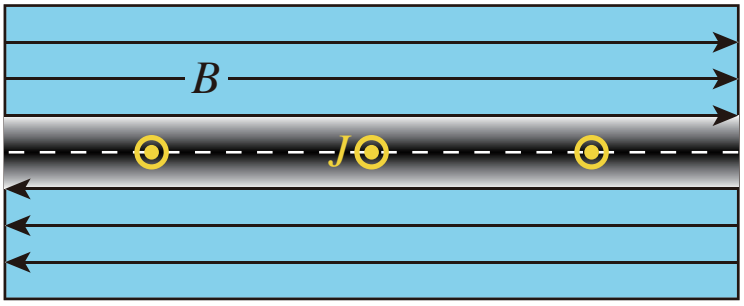

Figure 4.6: A schematic view of one-dimensional Harris-type equilibrium condition.

4.9 Magnetic Coordinate System

In this work, we use magnetic coordinate system instead of the Cartesian coordinate system to analyze the output data from the simulation and understand the physics associated with the particle motion. The transformation of coordinate system is performed as

$$\hat{e_{\perp 2}} = \hat{B}_p \times \hat{e}_z, \tag{4.53}$$

$$\hat{e_{\parallel}} = \hat{B}, \tag{4.54}$$

$$\hat{e_{\perp 1}} = \hat{e_{\perp 2}} \times \hat{e}_{\parallel}, \tag{4.55}$$

where $\hat{B_p} = \boldsymbol{B}_p/|B_p|$ is poloidal magnetic field normalized by the strength of the poloidal magnetic field and $\hat{e}_z$ is the unit vector along z-axis. Figure 4.7 shows the concept of the coordinate transformation, which is based on two rotation operations: (1) a rotation with angle ϕ in x-y plane and (2) a rotation with angle θ. The operations (1) and (2) can be described as

$$\begin{pmatrix} \hat{e'_{\perp 1}} \\ \hat{e'_{\perp 2}} \\ \hat{e'_{\parallel}} \end{pmatrix} = \begin{pmatrix} 0 & 0 & 1 \\ \sin\phi & -\cos\phi & 0 \\ \cos\phi & \sin\phi & 0 \end{pmatrix} \begin{pmatrix} \hat{e_x} \\ \hat{e_y} \\ \hat{e_z} \end{pmatrix}, \tag{4.56}$$

$$\begin{pmatrix} \hat{e_{\perp 1}} \\ \hat{e_{\perp 2}} \\ \hat{e_{\parallel}} \end{pmatrix} = \begin{pmatrix} \sin\theta & 0 & -cos\theta \\ 0 & 1 & 0 \\ \cos\theta & 0 & \sin\theta \end{pmatrix} \begin{pmatrix} \hat{e'_{\perp 1}} \\ \hat{e'_{\perp 2}} \\ \hat{e'_{\parallel}} \end{pmatrix}. \tag{4.57}$$

In summary, the operation of coordinate transformation can be described as

$$\begin{pmatrix} \hat{e_{\perp 1}} \\ \hat{e_{\perp 2}} \\ \hat{e_{\parallel}} \end{pmatrix} = \begin{pmatrix} -\cos\phi\cos\theta & -\sin\phi\cos\theta & \sin\theta \\ \sin\phi & -\cos\phi & 0 \\ \cos\phi\sin\theta & \sin\phi\sin\theta & \cos\theta \end{pmatrix} \begin{pmatrix} \hat{e_x} \\ \hat{e_y} \\ \hat{e_z} \end{pmatrix}. \tag{4.58}$$

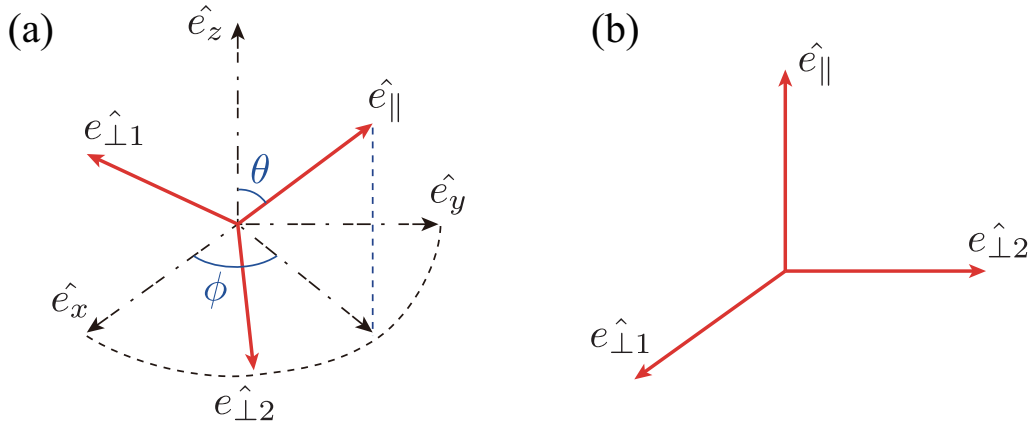

Figure 4.7: The concept of the coordinate transformation from the Cartesian coordinate to the magnetic coordinate system.

Chapter 5

Simulation Results

In this chapter, the results from 2D PASMO simulation of guide-field reconnection is discussed. First, the quasi-steady state of the reconnection when we performed data analysis is reported. Then, The electric field structure, which plays a key role in the electron energization, is presented. Finally, the observed parallel and perpendicular acceleration and heating are discussed.

5.1 Quasi Steady-State of Reconnection

As time goes on, the reconnection process gradually relaxes toward a steady state. Figure 5.1 (a) shows the temporal evolutions of the reconnection electric field E_z for the case guide-field ratio is 3, where the thin dotted lines stand for the values of the external driving electric field E_d=0.04.

The reconnection electric field is defined as the out-of-plane electric field at the X-point, that is a direct measure of the reconnection rate. There exist two temporal phases in the evolution of the reconnection electric field, i.e., the growing phase and saturation phase. The reconnection field experiences a fast growth, starts to saturate and then gradually approaches the external driving field. These results lead us to the conclusion that the system transits to a steady reconnection state in which the reconnection rate is balanced with the flux input rate at the boundary. This conclusion is consistent with the requirement for a steady state.

The steady reconnection rate is mainly controlled by the external driving electric field E_d, which is consistent with the requirement for a 2D steady state, though there is a small fluctuation around E_d. Furthermore, for 2D quasi-steady reconnection, the out-of-

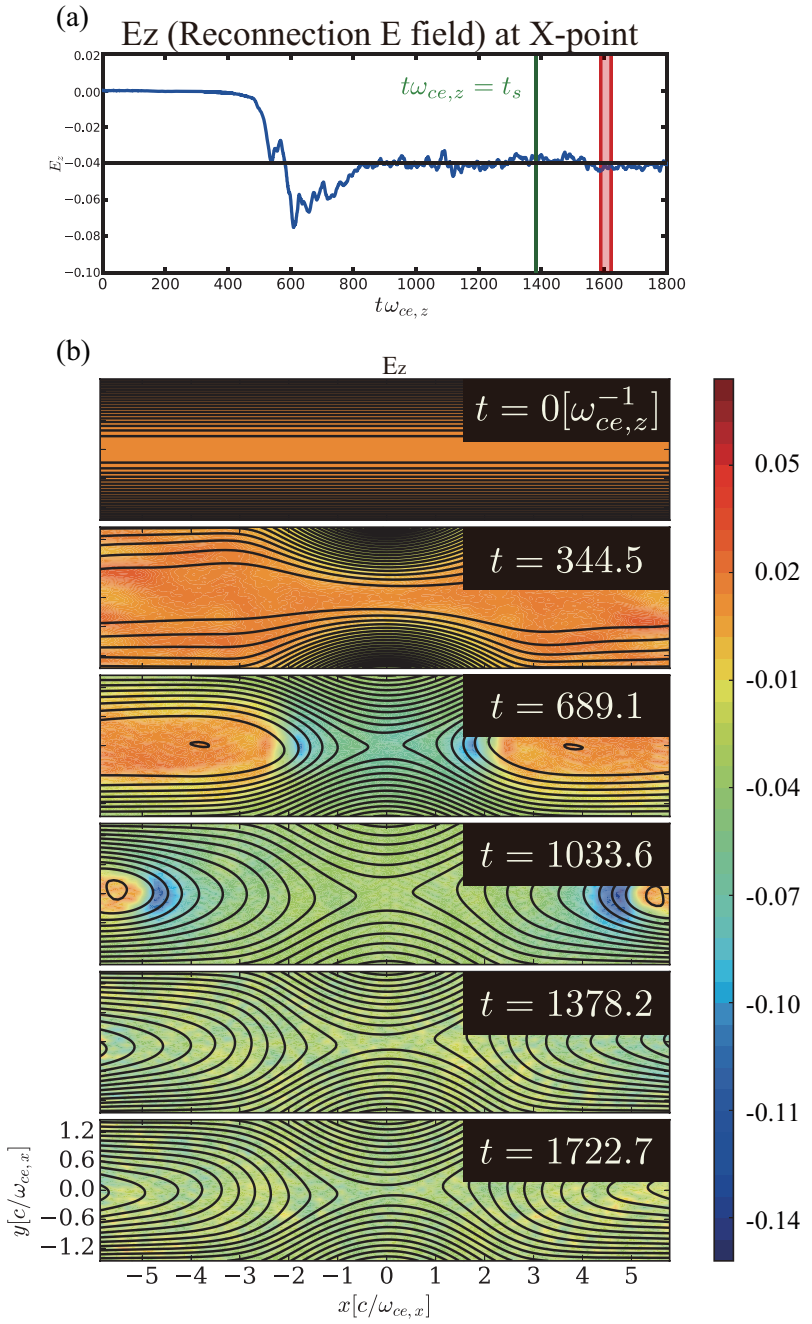

Figure 5.1: (a) The time evolution of out-of-plane electric field at the X-point. The out-of-plane electric field E_z becomes uniform in space after $t\omega_{ce,z} = t_s \simeq 1400$. (b) The time evolution of out-of-plane electric field E_z in 2D. It penetrates toward the center of the simulation box from the upstream boundaries and becomes uniform in space after the quasi-steady state.

plane electric field becomes uniform in space, and therefore this field must be equal to the external driving field E_d at the boundary, which is verified from Faraday's law, as shown in Fig.5.1 (b).

Since the physical quantities are almost kept unchanged in the quasi steady-state, we averaged the simulation data over time during $t\omega_{ce,z} = 1596.37\text{-}1619.34$ (red region in Fig. 5.1(a)), which is comparable to 3.66 electron gyration periods in order to decrease statistical noise. The following data analysis is performed by using the averaged data.

5.2 Electric Field Structure

5.2.1 Parallel Electric Field

One of the signature of the guide-field reconnection is the parallel electric field structure along the low density separatrix arm [42; 43]. Since the guide-field component of the magnetic field and the reconnection electric field is in the same axis, there is a parallel electric field component to the magnetic field at the X-point. When the reconnection

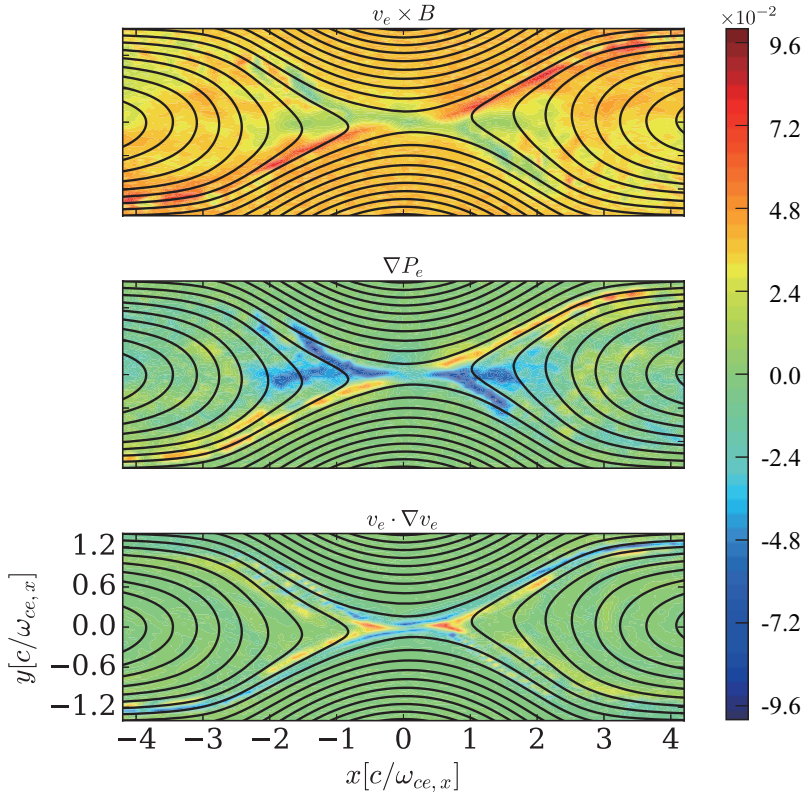

Figure 5.2: 2D spatial profiles of the Lorentz force, pressure and inertia terms in out-of-plane component of the generalized Ohm's law.

relaxes to a quasi steady-state, the generalized Ohm's law is written as

$$\boldsymbol{E} + \boldsymbol{v}_e \times \boldsymbol{B} = -\frac{1}{qn_e}\nabla \cdot \boldsymbol{P}_e - \frac{m_e}{q}\left(\frac{\partial}{\partial t} + \boldsymbol{v}_e \cdot \nabla\right)\boldsymbol{v}_e. \tag{5.1}$$

Figure 5.2 shows the 2D spatial profiles of the out-of-plane z-components of ideal and non-ideal terms in Eq.5.1. The frozen-in condition for electrons is broken by both the pressure term and the inertia term near the X-point. Since the dot product of the Lorentz term in Eq.5.1 and the magnetic field, $(\boldsymbol{v}_e \times \boldsymbol{B}) \cdot \boldsymbol{B} = 0$, the parallel electric field $E_\parallel = \boldsymbol{E} \cdot \hat{\boldsymbol{B}}$ is sustained by these pressure and inertia terms of the generalized Ohm's law. In the high guide-field condition, the magnetic field line is mainly in z-direction, it is found that the pressure term shown in Fig.5.2 (b) plays a key role in the generation of the parallel electric field.

When the inflows from the upstream boundaries are driven by the external electric field E_z, the electrons can be accelerated parallel to the magnetic field since there is guide-field in the same direction. Meanwhile, ions cannot follow the electron dynamics due to the mass ratio, there is ion rich region near the X-point. In order to maintain the charge neutrality, electrons are coming from the upstream, however, they would be accelerated by the electric field along the separatrix. As a result, quadruple structure of the electron density is achieved. It breaks the symmetry of the electric field structure and

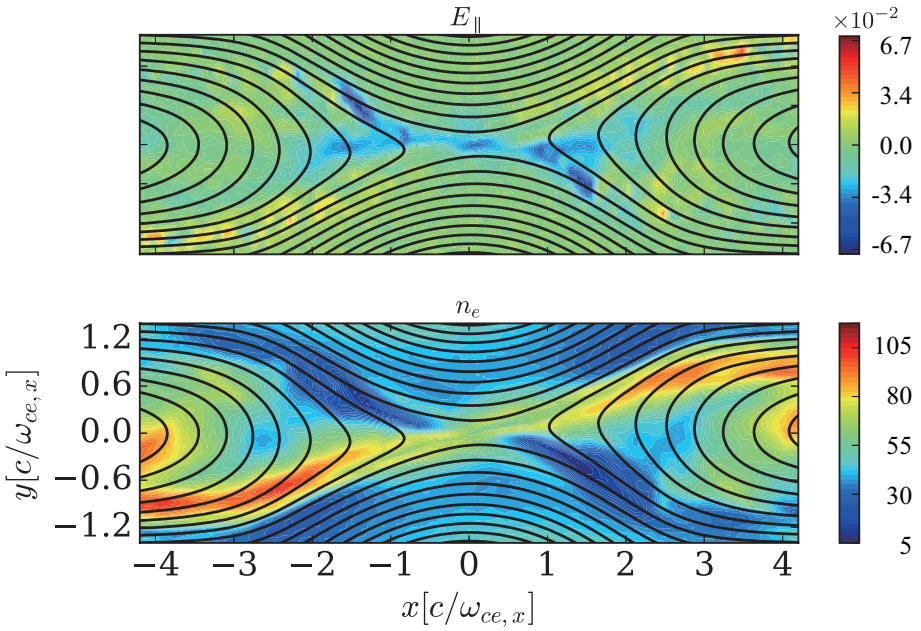

Figure 5.3: 2D spatial profiles of the parallel electric field and electron density profile.

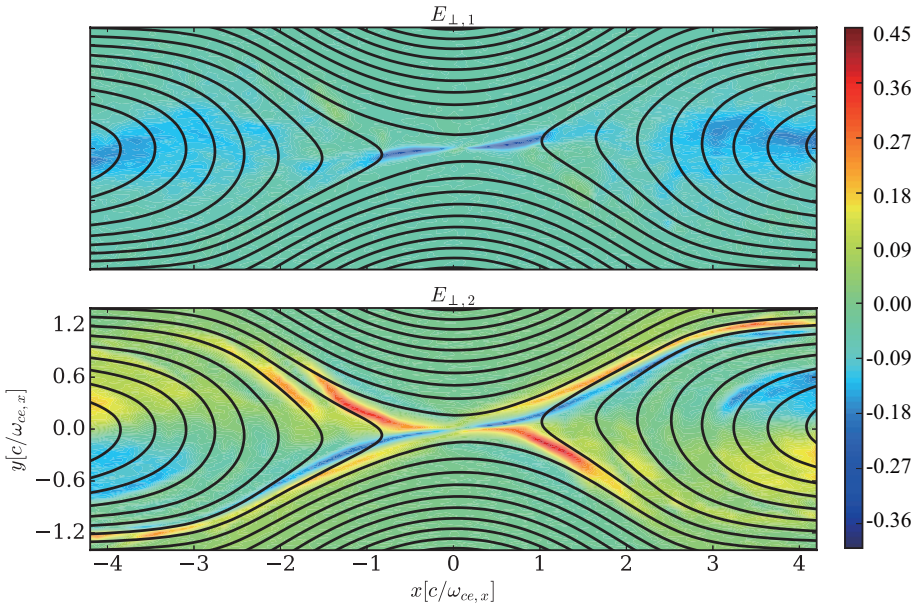

Figure 5.4: 2D spatial profiles of the perpendicular electric fields, which are mainly electrostatic fields generated by the charge separation.

the pressure profile would play a role to generate the parallel electric field along the low density separatrix arm as shown as Fig.5.3.

5.2.2 Perpendicular Electric Field

Figure 5.4 shows the perpendicular electric fields $E_{\perp,1}$ and $E_{\perp,2}$ in the high guide-field reconnection, where the magnetic coordinate system is discussed in the previous chapter. It is found that $E_{\perp,1}$ is localized in the vicinity of the X-point on the mid-plane ($y = 0$) and $E_{\perp,2}$ is peaked along the magnetic field line in the separatrices.

The perpendicular electric fields, unlike the parallel electric field, are mainly electrostatic fields, which is generated by the charge separation. The out-of-plane magnetic field in the high guide-field condition consists of a symmetric guide-field and quadrupole field created by the Hall current, as a result, the magnetic pressure decreases in the region where the sign of the quadrupole field is opposite to that of the guide-field, while in the other region, the magnetic pressure increases. The external driving plasma flow strongly compresses the weak magnetic pressure region, and thus the asymmetric profile of the out-of-plane magnetic field is formed. Strong compression creates an electron-rich region in the region of the weak magnetic field near the high density separatrix, where the electron current layer evolves. as shown in Fig.5.5.

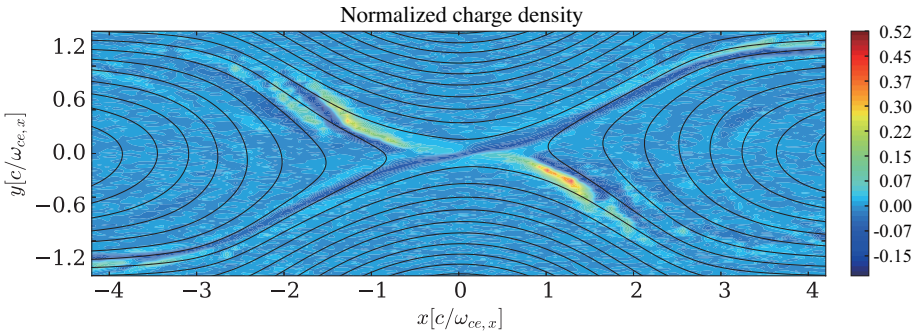

Figure 5.5: 2D spatial profiles of the normalized charge density $(n_i - n_e)/n_e$.

5.2.3 Charge separation

Although the pressure gradient force balances the Lorentz force in the Harris equilibrium, the electrostatic force balances the Lorentz force in the y direction as

$$n_e e E_y = \frac{1}{c}\left(J_{ez}B_x - J_{ex}B_z\right). \tag{5.2}$$

This equation is equivalent to the electron frozen-in condition in the inflow direction. The electrostatic field is maximized around the electron skin depth and its value is much larger than the pressure tensor term. By using Ampere's law and the fact that the current density is carried mainly by electrons, the force-balance equation Eq.5.2 is rewritten as

$$n_e e E_y = -\frac{\partial}{\partial y}\left(\frac{B_x^2 + B_z^2}{8\pi}\right) + \frac{1}{4\pi}\left(B_x\frac{\partial B_y}{\partial x} + B_z\frac{\partial B_x}{\partial z}\right). \tag{5.3}$$

This equation suggests that the electrostatic force balances the magnetic pressure force which is a main component of the Lorentz force. The inward flowing magnetized electrons carry magnetic flux towards the electron dissipation region away from the ion dissipation region. If the half-width of charge separation region (CSR) is given by the electron skin depth d_e, using Gauss' law, Eq.5.2 can be rewritten as

$$\begin{aligned}
\frac{4\pi n_e e^2}{m_e c^2} d_e (n_i - n_e) &= \frac{-1}{4\pi m_e c^2}\left[\frac{\partial}{\partial y}\left(\frac{B_x^2 + B_z^2}{2}\right) - B_x\left(\frac{\partial B_y}{\partial x}\right)\right], \\
\frac{1}{d_e}\int\left(\frac{n_i - n_e}{n_e}\right)dy &= -\frac{1}{2}\left(\frac{V_{e,Alf,t}}{c}\right)^2 + \frac{1}{4\pi n_e m_e c^2}\int B_x\frac{\partial B_y}{\partial x}dy, \\
&= -\frac{1}{2}\left(\frac{V_{e,Alf,t}}{c}\right)^2 + \mathcal{R}\sqrt{\frac{m_e}{m_i}}\left(\frac{V_{e,Alf,x}}{c}\right)^2.
\end{aligned} \tag{5.4}$$

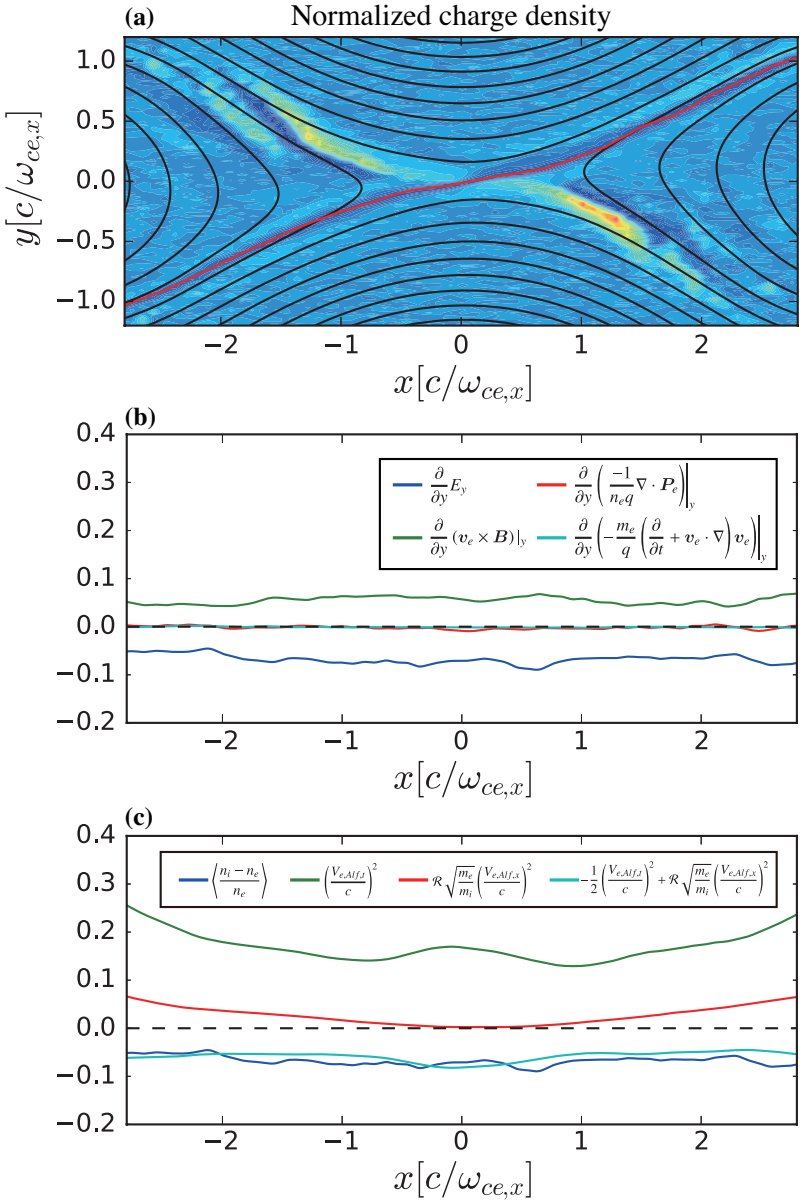

Figure 5.6: (a) 2D spatial profiles of the normalized charge density $\hat{n_c} = (n_i - n_e)/n_e$ with the red line, which presents the peak value of the normalized charge density. 1D profiles of (b) the partial differential of the each term in the generalized Ohm's law in the inflow direction and (c) the relation between the electron Alfvén velocity at the edge of CSR and normalized charge density according Eq.5.5 along the red line in the above panel (a).

As a result, a relation between the electron Alfvén velocity at the edge of CSR and normalized charge density inside CSR can be obtained as

$$\left\langle \frac{n_i - n_e}{n_e} \right\rangle = -\frac{1}{2}\left(\frac{V_{e,Alf,t}}{c}\right)^2 + \mathcal{R}\sqrt{\frac{m_e}{m_i}}\left(\frac{V_{e,Alf,x}}{c}\right)^2. \tag{5.5}$$

Here,

$$V_{e,Alf,t} = \sqrt{\frac{B_x^2 + B_z^2}{4\pi n_e m_e}}, \quad V_{e,Alf,x} = \frac{B_x}{\sqrt{4\pi n_e m_e}} \text{ and } \mathcal{R} = \frac{E_z}{B_{x,0} V_{i,Alf,x}}. \tag{5.6}$$

Figure 5.6 (b) shows the contribution from the partial differential of the each term in the generalized Ohm's law in the inflow direction along a red line shown in Fig.5.6 (a), where the normalized charge density has peak value. It is obviously found the Lorentz force is the main component for the force balance in the inflow direction and that is almost constant along the high density separatrix where the normalized charge separation is peaked. Figure 5.6 (c) shows the contribution from each term in the Eq.5.5 along the red line shown in Fig.5.6 (a). It is clearly seen that the normalized charge density is about 0.06, which satisfies Eq.5.5 with high accuracy. The detail physics about the reason why the normalized charge density has a constant value along the high density separatrix needs future discussion.

5.3 Energy Conversion Mechanism for Electrons

5.3.1 Overview of Electron Energy Conversion Mechanism

The energy conversion mechanism for electron energy, both the thermal and the kinetic energy, is investigated by means of two-dimensional, full-particle simulations in an open system. The parallel electric field is generated in the low density separatrix and that accelerates electrons along the separatix, as a result, electrons from a beam component of the distribution function. When the accelerated electrons escape from the X-point and meet the cold bulk component, the thermal energy can be pile-up in there. It is also shown that electron perpendicular heating is mainly due to the breaking of magnetic moment conservation in separatrix region because the charge separation generates intense variation of electric field within the several electron Larmor radii. Meanwhile, electron perpendicular acceleration takes place manly due to the polarization drift term as well as the curvature

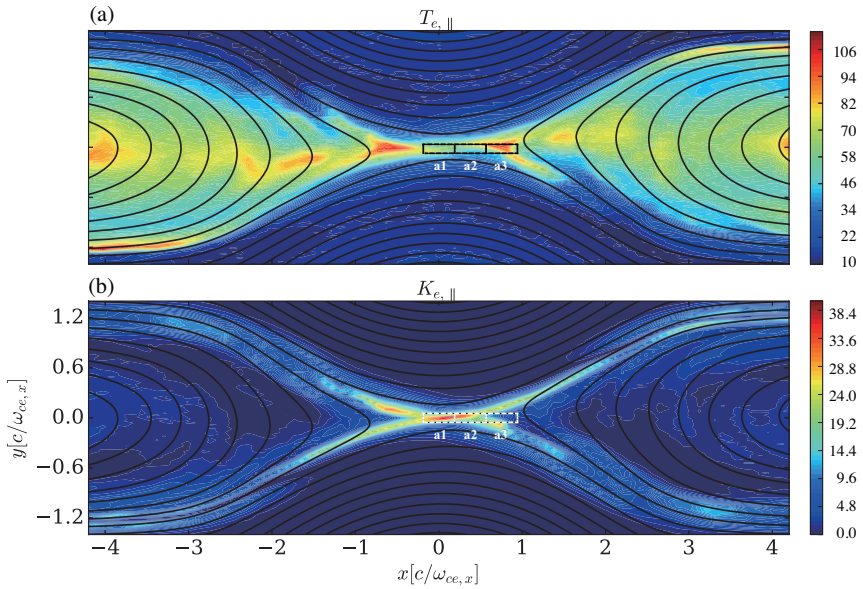

Figure 5.7: 2D profiles of (a) the perpendicular electron thermal energy $T_{e,\parallel}$ and (b) the perpendicular electron kinetic energy $K_{e,\parallel}$ per a single electron in the quasi-steady state. The physical quantities are averaged over time during $t\omega_{ce,z} = 1596.37$–1619.34, which is comparable to 3.66 electron gyration periods.

drift term of $\boldsymbol{E} \cdot \boldsymbol{u}_\perp$ in the downstream near the X-point. The enhanced electric field due to the charge separation there results in a significant effect of the polarization drift term on the dissipation of magnetic energy within the ion inertia length in the downstream.

5.3.2 Parallel Acceleration and Heating

Figure 5.7 shows the thermal component of electric parallel energy $T_{e,\parallel} = \boldsymbol{P}_e \cdot \hat{\boldsymbol{B}}^2/n_e$ and $K_{e,\parallel} = 0.5 m_e \left(\boldsymbol{u}_e \cdot \hat{\boldsymbol{B}}\right)^2$, where $\boldsymbol{P}_e$ is the diagonal term of electron pressure tensor, $\hat{\boldsymbol{B}} = \boldsymbol{B}/|B|$ is the normalized magnetic field and n_e is electron density. It is clearly shown that electrons are accelerated by the parallel electric field along the separatrix and they gain kinetic energy in the vicinity of the X-point. Since the collision effect is not installed in this 2D simulation, the accelerated electrons from a beam component in the distribution function in the vicinity of the X-point. It explains that the thermal component is not peaked at the X-point.

Figure 5.8 shows the electron distribution function sampled in the boxed area illustrated in Fig.5.7 in the vicinity of the X-point. It is found the parallel beam component of electron distribution function at the X-point. This beam component, which is also found in previous researches [35; 42; 43; 75] can drive beam type instability that we do not discuss

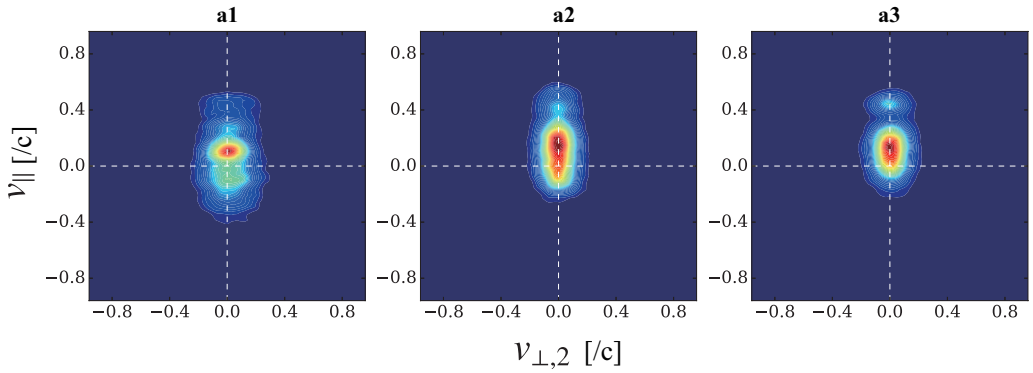

Figure 5.8: The electron distribution $f_e(v_{\perp,1}, v_{\perp,2}, v_{\parallel})$ sampled in the boxed area illustrated in Fig.5.7 in the vicinity of the X-point.

in this dissertation. The electron parallel acceleration is often observed by the satellites' measurements in the magnetotail [66; 76].

5.3.3 Perpendicular Acceleration and Heating

Figure 5.9(a) shows the thermal component of electron perpendicular energy $T_{e,\perp} = \boldsymbol{P}_e \cdot (\boldsymbol{I} - \hat{\boldsymbol{B}}^2)/2n_e$, where $\boldsymbol{P}_e$ is the diagonal term of electron pressure tensor, $\boldsymbol{I}$ is a unit matrix, $\hat{\boldsymbol{B}} = \boldsymbol{B}/|B|$ is the normalized magnetic field and n_e is electron density. It is shown that $T_{e,\perp}$ increases in one pair of separatrix arms (region (i)) and little region of the other pair of separatrix arms (region (ii)) during high guide-field reconnection. Since the out-plane magnetic field B_z is almost spatially uniform in the vicinity of the central diffusion region, including the X-point and separatrix region near the X-point [35], the intensity of magnetic field only has a 20% difference between the X-point and the separatrix region. That is, the mirror effect is not effective during the high guide-field reconnection. Therefore, the magnetic moment conservation of electrons is obviously broken in the separatrix region.

Figure 5.10 (a) and (b) show charge separation and parallel electric field structure in the right half region. In the guide-field reconnection, the parallel electric field is generated in a pair of separatrix arms, which indicates the violation of the frozen-in condition for electrons ($\boldsymbol{E} + \boldsymbol{v}_e \times \boldsymbol{B} \neq 0$), as clarified in several papers [36; 42; 43; 44]. The electrons, which are easily accelerated by the parallel electric field, accumulate in both the region (i) and (ii). Because the ions cannot move as quickly as the electrons, accumulated electrons are charging negatively the region (i) and (ii) as shown in Fig.5.10 (a). Due to the presence

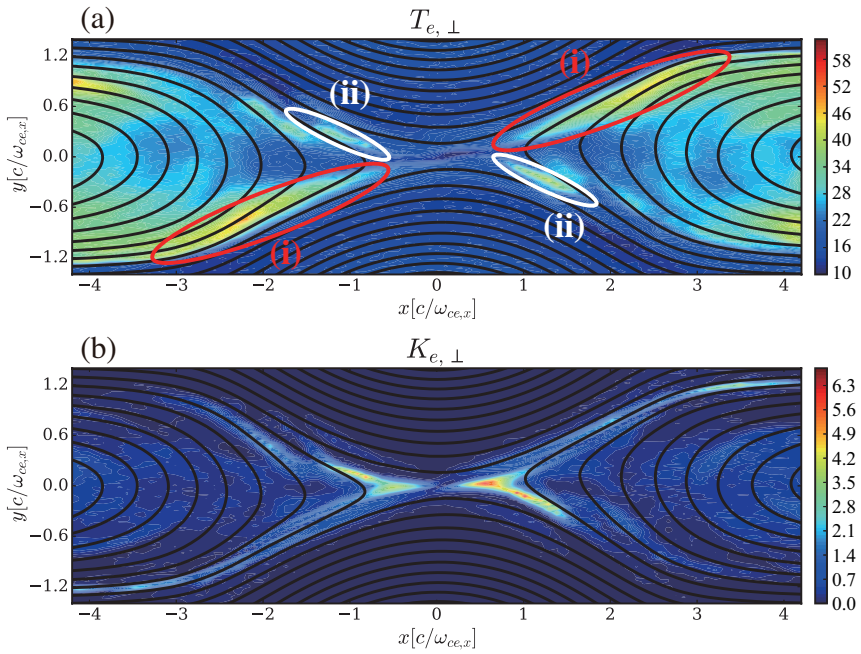

Figure 5.9: 2D profiles of (a) the perpendicular electron thermal energy $T_{e,\perp}$ and (b) the perpendicular electron kinetic energy $K_{e,\perp}$ per a single electron in the quasi-steady state. The physical quantities are averaged over time during $t\omega_{ce,z} = 1596.37$–1619.34, which is comparable to 3.66 electron gyration periods.

of charge separation, intense variation of electric fields is present with electron scale in both the region (i) and (ii) as shown in Fig.5.10 (c). In general, the fast electron motion plays a role to neutralize the charge separation quickly in plasma, however, the non-ideal effects sustain the electrostatic field, which is generated by the charge separation in the separatrix region as shown in Fig.5.10 (d). The width of the charge separation δ_d can be estimated from the electron dynamics as

$$\delta_d = V_d\sqrt{\frac{2Lm_e}{qE_\parallel}} \sim \frac{E}{B}\sqrt{\frac{2Lm_e}{qE_\parallel}} \sim r_e\sqrt{\frac{2V_d}{v_{th,e}}\frac{L}{r_e}}, \tag{5.7}$$

where V_d is $\boldsymbol{E}\times\boldsymbol{B}$ drift velocity, L is length of the parallel electric field along the field line and r_e is the electron Larmor radius. Since the parallel electric field is balanced with the pressure term and the inertia term, L is comparable to the ion inertia length d_{i0}. The width of the charge separation δ_d can be estimated under the assumption $L \sim d_{i0}$ as

$$\delta_d \sim r_e\sqrt{\frac{2V_d}{v_{th,e}}\frac{d_{i0}}{r_e}} = r_e\sqrt{\frac{2V_d}{v_{th,e}}\frac{c}{v_{th,e}}\frac{\omega_{ce}}{\omega_{pe}}\sqrt{\frac{m_i}{m_e}}}. \tag{5.8}$$

Using typical values for these parameters at sites of reconnection [54; 77; 78], δ_d is esti-

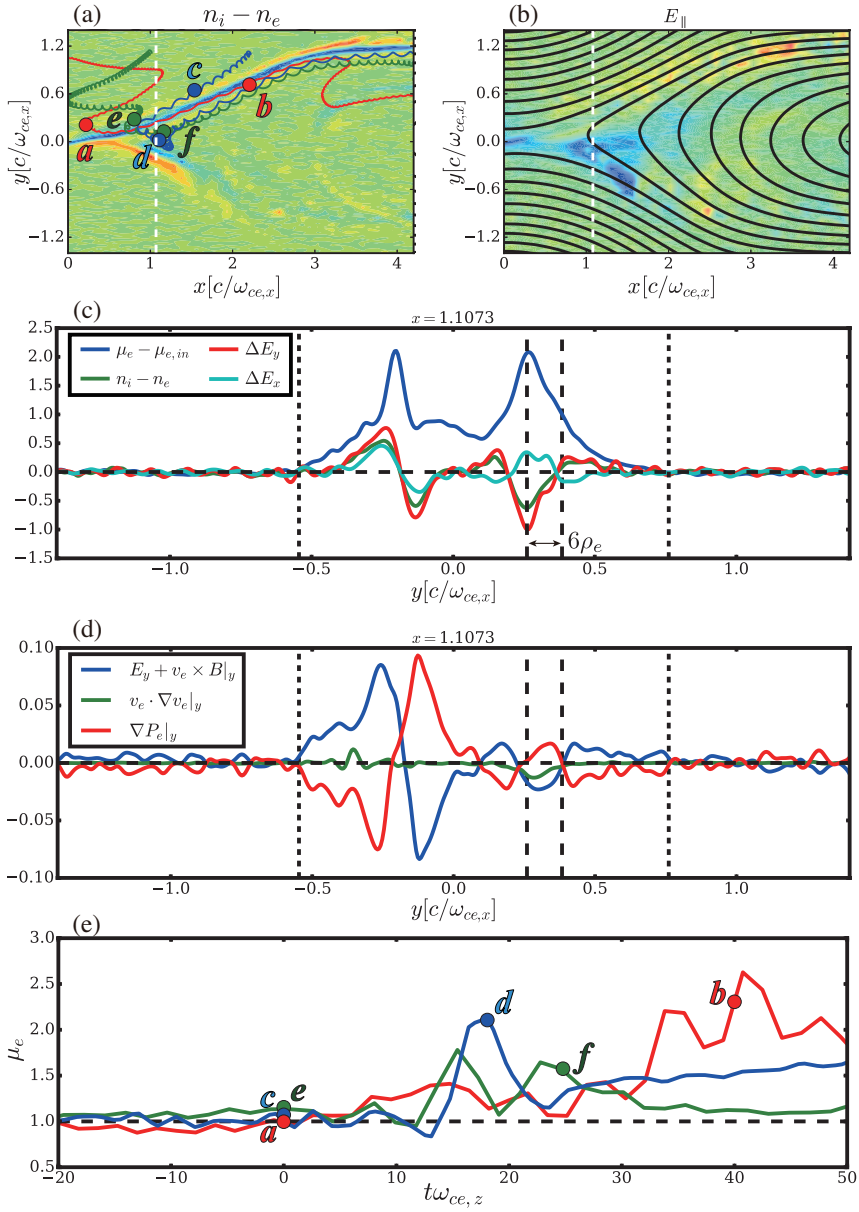

Figure 5.10: 2D profiles of (a) charge separation $n_i - n_e$ with the trajectory of test particles, wherein red and blue region means ion and electron rich respectively and (b) parallel electric field $E_\parallel$ in the quasi-steady state. (c) 1D profiles of the charge separation $n_i - n_e$, the variation of magnetic moment from that in the upstream $\mu_e - \mu_{e,in}$, the partial differential of electric field normalized to peak value of ΔE_y, where $\Delta E_x = \partial E_x/\partial y$ and $\Delta E_y = \partial E_y/\partial y$ along the illustrated cut, $x = 1.11c/\omega_{ce}$. (d) The spatial profile of each term in the in-plane component (y-direction) of the electron momentum equation along $x = 1.11c/\omega_{ce}$. (e) The time evolution of magnetic moment of the test particles.

mated as several electron Larmor radii. Therefore, the variation of electric fields, which caused by the charge separation, breaks the conservation of magnetic moment μ_e and increases the electron perpendicular temperature $T_{e,\perp}$ as shown in Fig.5.10 (c). The trajectories of the typical electrons are provided in Fig.5.10 (a) by means of the test particle simulation. When the electrons move across the separatrix, the electron magnetic moment μ_e increases due to the structure of electric fields as shown in Fig.5.10 (e).

On the other hand, the electron perpendicular kinetic energy $K_{e,\perp} = 0.5 m_e \boldsymbol{u}_e^2 \cdot (\boldsymbol{I} - \hat{\boldsymbol{B}}^2)$ due to the various drifts increases in the downstream near the X-point as shown in Fig.5.9 (b). Here, $\boldsymbol{u}_e \equiv \langle \boldsymbol{v}_e \rangle_{\boldsymbol{v}}$ is the electron fluid velocity and the operator $\langle \boldsymbol{a} \rangle_{\boldsymbol{v}} = 1/n_e \int d\boldsymbol{v} \boldsymbol{a} f_e(\boldsymbol{x}, \boldsymbol{v}, t)$ indicates the integration over velocity space. The electron current density perpendicular to magnetic field can be expressed as

$$
\begin{aligned}
n_e \boldsymbol{u}_\perp = & \boldsymbol{P}_\parallel \frac{\boldsymbol{B} \times (\boldsymbol{B} \cdot \nabla) \boldsymbol{B}}{B^4} \\
& + \boldsymbol{P}_\perp \left(\frac{\boldsymbol{B}}{B^3} \right) \times \nabla \boldsymbol{B} - \left[\nabla \times \frac{\boldsymbol{P}_\perp \boldsymbol{B}}{B^2} \right]_\perp \\
& + \rho \frac{\boldsymbol{E} \times \boldsymbol{B}}{B^2} + \rho_m \frac{\boldsymbol{B}}{B^2} \times \frac{d \boldsymbol{u}_E}{dt},
\end{aligned}
\tag{5.9}
$$

where $\boldsymbol{P}_\parallel \equiv n_e m_e \langle v_{e,\parallel}^2 \boldsymbol{v}_e \rangle_{\boldsymbol{v}}$, $\boldsymbol{P}_\perp \equiv 0.5 n_e m_e \langle v_{e,\perp}^2 \boldsymbol{v}_e \rangle_{\boldsymbol{v}}$, ρ is charge density, ρ_m is electron mass density and $\boldsymbol{u}_E$ is $\boldsymbol{E} \times \boldsymbol{B}$ drift velocity, respectively [79; 80; 81]. The terms on the right hand side of Eq.5.9 are due to curvature drift, ∇B drift, magnetization, $\boldsymbol{E} \times \boldsymbol{B}$ drift and polarization drift, respectively. The expression is simplified as $\boldsymbol{u}_\perp = \boldsymbol{u}_c + \boldsymbol{u}_g + \boldsymbol{u}_m + \boldsymbol{u}_{\boldsymbol{E}\times\boldsymbol{B}} + \boldsymbol{u}_p$, in which $u_{\boldsymbol{E}\times\boldsymbol{B}}$ does not affect the energy conversion. Since the pressure tensor is gyrotropic due to the high guide-field, Eq.5.9 gives an accurate description for $\boldsymbol{u}_\perp$.

Figures 5.11(a) and (b) show the spatial distribution of $\boldsymbol{E} \cdot \boldsymbol{u}_p$ and $\boldsymbol{E} \cdot \boldsymbol{u}_c$ respectively. The polarization drift term $\boldsymbol{E} \cdot \boldsymbol{u}_p$ has a significant effect in the downstream near the X-point, while the curvature drift term $\boldsymbol{E} \cdot \boldsymbol{u}_c$ is a globally dominant term of $\boldsymbol{E} \cdot \boldsymbol{u}_\perp$. In contrast, the contribution from ∇B drift in the high guide-field reconnection is small unlike that in the anti-parallel reconnection [81]. The contribution from the magnetization term is small compared to these two. When the flow velocity $\boldsymbol{u}$ is along the magnetic field curvature $\boldsymbol{\kappa}$ due to tension force, the curvature drift term can be estimated as $\boldsymbol{E} \cdot \boldsymbol{u}_c \sim (\boldsymbol{P}_\parallel / n_e \boldsymbol{B} \times \boldsymbol{\kappa} / B^2) \cdot (-\boldsymbol{u} \times \boldsymbol{B}) > 0$. The cumulation of curvature drift for energy conversion is significant near the X-point due to the magnetic field curvature $\boldsymbol{\kappa}$ in the downstream.

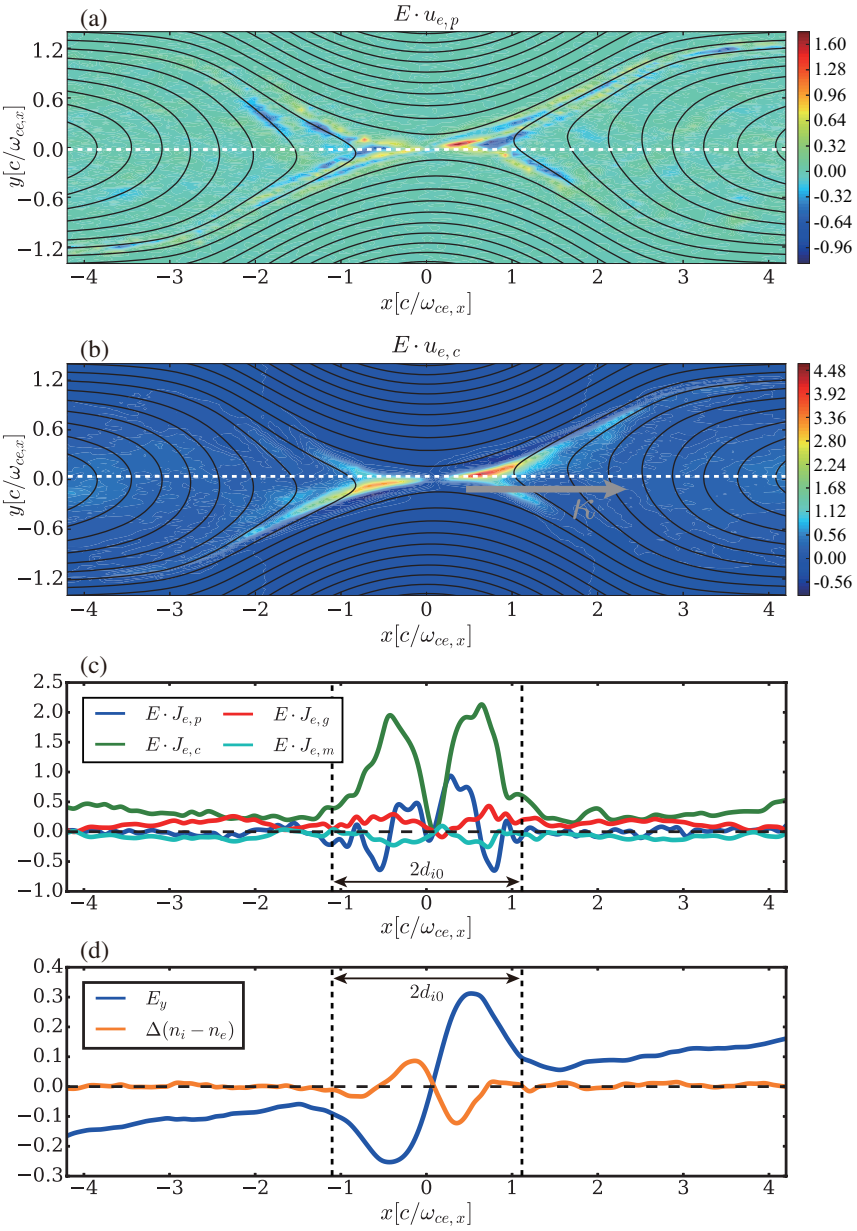

Figure 5.11: 2D profiles of the energy conversion rate due to (a) polarization drift $\boldsymbol{E}\cdot\boldsymbol{u}_p$ and (b) curvature drift $\boldsymbol{E}\cdot\boldsymbol{u}_c$ in the quasi-steady state. (c) 1D profiles of the energy conversion rate due to different types of current terms. $\boldsymbol{E}\cdot\boldsymbol{u}_c$, $\boldsymbol{E}\cdot\boldsymbol{u}_p$, $\boldsymbol{E}\cdot\boldsymbol{u}_g$ and $\boldsymbol{E}\cdot\boldsymbol{u}_m$ represent energy conversion due to curvature drift, polarization drift, ∇B drift and magnetization, respectively. (d) 1D profiles of the partially differential value of charge separation in the y-direction $\Delta(n_i - n_e) = \partial(n_i - n_e)/\partial y$ and E_y.

The overall effect of $\boldsymbol{E}\cdot\boldsymbol{u}_c$ is a strong electron energization. By contrast, the polarization term $\boldsymbol{E}\cdot\boldsymbol{u}_p$ whose intensity is comparable to the $\boldsymbol{E}\cdot\boldsymbol{u}_c$ for electron energization, is localized around the X-point. This polarization term is elaborated later.

Figure 5.11(c) shows the cumulation of $\boldsymbol{E}\cdot\boldsymbol{u}_c$, $\boldsymbol{E}\cdot\boldsymbol{u}_p$, $\boldsymbol{E}\cdot\boldsymbol{u}_g$ and $\boldsymbol{E}\cdot\boldsymbol{u}_m$ along the x-direction. In the vicinity of the X-point, the polarization term $\boldsymbol{E}\cdot\boldsymbol{u}_p$ has a significant effect on the electron magnetization. The scale of $\boldsymbol{E}\cdot\boldsymbol{u}_p$ is present within the ion inertia length d_{i0} in the vicinity of the X-point due to the charge separation as shown in Fig.5.11(d). This charge separation is caused by the parallel electric field, which is sustained by the non-ideal term of generalized Ohm's law. Due to the charge separation, E_y increases within the ion inertia length d_{i0} as shown in Fig.5.11(d). The polarization term $\boldsymbol{E}\cdot\boldsymbol{u}_p$ during the quasi-steady state under the high guide-field condition can be estimated as

$$\begin{aligned}\boldsymbol{E}\cdot\boldsymbol{u}_p &\simeq \boldsymbol{E}\cdot\left(\frac{\boldsymbol{B}}{|B|^2}\times(\boldsymbol{u}\cdot\nabla)\boldsymbol{u}_E\right)\\ &\sim E_y\frac{B_z^2}{|B|^4}u_x\frac{\partial E_y}{\partial x}.\end{aligned} \tag{5.10}$$

Therefore, E_y enhanced by the charge separation causes dissipation of magnetic energy and results in the electron perpendicular acceleration near the X-point in the high guide-field reconnection.

5.4 The Mass Ratio Effects

It has been discussed that the charge separation plays a key role on the energy conversion mechanism for electron. In general, the mass ratio effect only changes the detail structure but not overall behavior of the plasma. The charge separation, however, could be highly sensitive with the mass ratio. Since the mass ratio we used in the numerical simulation is reduced to 100 from the real nature (1836 if ion is hydrogen), it should be evaluated that the mass ratio effects on the energy conversion mechanism during magnetic reconnection with a guide-field.

We performed with different values of mass ratio varied from $m_i/m_e = 25$ to $m_i/m_e = 200$ for the magnetic reconnection with a guide-field. Figure 5.12 shows the mass ratio effect on the width of the charge separation normalized by the electron gyro-radius δ_d/r_e. The red circles denote the simulation results with different mass ratio and the blue like represents the result from Eq.5.8. The simulation results agree with the predicted mass

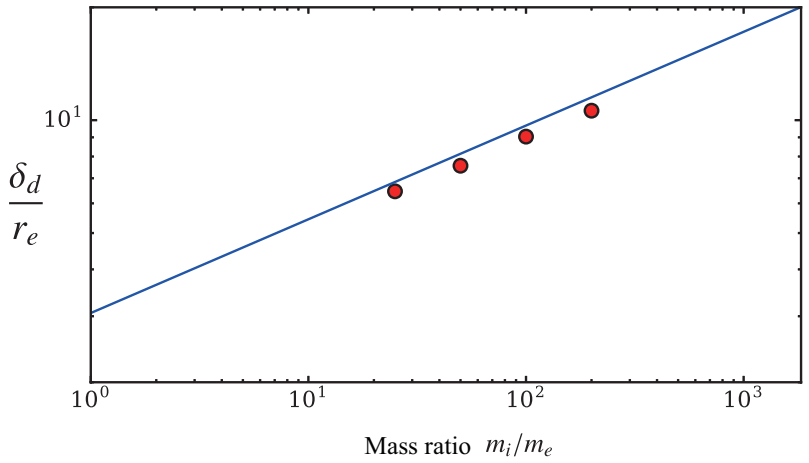

Figure 5.12: The relationship between the mass ratio m_i/m_e and the width of the charge separation normalized by the electron gyro-radius δ_d/r_e at the separatirx. The red circles denote the simulation results and the blue line represents the result from Eq.5.8.

ratio effect by Eq.5.8. This agreement is one of the evidence that we can rely on this equation to describe the width of the charge separation at the separatrix even this does not prove that the Eq.5.8 is universal. Since the dimension-less parameter ω_{pe}/ω_{ce} and the ratio between the light velocity and the initial electron thermal velocity $c/v_{e,th}$ are both reduced to 9 from the typical value at sites of reconnection 10-100 and 20-200, respectively, the simulation results represent δ_d/r_e could reach 10 in the real mass ratio 1836. Using typical values for these parameters at sites of reconnection, however, δ_d/r_e is estimated below 10 as discussed in previous section.

Chapter 6

Discussion and Conclusions

We introduced the guide-field reconnection results from UTST and MRX laboratory experiments and 2D PASMO numerical simulation in previous chapters. In both the experiments and the simulations, the electron heating was observed in the vicinity of the X-point and at the separatrix. In this chapter, we discuss a possible electron heating mechanism based on the experiment and simulation results.

6.1 Comparison between the Experiments and the Simulation

In the MRX guide-field reconnection experiment, the electron temperature measured by the Langmuir probe is highest around the X-point and elongated along with the high density separatrix. Since the electron parallel acceleration and heating occurs in the vicinity of the X-point, it can not explain the electron heating in the separatrix. On the other hand, the perpendicular heating suggested in previous chapter occurs at the high density separatrix. Therefore, the experiments and simulations suggest that electrons gain both the parallel and perpendiuclar kinetic/thermal energy by parallel electric field, which is mainly inductive field and perpendicular electric field, which is mainly electrostatic field, respectively.

Figure 6.1 shows the guide-field ratio dependance on the electron heating in the vicinity of the X-point in MRX experiments and PASMO simulations. The feature of electron heating measured in MRX agrees well with that of 2D PASMO numerical simulations qualitatively. However, the spatial width of the high temperature region is broader when the guide-field ratio decreases. The possible candidate for this problem is effects from 3D structure such as flux ropes are proven to be important under certain discharge conditions

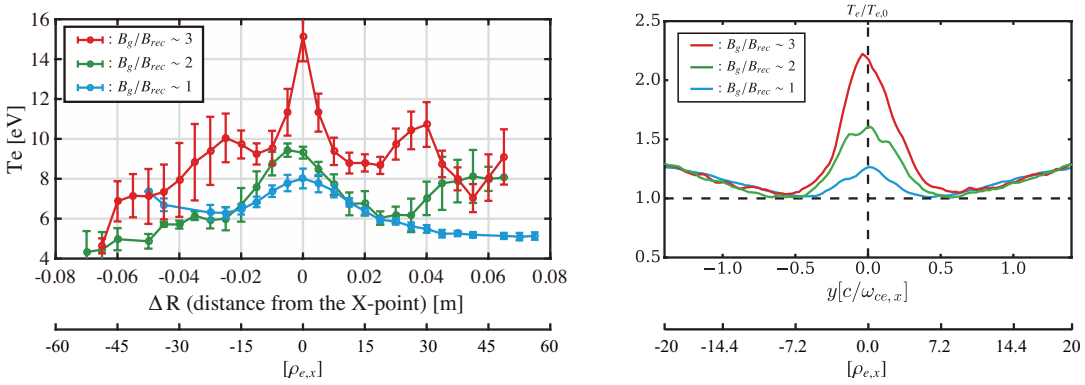

Figure 6.1: Radial profiles of T_e with three different guide-field ratio in the middle of the quasi-steady state period in MRX experiments and PASMO simulations.

[82]. When the guide-field ratio increases, the reconnection itself becomes 2D-like, thus, the difference between the experiments and the simulations becomes small.

6.2 Conclusions

Experimental and simulation studies on energy conversion for electrons during guide-field reconnection lead to the following three central conclusions:

1. Electrons are heated non-classically around the X-point. Energy from the reconnection electric field is quickly dissipated near the electron diffusion region and classical Ohmic dissipation does not account for the large observed electron heating, indicating the presence of anomalous resistivity.
2. The electron heating observed around the X-point strongly depends on the guide-field ratio, indicating the parallel acceleration for electrons is the main energy conversion mechanism for the guide-field reconnection.
3. The perpendicular electron heating and acceleration are suggested by means of 2D PIC simulation. Breaking of electron magnetic moment due to the charge separation leads the electron perpendicular heating at the high density separatrix and electrons are accelerated perpendicularly near the X-point and exhausted into the downstream.

Each of the above main conclusions is described in detail in the following subsections.

6.2.1 Electron heating at the X-point

The 2D electron temperature profile obtained using Thomson scattering measurement system and triple Langmuir probes in UTST and MRX respectively shows that electrons are heated around the X-point. Measurements and analyses suggest that electrons are heated by anomalous resistivity, but the precise mechanisms that generate the anomalous resistivity remain unknown. The classical Ohmic dissipation based on the perpendicular Spitzer resistivity cannot explain the measured 2D temperature profile. The required heating power exceeds that of classical Ohmic dissipation by a factor due to the high electron temperature. To explain the high electron temperature, the Ohmic dissipation must be larger than the classical value, indicating the presence of anomalous resistivity. Magnetic and electrostatic fluctuations in the lower hybrid frequency range are observed near the X-point. These fluctuations may contribute to the observed non-classical electron heating, but additional measurements on the wave characteristics are required to draw definitive conclusions.

6.2.2 Guide-field effects on the electron heating

The 1D electron temperature profile with three different guide-field ratio in MRX suggests that the guide-field ratio plays a key role on the electron heating near the X-point. The parallel component of $\boldsymbol{E}\cdot\boldsymbol{J}$ is dominant in all three different guide-field ratio unlike the anti-parallel reconnection [83]. Since this trend is also observed in 2D PASMO simulation qualitatively, the parallel acceleration is a strong candidate for the electron energization in the vicinity of the X-point.

6.2.3 Electron perpendicular heating and acceleration

The electron perpendicular heating mainly due to the breaking of magnetic moment conservation in the high density separatrix is observed in 2D PASMO simulation. The charge separation generates intense variation of electric field, which is sustained by the non-ideal effects within the several electron Larmor radii. Meanwhile, electron perpendicular acceleration takes place manly due to the polarization drift term as well as the curvature drift term of the magnetic energy dissipation in the downstream near the X-point. This energy

conversion mechanism can explain the elongated profile of the high electron temperature measured in MRX.

6.3 Suggested Future Works

6.3.1 Anomalous Resistivity

The observed non-classical electron heating is related to an important problem. We observed magnetic and electrostatic fluctuations in the lower hybrid frequency range in the MRX experiment. These fluctuations may originate from different types of waves propagating along the magnetic fields, which possibly contribute to the development of anomalous resistivity near the X-point. A full particle simulations for the wave activity in 2D or 3D with verifying the guide-field ratio are required to address this problem.

6.3.2 Collisional Effect

Since the parallel acceleration is a key energy conversion mechanism, the collisional effects, which changes the Dreicer runaway field, can be studied in detail via numerical simulation with installing the collisional effect. In the anti-parallel reconnection, the effects from Coulomb collisions are reported to contribute to broadening the width but the layer width remains narrow in simulations [84]. However, the role of the collision is still open question in the guide-field reconnection.

6.3.3 Energetic Particles

Runaway electrons are expected to exist near the X-point when the reconnection electric field exceeds the Dreicer runaway field, in both MRX and UTST [40]. Using Soft X-Ray measurement, the existence of the energetic particles is reported, however, the detail mechanism is still unsolved due to the limited spatial resolution of the measurement system. It is valuable to measure if and where the fast electrons are generated. There are ongoing debates on energetic particle generation between models based on the single X-line geometry and those emphasizing the multiple X-line geometry. Measuring the population of energetic electrons under different magnetic geometries will be beneficial for understanding energetic particle generation.

References

[1] R. G. Giovanelli. A Theory of Chromospheric Flares. *Nature*, 158:81, July 1946. URL http://dx.doi.org/10.1038/158081a0.

[2] Eric Ronald Priest and Terry Forbes. *Magnetic reconnection. MHD theory and applications*. Cambridge University Press, United Kingdom, 2000. ISBN 0-521-48179-1.

[3] Ellen G. Zweibel and Masaaki Yamada. Magnetic reconnection in astrophysical and laboratory plasmas. *Annual Review of Astronomy and Astrophysics*, 47(1):291–332, 2009. doi: 10.1146/annurev-astro-082708-101726. URL https://doi.org/10.1146/annurev-astro-082708-101726.

[4] Masaaki Yamada, Russell Kulsrud, and Hantao Ji. Magnetic reconnection. *Rev. Mod. Phys.*, 82:603–664, Mar 2010. doi: 10.1103/RevModPhys.82.603. URL http://link.aps.org/doi/10.1103/RevModPhys.82.603.

[5] J. B. Taylor. Relaxation and magnetic reconnection in plasmas. *Rev. Mod. Phys.*, 58:741–763, Jul 1986. doi: 10.1103/RevModPhys.58.741. URL http://link.aps.org/doi/10.1103/RevModPhys.58.741.

[6] M. Yamada, F. M. Levinton, N. Pomphrey, R. Budny, J. Manickam, and Y. Nagayama. Investigation of magnetic reconnection during a sawtooth crash in a high - temperature tokamak plasma. *Physics of Plasmas*, 1(10):3269–3276, 1994. doi: http://dx.doi.org/10.1063/1.870479. URL http://scitation.aip.org/content/aip/journal/pop/1/10/10.1063/1.870479.

[7] P. Sweet. *Electromagnetic Phenomena in Cosmical Physics*. Cambridge University Press, 1958.

[8] E. N. Parker. Sweet's mechanism for merging magnetic fields in conducting fluids. *Journal of Geophysical Research*, 62(4):509–520, 1957. ISSN 2156-2202. doi: 10.1029/JZ062i004p00509. URL http://dx.doi.org/10.1029/JZ062i004p00509.

[9] L. Spitzer. *Physics of fully ionized gases, 2nd ed.* Interscience Publishers, New York, USA, 1962.

[10] Petschek H. E. Aas-nana symposium on the physics of solar flares. *NASA Spec. Publ.*, SP-50:425, 1964.

[11] D. Biskamp. Magnetic reconnection via current sheets. *The Physics of Fluids*, 29 (5):1520–1531, 1986. doi: 10.1063/1.865670. URL http://aip.scitation.org/doi/abs/10.1063/1.865670.

[12] D. A. Uzdensky and R. M. Kulsrud. Two-dimensional numerical simulation of the resistive reconnection layer. *Physics of Plasmas*, 7(10):4018–4030, 2000. doi: 10.1063/1.1308081. URL http://aip.scitation.org/doi/abs/10.1063/1.1308081.

[13] B. U. Ö. Sonnerup. *Magnetic field reconnection in Solar system plasma physics*, volume 3. edited by L. T. Lanzerotti, C. F. Kennel, and E. N. Parker (Louis JNorth-Holland Pub. Co.), 1979.

[14] X. H. Deng and H. Matsumoto. Rapid magnetic reconnection in the Earth' s magnetosphere mediated by whistler waves. *Nature*, 410:557, March 2001. URL http://dx.doi.org/10.1038/35069018.

[15] M. Øieroset, T. D. Phan, M. Fujimoto, R. P. Lin, and R. P. Lepping. In situ detection of collisionless reconnection in the Earth's magnetotail. *Nature*, 412:414, July 2001. URL http://dx.doi.org/10.1038/35086520.

[16] F. S. Mozer, S. D. Bale, and T. D. Phan. Evidence of diffusion regions at a subsolar magnetopause crossing. *Phys. Rev. Lett.*, 89:015002, Jun 2002. doi: 10.1103/PhysRevLett.89.015002. URL https://link.aps.org/doi/10.1103/PhysRevLett.89.015002.

[17] Yang Ren, Masaaki Yamada, Stefan Gerhardt, Hantao Ji, Russell Kulsrud, and Aleksey Kuritsyn. Experimental verification of the hall effect during magnetic reconnection in a laboratory plasma. *Phys. Rev. Lett.*, 95:055003, Jul 2005. doi: 10.1103/PhysRevLett.95.055003. URL https://link.aps.org/doi/10.1103/PhysRevLett.95.055003.

[18] M. R. Brown, C. D. Cothran, and J. Fung. Two fluid effects on three-dimensional reconnection in the swarthmore spheromak experiment with comparisons to space data. *Physics of Plasmas*, 13(5):056503, 2006. doi: 10.1063/1.2180729. URL https://doi.org/10.1063/1.2180729.

[19] Ritoku Horiuchi and Tetsuya Sato. The meandering orbit effect on stabilization of the tilting instability in a field reversed configuration. *Physics of Fluids B: Plasma Physics*, 2(11):2652–2660, 1990. doi: 10.1063/1.859579. URL https://doi.org/10.1063/1.859579.

[20] E. G. Harris. On a plasma sheath separating regions of oppositely directed magnetic field. *Il Nuovo Cimento (1955-1965)*, 23(1):115–121, Jan 1962. ISSN 1827-6121. doi: 10.1007/BF02733547. URL https://doi.org/10.1007/BF02733547.

[21] Michael Hesse, Karl Schindler, Joachim Birn, and Masha Kuznetsova. The diffusion region in collisionless magnetic reconnection. *Physics of Plasmas*, 6(5):1781–1795, 1999. doi: 10.1063/1.873436. URL https://doi.org/10.1063/1.873436.

[22] P. L. Pritchett. Collisionless magnetic reconnection in a three-dimensional open system. *Journal of Geophysical Research: Space Physics*, 106(A11):25961–25977, 2001. ISSN 2156-2202. doi: 10.1029/2001JA000016. URL http://dx.doi.org/10.1029/2001JA000016.

[23] D Biskamp. Instability of two-dimensional collisionless plasmas with neutral points. *Plasma Physics*, 13(11):1013, 1971. URL http://stacks.iop.org/0032-1028/13/i=11/a=003.

[24] Ritoku Horiuchi and Tetsuya Sato. Particle simulation study of driven magnetic reconnection in a collisionless plasma. *Physics of Plasmas*, 1(11):3587–3597, 1994. doi: http://dx.doi.org/10.1063/1.870894. URL http://scitation.aip.org/content/aip/journal/pop/1/11/10.1063/1.870894.

[25] A. Ishizawa and R. Horiuchi. Suppression of hall-term effects by gyroviscous cancellation in steady collisionless magnetic reconnection. *Phys. Rev. Lett.*, 95:045003, Jul 2005. doi: 10.1103/PhysRevLett.95.045003. URL https://link.aps.org/doi/10.1103/PhysRevLett.95.045003.

[26] A. A. Galeev and R. N. Sudan. *Handbook of plasma physics. Vol. 2: Basic plasma physics II.* North-Holland Publishing Company, Amsterdam - New York - Oxford., 1985.

[27] William Daughton and H. Karimabadi. Kinetic theory of collisionless tearing at the magnetopause. *Journal of Geophysical Research: Space Physics*, 110(A3):n/a–n/a, 2005. ISSN 2156-2202. doi: 10.1029/2004JA010751. URL http://dx.doi.org/10.1029/2004JA010751. A03217.

[28] A. A. Petrukovich. Origins of plasma sheet by. *Journal of Geophysical Research: Space Physics*, 116(A7):n/a–n/a, 2011. ISSN 2156-2202. doi: 10.1029/2010JA016386. URL http://dx.doi.org/10.1029/2010JA016386. A07217.

[29] M. Yamada, Y. Ono, A. Hayakawa, M. Katsurai, and F. W. Perkins. Magnetic reconnection of plasma toroids with cohelicity and counterhelicity. *Phys. Rev. Lett.*, 65:721–724, Aug 1990. doi: 10.1103/PhysRevLett.65.721. URL https://link.aps.org/doi/10.1103/PhysRevLett.65.721.

[30] Y. Ono, A. Morita, M. Katsurai, and M. Yamada. Experimental investigation of three - dimensional magnetic reconnection by use of two colliding spheromaks. *Physics of Fluids B: Plasma Physics*, 5(10):3691–3701, 1993. doi: 10.1063/1.860840. URL https://doi.org/10.1063/1.860840.

[31] Ritoku Horiuchi and Tetsuya Sato. Particle simulation study of collisionless driven reconnection in a sheared magnetic field. *Physics of Plasmas*, 4(2):277–289, 1997. doi: 10.1063/1.872088. URL https://doi.org/10.1063/1.872088.

[32] J. D. Huba. Hall magnetic reconnection: Guide field dependence. *Physics of Plasmas*, 12(1):012322, 2005. doi: 10.1063/1.1834592. URL https://doi.org/10.1063/1.1834592.

[33] T. D. Tharp, M. Yamada, H. Ji, E. Lawrence, S. Dorfman, C. E. Myers, and J. Yoo. Quantitative study of guide-field effects on hall reconnection in a laboratory plasma. *Phys. Rev. Lett.*, 109:165002, Oct 2012. doi: 10.1103/PhysRevLett.109.165002. URL https://link.aps.org/doi/10.1103/PhysRevLett.109.165002.

[34] T. D. Tharp, M. Yamada, H. Ji, E. Lawrence, S. Dorfman, C. Myers, J. Yoo, Y.-M. Huang, and A. Bhattacharjee. Study of the effects of guide field on hall reconnection. *Physics of Plasmas*, 20(5):055705, 2013. doi: 10.1063/1.4805244. URL https://doi.org/10.1063/1.4805244.

[35] Ritoku Horiuchi, Shunsuke Usami, and Hiroaki Ohtani. Influence of a guide field on collisionless driven reconnection. *Plasma and Fusion Research*, 9:1401092–1401092, 2014. ISSN 1880-6821. doi: 10.1585/pfr.9.1401092. URL http://ci.nii.ac.jp/naid/130005089495/en/.

[36] S. Inoue, Y. Ono, H. Tanabe, R. Horiuchi, and C.Z. Cheng. Numerical study of energy conversion mechanism of magnetic reconnection in the presence of high guide field. *Nuclear Fusion*, 55(8):083014, 2015. URL http://stacks.iop.org/

0029-5515/55/i=8/a=083014.

[37] Stephen M. White. Energetic electron populations in solar flares. *AIP Conference Proceedings*, 294(1):199–204, 1994. doi: 10.1063/1.45191. URL http://aip.scitation.org/doi/abs/10.1063/1.45191.

[38] Hamish A. S. Reid and Eduard P. Kontar. Evolution of the solar flare energetic electrons in the inhomogeneous inner heliosphere. *Solar Physics*, 285(1):217–232, Jul 2013. ISSN 1573-093X. doi: 10.1007/s11207-012-0013-x. URL https://doi.org/10.1007/s11207-012-0013-x.

[39] Gottfried Mann. Energetic electrons generated during solar flares. *Journal of Plasma Physics*, 81(6), 2015. doi: 10.1017/S0022377815001166.

[40] Tomohiko USHIKI, Michiaki INOMOTO, Kotaro YAMASAKI, Xuehan GUO, Takumichi SUGAWARA, Keita MATSUYAMA, Haruhisa KOGUCHI, and Takuma YAMADA. Generation of energetic electrons during spherical tokamak merging in utst. *Plasma and Fusion Research*, 11:2402100–2402100, 2016. doi: 10.1585/pfr.11.2402100.

[41] Ami M. DuBois, Abdulgader F. Almagri, Jay K. Anderson, Daniel J. Den Hartog, John David Lee, and John S. Sarff. Anisotropic electron tail generation during tearing mode magnetic reconnection. *Phys. Rev. Lett.*, 118:075001, Feb 2017. doi: 10.1103/PhysRevLett.118.075001. URL https://link.aps.org/doi/10.1103/PhysRevLett.118.075001.

[42] P. L. Pritchett and F. V. Coroniti. Three-dimensional collisionless magnetic reconnection in the presence of a guide field. *Journal of Geophysical Research: Space Physics*, 109(A1):n/a–n/a, 2004. ISSN 2156-2202. doi: 10.1029/2003JA009999. URL http://dx.doi.org/10.1029/2003JA009999. A01220.

[43] Paolo Ricci, J. U. Brackbill, W. Daughton, and Giovanni Lapenta. Collisionless magnetic reconnection in the presence of a guide field. *Physics of Plasmas*, 11(8):4102–4114, 2004. doi: http://dx.doi.org/10.1063/1.1768552. URL http://scitation.aip.org/content/aip/journal/pop/11/8/10.1063/1.1768552.

[44] G. Lapenta, S. Markidis, A. Divin, M. Goldman, and D. Newman. Scales of guide field reconnection at the hydrogen mass ratio. *Physics of Plasmas*, 17(8):082106, 2010. doi: http://dx.doi.org/10.1063/1.3467503. URL http://scitation.aip.org/content/aip/journal/pop/17/8/10.1063/1.3467503.

[45] K. Shibata, S. Masuda, M. Shimojo, H. Hara, T. Yokoyama, S. Tsuneta, T. Kosugi, and Y. Ogawara. Hot-plasma ejections associated with compact-loop solar flares. *The Astrophysical Journal Letters*, 451(2):L83, 1995. URL http://stacks.iop.org/1538-4357/451/i=2/a=L83.

[46] Kazunari Shibata and Syuniti Tanuma. Plasmoid-induced-reconnection and fractal reconnection. *Earth, Planets and Space*, 53(6):473–482, Jun 2001. ISSN 1880-5981. doi: 10.1186/BF03353258. URL https://doi.org/10.1186/BF03353258.

[47] S. Tsuneta. Structure and Dynamics of Magnetic Reconnection in a Solar Flare. *The Astrophysical Journal*, 456:840, January 1996. doi: 10.1086/176701.

[48] Hirohisa Hara, Tetsuya Watanabe, Louise K. Harra, J. Leonard Culhane, and Peter R. Young. Plasma motions and heating by magnetic reconnection in a 2007 may 19

flare. *The Astrophysical Journal*, 741(2):107, 2011. URL http://stacks.iop.org/0004-637X/741/i=2/a=107.

[49] W. J. Hughes. *Introduction to Space Physics edited by M. G. Kivelson and C. T. Russell*. Cambridge University Press, New York, April 1995.

[50] G. Paschmann, B. U. Ö. Sonnerup, I. Papamastorakis, N. Sckopke, G. Haerendel, S. J. Bame, J. R. Asbridge, J. T. Gosling, C. T. Russell, and R. C. Elphic. Plasma acceleration at the Earth's magnetopause: evidence for reconnection. *Nature*, 282: 243, November 1979. URL http://dx.doi.org/10.1038/282243a0.

[51] B. U. Ö. Sonnerup, G. Paschmann, I. Papamastorakis, N. Sckopke, G. Haerendel, S. J. Bame, J. R. Asbridge, J. T. Gosling, and C. T. Russell. Evidence for magnetic field reconnection at the earth's magnetopause. *Journal of Geophysical Research: Space Physics*, 86(A12):10049–10067, 1981. ISSN 2156-2202. doi: 10.1029/JA086iA12p10049. URL http://dx.doi.org/10.1029/JA086iA12p10049.

[52] T. D. Phan, L. M. Kistler, B. Klecker, G. Haerendel, G. Paschmann, B. U. Ö. Sonnerup, W. Baumjohann, M. B. Bavassano-Cattaneo, C. W. Carlson, A. M. DiLellis, K.-H. Fornacon, L. A. Frank, M. Fujimoto, E. Georgescu, S. Kokubun, E. Moebius, T. Mukai, M. Øieroset, W. R. Paterson, and H. Reme. Extended magnetic reconnection at the Earth's magnetopause from detection of bi-directional jets. *Nature*, 404: 848, April 2000. URL http://dx.doi.org/10.1038/35009050.

[53] A. Vaivads, Y. Khotyaintsev, M. André, A. Retinò, S. C. Buchert, B. N. Rogers, P. Décréau, G. Paschmann, and T. D. Phan. Structure of the magnetic reconnection diffusion region from four-spacecraft observations. *Phys. Rev. Lett.*, 93:105001, Aug 2004. doi: 10.1103/PhysRevLett.93.105001. URL https://link.aps.org/doi/10.1103/PhysRevLett.93.105001.

[54] T. D. Phan, J. T. Gosling, M. S. Davis, R. M. Skoug, M. Oieroset, R. P. Lin, R. P. Lepping, D. J. McComas, C. W. Smith, H. Reme, and A. Balogh. A magnetic reconnection x-line extending more than 390 earth radii in the solar wind. *Nature*, 439 (7073):175–178, 01 2006. URL http://dx.doi.org/10.1038/nature04393.

[55] Vassilis Angelopoulos, James P. McFadden, Davin Larson, Charles W. Carlson, Stephen B. Mende, Harald Frey, Tai Phan, David G. Sibeck, Karl-Heinz Glassmeier, Uli Auster, Eric Donovan, Ian R. Mann, I. Jonathan Rae, Christopher T. Russell, Andrei Runov, Xu-Zhi Zhou, and Larry Kepko. Tail reconnection triggering substorm onset. *Science*, 321(5891):931–935, 2008. ISSN 0036-8075. doi: 10.1126/science.1160495. URL http://science.sciencemag.org/content/321/5891/931.

[56] Takuma Yamada, Ryota Imazawa, Shuji Kamio, Ryuma Hihara, Keita Abe, Morio Sakumura, Qinghong Cao, Takuya Oosako, Hiroaki Kobayashi, Takuma Wakatsuki, Byungil An, Yoshihiko Nagashima, Hajime Sakakita, Haruhisa Koguchi, Satoru Kiyama, Yoichi Hirano, Michiaki Inomoto, Akira Ejiri, Yuichi Takase, and Yasushi Ono. Merging startup experiments on the utst spherical tokamak. *Plasma and Fusion Research*, 5:S2100–S2100, 2010. doi: 10.1585/pfr.5.S2100.

[57] M. Inomoto, T.G. Watanabe, K. Gi, K. Yamasaki, S. Kamio, R. Imazawa, T. Yamada, X. Guo, T. Ushiki, H. Ishikawa, H. Nakamata, N. Kawakami, T. Sugawara, K. Matsuyama, K. Noma, A. Kuwahata, and H. Tanabe. Centre-solenoid-free merging

start-up of spherical tokamak plasmas in utst. *Nuclear Fusion*, 55(3):033013, 2015. URL http://stacks.iop.org/0029-5515/55/i=3/a=033013.

[58] A Sykes, R Akers, L Appel, P G Carolan, N J Conway, M Cox, A R Field, D A Gates, S Gee, M Gryaznevich, T C Hender, I Jenkins, R Martin, K Morel, A W Morris, M P S Nightingale, C Ribeiro, D C Robinson, M Tournianski, M Valovic, M J Walsh, and C Warrick. High-β performance of the start spherical tokamak. *Plasma Physics and Controlled Fusion*, 39(12B):B247, 1997. URL http://stacks.iop.org/0741-3335/39/i=12B/a=019.

[59] Y. Ono and M. Inomoto. Ultra-high-beta spherical tokamak formation by use of an oblate field-reversed configuration. *Physics of Plasmas*, 7(5):1863–1869, 2000. doi: 10.1063/1.874009. URL https://doi.org/10.1063/1.874009.

[60] T. C. Hender, S. J. Allfrey, R. Akers, L. C. Appel, M. K. Bevir, R. J. Buttery, M. Gryaznevich, I. Jenkins, O. J. Kwon, K. G. McClements, R. Martin, S. Medvedev, M. P. S. Nightingale, C. Ribeiro, C. M. Roach, D. C. Robinson, S. E. Sharapov, A. Sykes, L. Villard, and M. J. Walsh. Magneto-hydro-dynamic limits in spherical tokamaks. *Physics of Plasmas (1994-present)*, 6(5):1958–1968, 1999. doi: http://dx.doi.org/10.1063/1.873493. URL http://scitation.aip.org/content/aip/journal/pop/6/5/10.1063/1.873493.

[61] Y. Ono, T. Kimura, E. Kawamori, Y. Murata, S. Miyazaki, Y. Ueda, M. Inomoto, A.L. Balandin, and M. Katsurai. High-beta characteristics of first and second-stable spherical tokamaks in reconnection heating experiments of ts-3. *Nuclear Fusion*, 43 (8):789, 2003. URL http://stacks.iop.org/0029-5515/43/i=8/a=321.

[62] M. Yamada, H. P. Furth, W. Hsu, A. Janos, S. Jardin, M. Okabayashi, J. Sinnis, T. H. Stix, and K. Yamazaki. Quasistatic formation of the spheromak plasma configuration. *Phys. Rev. Lett.*, 46:188–191, Jan 1981. doi: 10.1103/PhysRevLett.46.188. URL https://link.aps.org/doi/10.1103/PhysRevLett.46.188.

[63] Xuehan Guo, Michiaki Inomoto, Takumichi Sugawara, Takenori G Watanabe, Kotaro Yamasaki, Tomohiko Ushiki, and Yasushi Ono. Two-dimensional electron temperature and density measurement during strong guide-field reconnection by using slide-type thomson scattering system. *Plasma and Fusion Research*, 10(3402017), 2015. doi: 10.1585/pfr.10.3402017. URL http://www.jspf.or.jp/PFR/PFR_articles/pfr2015S2/pfr2015_10-3402017.html.

[64] Xuehan Guo, Michiaki Inomoto, and Yasushi Ono. Quantitative analysis of electron heating during spherical tokamak merging by slide-type 2-d thomson scattering measurement system. *IEEJ Transactions on Fundamentals and Materials*, 134(9): 515–516, 2014. doi: 10.1541/ieejfms.134.515.

[65] Y. Ono, H. Tanabe, Y. Hayashi, T. Ii, Y. Narushima, T. Yamada, M. Inomoto, and C. Z. Cheng. Ion and electron heating characteristics of magnetic reconnection in a two flux loop merging experiment. *Phys. Rev. Lett.*, 107:185001, Oct 2011. doi: 10.1103/PhysRevLett.107.185001. URL https://link.aps.org/doi/10.1103/PhysRevLett.107.185001.

[66] M. Øieroset, R. P. Lin, T. D. Phan, D. E. Larson, and S. D. Bale. Evidence for electron acceleration up to $\sim$ 300 keV in the magnetic reconnection diffu-

sion region of earth's magnetotail. *Phys. Rev. Lett.*, 89:195001, Oct 2002. doi: 10.1103/PhysRevLett.89.195001. URL http://link.aps.org/doi/10.1103/PhysRevLett.89.195001.

[67] Tomohiko Ushiki, Michiaki Inomoto, and Haruhisa Koguchi. Soft x-ray emission observation during magnetic reconnection in spherical tokamak merging. *IEEJ Transactions on Fundamentals and Materials*, 134(9):493–496, 2014. doi: 10.1541/ieejfms.134.493.

[68] Yoo Jongsoo. *Experimental Studies of Particle Acceleration and Heating during Magnetic Reconnection*. PhD thesis, Princeton University, 2013. URL http://agile.rm.iasf.cnr.it/doc/PAAL6/Dissertation_Yoo_Princeton_June2013.pdf.

[69] I. H. Hutchinson. *Principles of Plasma Diagnostics*. Cambridge University Press, 2 edition, 2002. doi: 10.1017/CBO9780511613630.

[70] I H Hutchinson. Ion collection by a sphere in a flowing plasma: I. quasineutral. *Plasma Physics and Controlled Fusion*, 44(9):1953, 2002. URL http://stacks.iop.org/0741-3335/44/i=9/a=313.

[71] J Egedal, A Fasoli, and J Nazemi. Dynamical plasma response during driven magnetic reconnection. *Phys. Rev. Lett.*, 90:135003, Apr 2003. doi: 10.1103/PhysRevLett.90.135003. URL https://link.aps.org/doi/10.1103/PhysRevLett.90.135003.

[72] K. Yamasaki, S. Inoue, S. Kamio, T. G. Watanabe, T. Ushiki, X. Guo, T. Sugawara, K. Matsuyama, N. Kawakami, T. Yamada, M. Inomoto, and Y. Ono. Laboratory study of diffusion region with electron energization during high guide field reconnection. *Physics of Plasmas*, 22(10):101202, 2015. doi: 10.1063/1.4932345. URL https://doi.org/10.1063/1.4932345.

[73] Charles K Birdsall and A Bruce Langdon. *Plasma physics via computer simulation*. CRC press, 2004.

[74] Hiroaki Ohtani and Ritoku Horiuchi. Open boundary condition for particle simulation in magnetic reconnection research. *Plasma and Fusion Research*, 4:024–1 – 024–14, jan 2009. doi: 10.1585/pfr.4.024. URL https://ci.nii.ac.jp/naid/120005964076/en/.

[75] Can Huang, Quanming Lu, and Shui Wang. The mechanisms of electron acceleration in antiparallel and guide field magnetic reconnection. *Physics of Plasmas*, 17 (7):072306, 2010. doi: 10.1063/1.3457930. URL https://doi.org/10.1063/1.3457930.

[76] J. Egedal, W. Daughton, and A. Le. Large-scale electron acceleration by parallel electric fields during magnetic reconnection. *Nat Phys*, 8(4):321–324, 04 2012. URL http://dx.doi.org/10.1038/nphys2249.

[77] J. R. Wygant, C. A. Cattell, R. Lysak, Y. Song, J. Dombeck, J. McFadden, F. S. Mozer, C. W. Carlson, G. Parks, E. A. Lucek, A. Balogh, M. Andre, H. Reme, M. Hesse, and C. Mouikis. Cluster observations of an intense normal component of the electric field at a thin reconnecting current sheet in the tail and its role in the shock-like acceleration of the ion fluid into the separatrix region. *Journal of*

Geophysical Research: Space Physics, 110(A9), 2005. ISSN 2156-2202. doi: 10.1029/2004JA010708. URL http://dx.doi.org/10.1029/2004JA010708.

[78] J. D. Scudder, R. D. Holdaway, W. S. Daughton, H. Karimabadi, V. Roytershteyn, C. T. Russell, and J. Y. Lopez. First resolved observations of the demagnetized electron-diffusion region of an astrophysical magnetic-reconnection site. *Phys. Rev. Lett.*, 108:225005, Jun 2012. doi: 10.1103/PhysRevLett.108.225005. URL http://link.aps.org/doi/10.1103/PhysRevLett.108.225005.

[79] E. N. Parker. Newtonian Development of the Dynamical Properties of Ionized Gases of Low Density. *Physical Review*, 107(4):924–933, August 1957. doi: 10.1103/PhysRev.107.924. URL http://link.aps.org/doi/10.1103/PhysRev.107.924.

[80] Roger Blandford, Paul Simeon, and Yajie Yuan. Cosmic ray origins: An introduction. *Nuclear Physics B - Proceedings Supplements*, 256-257:9–22, 2014. ISSN 0920-5632. doi: 10.1016/j.nuclphysbps.2014.10.002. URL http://www.sciencedirect.com/science/article/pii/S0920563214001960. Cosmic Ray Origin - Beyond the Standard Models.

[81] Xiaocan Li, Fan Guo, Hui Li, and Gang Li. Nonthermally dominated electron acceleration during magnetic reconnection in a low-β plasma. *The Astrophysical Journal Letters*, 811(2):L24, 2015. URL http://stacks.iop.org/2041-8205/811/i=2/a=L24.

[82] S. Dorfman, H. Ji, M. Yamada, J. Yoo, E. Lawrence, C. Myers, and T. D. Tharp. Three-dimensional, impulsive magnetic reconnection in a laboratory plasma. *Geophysical Research Letters*, 40(2):233–238, 2013. ISSN 1944-8007. doi: 10.1029/2012GL054574. URL http://dx.doi.org/10.1029/2012GL054574.

[83] Jongsoo Yoo, Masaaki Yamada, Hantao Ji, Jonathan Jara-Almonte, and Clayton E. Myers. Bulk ion acceleration and particle heating during magnetic reconnection in a laboratory plasma. *Physics of Plasmas*, 21(5):055706, 2014. doi: 10.1063/1.4874331. URL https://doi.org/10.1063/1.4874331.

[84] V. Roytershteyn, W. Daughton, S. Dorfman, Y. Ren, H. Ji, M. Yamada, H. Karimabadi, L. Yin, B. J. Albright, and K. J. Bowers. Driven magnetic reconnection near the dreicer limit. *Physics of Plasmas*, 17(5):055706, 2010. doi: 10.1063/1.3399787. URL https://doi.org/10.1063/1.3399787.

List of Publications

査読付論文

1. X. Guo, R. Horiuchi, C. Z. Cheng, Y. Kaminou and Y. Ono "Energy conversion mechanism for electron perpendicular energy in high guide-field reconnection" Phys. Plasmas 24, 032901 (2017)

2. Xuehan Guo, Michiaki Inomoto, Takumichi Sugawara, Kotaro Yamasaki, Tomohiko Ushiki, Yasushi Ono and TS Group, "Localized electron heating by strong guide-field magnetic reconnection" Phys. Plasmas 22 101201 (2015)

3. X. Guo, M. Inomoto, T. Sugawara, T. G. Watanabe, K. Yamasaki, T. Ushiki, and Y. Ono, "Two-dimensional electron temperature and density measurement during strong guide-field reconnection by using slide-type Thomson scattering system" Plasma Fusion Res. 10, 3402017 (2015)

4. 郭 学瀚, 井 通暁, 小野 靖, "スライド型 2 次元トムソン散乱計測を用いた球状トカマク合体時の電子加熱の定量的評価" 電気学会論文誌 A, Vol.134, No.9 (2014)

5. Kyohei KONDO, Michiaki INOMOTO, Xuehan GUO, Tomohiko USHIKI, Takumichi SUGAWARA, Takum i MIHARA, Shuji KAMIO, Hiroshi TANABE and Yasushi ONO, "Separated Double-Current Layers in a High-Guide-Field Reconnection Experiment" Plasma Fusion Res. 12, 1202033 (2017)

6. Yasuhiro Kaminou, Xuehan Guo, Michiaki Inomoto, Yasushi Ono and Ritoku Horiuchi, "Numerical study of Hall effects on counter-helicity spheromak merging by two-dimensional Hall-MHD simulations" Phys. Plasma 24 032508 (2017)

7. Tomohiko USHIKI, Michiaki INOMOTO, Kotaro YAMASAKI, Xuehan GUO, Takumichi SUGAWARA, Keita MATSUYAMA, Haruhisa KOGUCHI and Takuma YAMADA, "Generation of Energetic Electrons during Spherical Tokamak Merging in UTST" Plasma Fusion Res. 11, 2402100 (2016)

8. 菅原 拓路, 郭 学瀚, 井 通暁, "中性粒子ビーム入射に向けた合体生成球状トカマクプラズマの電子密度・温度の評価", 電気学会論文誌 A, Vol.135, No.11, pp.727-728 (2016)

9. K. Yamasaki, S. Inoue, S. Kamio, T. G. Watanabe, T. Ushiki, X. Guo, T. Sugawara, K. Matsuyama, N. Kawakami, T. Yamada, M. Inomoto and Y. Ono, "Laboratory study of diffusion region with electron energization during high guide field recon-

nection" Phys. Plasmas 22 101202 (2015)

10. M. Inomoto, T.G. Watanabe, K. Gi, K. Yamasaki, S. Kamio, R. Imazawa, T. Yamada, X. Guo, T. Ushiki, H. Ishikawa, H. Nakamata, N. Kawakami, T. Sugawara, K. Matsuyama, K. Noma, A. Kuwahata and H. Tanabe, "Center-solenoid-free merging start-up pf spherical tokamak plasmas in UTST" Nucl. Fusion 55 033013 (2015)

招待講演

1. X. Guo, R. Horiuchi, S. Usami, F. Pucci, Y. Ono, "ガイド磁場リコネクション時のエネルギー変換機構", プラズマシュミレータシンポジウム 2017, 自然科学研究機構核融合研究所, 2017 年 9 月

国際口頭発表

2. X. Guo, M. Inomoto, R. Horiuchi, Y. Ono and UTST Experiment Group, "Experimental and Numerical studies for Localized Electron Heating of High Guide Field Reconnection", MR2016 The US-Japan Workshop on Magnetic Reconnection, Napa, California, Mar. 7-11, 2016

3. Xuehan Guo, Michiaki Inomoto, Takumichi Sugawara, Kotaro Yamasaki, Tomohiko Ushiki, Yasushi Ono, "Electron Heating Mechanism of Strong Guide-Field Magnetic Reconnection, SNU-UoT joint-seminar, The University of Tokyo, June 2015

4. X. Guo, M. Inomoto, T. Sugawara, K. Yamasaki, T. Ushiki, H. Nakamata, H. Ishikawa and Y. Ono,"Slide-type 2-D Thomson scattering measurement for magnetic reconnection in UTST merging experiment" 3rd A-3 Foresight workshop on Spherical Torus 2014, Kisarazu, Dec. 2014

国際ポスター発表

5. X. Guo, R. Horiuchi, S. Usami and Y. Ono, "Effective Ion Heating in Guide-Field Magnetic Reconnection" 59th Annual Meeting of the APS Division of Plasma Physics, Milwaukee, Wisconsin, United States, Oct. 23-27, 2017

6. X. Guo, R. Horiuchi, Y. Kmainou, C. Z. Cheng and Y. Ono, "Energy Conversion Mechanism for Electron Perpendicular Energy in High Guide-Field Reconnection" MR2017 US-Japan Workshop on Magnetic Reconnection, Matsuyama, Japan, Mar. 2017

7. X. Guo, R. Horiuchi, Y. Kmainou, C. Z. Cheng and Y. Ono, "Energy Conversion Mechanism for Electron Perpendicular Energy in High Guide-Field Reconnection" 58th Annual Meeting of the APS Division of Plasma Physics, San Jose, California, United States, Oct. 31- Nov. 4, 2016

8. X. Guo, T. Sugawara, M. Inomoto, K. Yamasaki, Y. Ono, UTST team, "Localized Electron Heating by Strong Guide-Field Magnetic Reconnection" 57th Annual

Meeting of the APS Division of Plasma Physics, Savannah, Georgia, United States, November 16-20, 2015

9. Xuehan Guo, Michiaki Inomoto, Takumichi Sugawara and Yasushi Ono, “Localized Electron Heating by Strong Guide-Field Magnetic Reconnection” Magnetic Reconnection in Plasmas, Nordita, Stockholm, Sweden, Aug. 2015

10. X. Guo, M. Inomoto, T. Sugawara, K. Yamasaki, T. Ushiki, and Y. Ono, “Electron Heating Mechanism of Magnetic Reconnection” 3rd A-3 Foresight Summer School on Plasma Physics, Southwestern Institute of Physics, Chengdu China, July 2015

11. X. Guo, T. Sugawara, A. Wang, M. Inomoto, and Y. Ono, ”Evaluation of Electron Heating during Strong Guide-Field Magnetic Reconnection in UTST Merging Experiment” Plasma Conference 2014, Niigata, Nov. 2014

12. X. Guo, A. Wang, T. Sugawara, M. Inomoto and Y. Ono, ”Slide-type 2D Thomson Scattering Measurement for Electron Heating of Magnetic Reconnection in UTST Merging Experiment” 24th International Toki Conference, Ceratopia Toki, Toki-city, Gifu, Nov. 2014

13. X. Guo, T. Sugawara, M. Inomoto, Y. Ono and UTST TEAM, ”Electron Heating Characteristics of Magnetic Reconnection in UTST Merging Tokamak Experiment” 56th Annual Meeting of the APS Division of Plasma Physics, New Orleans, Louisiana, Oct. 2014

14. X. Guo, T.G. Watanabe, K. Yamasaki, A. Wang, T. Ushiki, H. Nakamata, H. Ishikawa, M. Inomoto and Y. Ono, ”Electron heating during magnetic reconnection in UTST plasma merging experiment”, A3 Foresight Summer School and Workshop on Spherical Torus (ST) 2014, Jeju, Jun. 2014

15. X. Guo, T.G. Watanabe, K. Yamasaki, A. Wang, T. Ushiki, H. Ishikawa, H. Nakamata, M. Inomoto and Y. Ono, ”Quantitative analysis of electron heating during magnetic reconnection by slide-type 2-D Thomson scattering measurement in UTST” US-JAPAN Workshop on Magnetic Reconnection 2014, Tokyo, Japan, May 2014

国内口頭発表

16. X. Guo, R. Horiuchi, C. Z. Cheng, Y. Ono, ”ガイド磁場リコネクション時の電子加熱”, 磁気リコネクション研究の最前線と今後の展望, NAOJ, Tokyo, Mar. 28-29, 2016

17. 郭 学瀚, 菅原 拓路, 山崎 広太郎, 井 通暁, 小野 靖, “高ガイド磁場リコネクションによる電子加熱と磁場構造変化の評価”, 日本物理学会 第 70 回年次大会, 早稲田大学, 2015 年 3 月

18. X. Guo, M. Inomoto, T. Sugawara, K. Yamasaki, T. Ushiki, H. Nakamata, H. Ishikawa, Y. Ono, ”Electron heating mechanism during strong guide-field magnetic reconnection”, 磁気リコネクション研究の最前線 -太陽・惑星・実験室-, 東京大学本郷

キャンパス, 2015 年 3 月

19. X. Guo, M. Inomoto, T. Sugawara, K. Yamasaki, T. Ushiki, H. Nakamata, H. Ishikawa and Y. Ono, "Evaluation of electron heating during high guide-field magnetic reconnection in UTST", 第 21 回ひので-実験室リコネクション研究会 , 情報通信研究機構, 2014 年 12 月

20. 郭 学瀚, 王 安斉, 井 通暁, 小野 靖, "プラズマ合体による電子加熱の定量的な評価", ST 研究会, 核融合科学研究所, 2014 年 8 月

21. 郭 学瀚, 井 通暁, 小野 靖,"UTST 球状トカマク実験におけるスライド型 2 次元トムソン散乱計測の開発", 平成 26 年電気学会全国大会, 愛媛, 2014 年 3 月

国内ポスター発表

22. 郭 学瀚, 渡辺 岳典, 山崎 広太郎, 王 安斉, 石川 裕貴, 牛木 知彦, 中俣 浩樹, 井 通暁, 小野 靖, "スライド型 2 次元トムソン散乱計測を用いた UTST 球状トカマク合体実験における電子加熱の定量的評価" 第 10 回 核融合エネルギー連合講演会, つくば国際会議場, 2014 年 6 月

23. X. Guo, T. Ushiki, Q. Cao, T. G. Watanabe, K. Yamasaki, A. Wang, H. Ishikawa, H. Nakamata, M. Inomoto and Y. Ono, "UTST 球状トカマク実験装置におけるトムソン散乱計測と軟 X 線計測の開発", プラズマ・核融合学会第 52 回プラズマ若手夏の学校, 三浦海岸, 2013 年 9 月

受賞

1. 学生ポスター賞 第 52 回プラズマ若手夏の学校

2. Student Poster Award A3 Foresight Summer School and Workshop on Spherical Torus (ST) 2014

その他

1. 日本学術振興会 特別研究員 DC1 面接免除採用
(採用期間: 2015 年 4 月 ∼2018 年 3 月)